

**UNIVERSITY OF CRETE
DEPARTMENT OF CHEMISTRY**



Doctoral Thesis

**FORMATION, STABILITY AND STRUCTURE OF
TRANSITION METAL OXIDE CLUSTERS**

Pavle B. Glodić

Thesis Supervisor: Theofanis N. Kitsopoulos

HERAKLION 2017

*Dedicated to the memory of
my father Bogosav and my mother Jovanka*

*Posvećeno uspomeni na
mog oca Bogosava i moju majku Jovanku*

Examination Board (alphabetically)

Theofanis Kitsopoulos

prof. at the Chemistry Department, University of Crete (supervisor)

dr. Michalis Velegrakis

principal researcher the Institute of Electronic Structure and Laser

Demetrios Anglos

prof. at the Chemistry Department, University of Crete

Spiros Anastasiadis

prof. at the Chemistry Department, University of Crete

Peter Rakitzis

prof. at the Physics Department, University of Crete

Athanassios Coutsolelos

prof. at the Chemistry Department, University of Crete

Stavros Farantos

prof. at the Chemistry Department, University of Crete

Acknowledgements:

I would first like to thank my thesis supervisor Professor Dr. Theofanis N. Kitsopoulos for giving me this great opportunity to work in his group at the Institute of Electronic Structure and Laser. Professor Kitsopoulos has been an excellent and a very inspiring supervisor and under his guidance I have spent a couple of very fruitful years during which I have learned a lot about Chemical Dynamics.

Also, I would sincerely like to thank my PhD thesis co-supervisor Dr. Michalis Velegarakis for giving me the opportunity to work in the Laboratory for Clusters and gain some experience in the field of Cluster Dynamics.

I would like next to thank to my colleague Dr. Petros Samartzis for everything he taught me in the laboratory for Chemical Dynamics, and for being a very good friend. All these years he has been very helpful, patient and ready to assist whenever I needed some help.

Many thanks to Dr. Claudia Mihesan for introducing me in the field of Cluster Dynamics, and teaching me different experimental techniques, for her support in writing my thesis and being a great coworker and friend.

I am grateful to Dr. Emmanouel Klontzas for showing me basics of computational chemistry and all his great help with the theoretical calculations and many insightful discussions.

Thanks to my colleague Dr. Andreas Kartakoullis for being a very good companion and a very valuable coworker during our PhD years.

I would also like to say big thank you to my irreplaceable laser technicians and great friends Apostolos Englezis and Yannis Labrakis for their technical support whenever I needed it.

Thanks to my family and to all my friends in Serbia, Croatia and Greece for encouraging me, believing in me, giving me comfort, and for all the great time we spent together.

CURICULUM VITAE

Born: 28. May 1978, Pakrac, Croatia

Citizenship: Croatian

Education:

- PhD student at the University of Crete, Department of Chemistry, Jun 2013 – May 2017
- Master's degree in Physical Chemistry, Faculty of Physical Chemistry, University of Belgrade, 30. September 2009
 - Master thesis: "Comparison of three different approaches for labelling of amino acids tyrosine and lysine with technetium-99m"
- Graduated in Physical Chemistry, Faculty of Physical Chemistry, University of Belgrade, 17. July 2008
 - Diploma thesis: "Comparative determination of arsenic in water by method of atomic absorption spectrometry and voltammetry"
- Secondary school: School of Chemical Technology, in Smederevska Palanka, completed in 1997

Career:

- September 2013 – February 2017:

Participating in research project on Cluster formation, stability and structure and Cluster – atom collisions (co-funded by EU (European Social Fund) and Greek National Funds (General Secretariat of Research & Technology)) at Institute of Electronic Structures and Laser, Foundation for Research and Technology – Greece, Heraklion.

- October 2010 – August 2013:

Early state researcher within "ICONIC" Marie Curie Initial Training Network (ITN-238671) under the Seventh Framework Program at Institute of Electronic Structures and Laser, Foundation for Research and Technology – Greece, Heraklion.

- December 2008 – September 2010 :

Researcher trainee at Laboratory for Radioisotopes, "Vinča" Institute of Nuclear Sciences, Belgrade.

ABSTRACT

The overall goal and motivation of the research presented in this thesis is to deepen the knowledge of the physical and chemical properties of small molecular and ionic clusters. The research discussed in this thesis has two different aspects.

In the first part we investigated the influence of solvation on the photodissociation dynamics of a diatomic molecule. First, we performed a detailed study on iodine-monochloride (ICl) in order to understand photodissociation of the ICl monomer. Following this experiment, we studied changes in photochemical behavior as a result of clustering of ICl molecules with xenon (Xe) atoms.

In the second part of thesis we investigated structure, stability and fragmentation mechanisms of transition metal oxide clusters, which is crucial in order to understand the chemical reactivity of these important catalysts. The experiments were performed on small niobium and yttrium oxide clusters. Additionally, theoretical calculations based on density functional theory (DFT) have been performed in the case of $Y_xO_y^+$ clusters in order to compare with the experimental findings.

Chapter II serves to describe the experimental apparatus in detail and the conditions under which these studies were conducted. The experiments on the rare gas clusters were conducted using well established slice imaging technique, developed in the Laboratory for Chemical Dynamics. For the transition metal oxide clusters studies we applied two collision induced dissociation (CID) methods, the conventional one employing a collision cell, and a novel method using crossed molecular beams, developed in Laboratory for Clusters.

The experiments described in Chapter III concern ICl photolysis in the ultraviolet region of the spectrum (235–265 nm), which was studied using the slice imaging technique. The $Cl^*(^2P_{1/2})/Cl(^2P_{3/2})$ and the $I^*(^2P_{1/2})/I(^2P_{3/2})$ branching ratio between the

$I(^2P_{3/2})+Cl(^2P_{3/2})/Cl(^2P_{1/2})$ and $I(^2P_{1/2})+Cl(^2P_{3/2})/Cl(^2P_{1/2})$ channels is extracted from the respective iodine and chlorine photofragment images. We find that ground state chlorine atoms ($Cl(^2P_{3/2})$) are formed nearly exclusively with excited state iodine atoms ($I(^2P_{1/2})$), while excited spin-orbit chlorine atoms ($Cl(^2P_{1/2})$) are concurrently produced only with ground state iodine atoms ($I(^2P_{3/2})$). We conclude that photolysis of ICl in this UV region is a relatively “clean” source of spin-orbit excited chlorine atoms that can be used in crossed molecular beam experiments.

In Chapter IV we present slice imaging data demonstrating the influence of clustering on the photodissociation dynamics of a diatomic molecule: iodine monochloride (ICl) was dissociated at 235 nm in He and Xe seed gasses, probing both Cl and I photofragment energy and angular distributions. We observe that the kinetic energy releases of both Cl and I fragments change from He to Xe seeding. For Cl fragments, the seeding in Xe *increases* the kinetic energy release of some Cl fragments with a narrow kinetic energy distribution, and leads to some fragments with rather broad statistical distribution falling off exponentially from near-zero energies up to about 2.5 eV. Iodine fragment distribution changes even more dramatically from He to Xe seeding: sharp features essentially disappear and a broad distribution arises reaching to about 2.5 eV. Both these observations are rationalized by a simple qualitative cluster model assuming ICl dissociation inside larger xenon clusters and “on surface” of smaller Xe species.

Chapter V presents research on oxygen-rich niobium oxide clusters, formed by mixing laser-produced Nb plasma with pure oxygen. Their stability is investigated by mass spectrometry and collision-induced dissociation (CID). The research described in this chapter is focused on the application of two CID methods – (1) the conventional one, and (2) a novel experimental configuration recently developed by our group, where the cluster ions beam is crossed with a secondary beam of noble gas atoms, and the fragments are rejected by a retarding field energy analyzer. Briefly, the relative collision cross sections of $Nb_xO_y^+$ ($x = 1, 2, y = 2-12$) clusters have been measured in order to obtain information on their stability and structure. In addition, information about their fragmentation channels has been obtained.

Finally, Chapter VI is dedicated to yttrium oxide cluster cations, which have been experimentally and theoretically studied. We produced small, oxygen-rich yttrium oxide clusters, $Y_xO_y^+$ ($x = 1, 2, y = 1-13$), by mixing the laser produced yttrium plasma with a molecular oxygen jet. Mass spectrometry measurements showed that the most stable clusters are those consisting of one yttrium and an odd number of oxygen atoms of the form YO_{2k+1}^+ ($k = 0-6$). Additionally, we performed collision induced dissociation experiments, which indicated that the loss of pairs of oxygen atoms down to a YO^+ core is the preferred fragmentation channel for all clusters investigated. Furthermore, we conduct DFT calculations and we obtained two types of low energy structures: one containing an yttrium cation core and the other composed of YO^+ core and O_2 ligands, being in agreement with the observed fragmentation pattern. Finally, from the fragmentation studies, total collision cross sections are obtained and these are compared with geometrical cross sections of the calculated structures.

Keywords: photodissociation, slice imaging, metal oxide clusters, collision induced dissociation

Table of Contents

Chapter I: Introduction.....	1
1.1 Theory	1
1.1.1 Light and matter interaction (absorption, emission, induced emission)	1
1.1.2 Spin-orbit coupling	5
1.1.3 Non-dissociative decay mechanism.....	7
1.1.3.1 Jablonski diagrams.....	7
1.1.3.2 Vibrational relaxation	9
1.1.3.3 Fluorescence	10
1.1.3.4 Internal conversion	10
1.1.3.5 Intersystem crossing.....	11
1.1.4 Dissociation mechanisms	12
1.1.4.1 Direct dissociation and the reflection principle.....	12
1.1.4.2 Predissociation.....	13
1.1.5 Clusters.....	15
1.1.5.1 Introduction.....	15
1.1.5.2 Generation of rare gas clusters by supersonic expansion	21

1.1.5.3 Generation of metal oxide clusters by laser vaporization	21
1.2 Experimental techniques	23
1.2.1 Mass spectrometry	23
1.2.1.1 Ionization and fragmentation	24
1.2.1.2 Linear time-of-flight (TOF) mass spectrometer	25
1.2.2 Resonance enhanced multi-photon ionization (REMPI).....	27
1.2.3 Velocity map imaging	29
1.2.3.1 Newton spheres.....	30
1.2.3.2 Velocity map imaging of photodissociation.....	33
1.2.3.3 The velocity mapping experiment	34
1.2.4 Slice imaging	38
1.2.5 Collision-induced dissociation	43
References	47
Chapter II: Experimental Apparatus and Methods.....	52
2.1 The slice imaging experimental apparatus	52
2.1.2 Data analysis.....	57
2.2 The cluster experimental apparatus.....	58

2.2.1 Conventional and crossed beams method	62
2.2.2 Fragmentation cross sections measurements.....	65
References	69
Chapter III: Ultraviolet photodissociation of iodine monochloride (ICl) at 235, 250 265 nm.....	71
3.1 Introduction.....	71
3.2 Experimental setup.....	73
3.3 Results	75
3.3.1 I-atom images	75
3.3.2 I*-atom images	80
3.3.3 Cl-atom images	80
3.3.4 Cl*-atom images	81
3.4 Discussion.....	81
3.5 Conclusion.....	86
References	87
Chapter IV: Driving photochemistry by clustering: The ICl case.....	90
4.1 Introduction.....	90

4.2 Experimental setup.....	92
4.3 Results	93
4.3.1 Cl and Cl* photofragments.....	93
4.3.2 I and I* photofragments	96
4.4 Discussion.....	99
4.4.1 Cl and Cl* photofragments.....	99
4.4.2 I and I* photofragments	103
4.5 Conclusion	105
References	107
Chapter V: Collision-induced dissociation of Nb_xO_y^+ ($x = 1, 2, y = 2-12$) clusters: crossed molecular beams and collision cell studies.....	109
5.1 Introduction.....	109
5.2 Experimental apparatus and methods.....	111
5.2.1 Setup.....	111
5.3 Results	112
5.3.1 Mass spectra.....	112
5.3.2 Fragmentation channels.....	114

5.3.3 Collision cross section measurements.....	117
5.3.4 Collisional multiionization	122
5.4 Conclusions.....	125
References	126
Chapter VI: Formation, fragmentation and structures of $Y_xO_y^+$ ($x = 1, 2$, $y = 1-13$) clusters: collision induced dissociation experiments and density functional theory calculations.....	131
6.1 Introduction.....	131
6.2 Experimental apparatus and methods.....	134
6.2.1 Setup.....	134
6.3 DFT calculations	135
6.4 Results and discussion.....	137
6.4.1 Mass spectra.....	137
6.4.2 Fragmentation channels.....	138
6.4.3 DFT calculations	141
6.4.4 Collision cross section measurements.....	150
6.5 Conclusions.....	154
References	156

LIST OF FIGURES

Figure

1.1.	The variation of the electric and the magnetic component of an electromagnetic wave, with wavelength λ , as it propagates along the x-axis...	2
1.2.	Absorption and emission processes in a two-state system.....	2
1.3.	Schematic representation of Hund's case (a).....	6
1.4.	Schematic representation of Hund's case (c).....	7
1.5.	Jablonski diagram illustrating the photophysical processes in an electronically excited state	8
1.6.	Steps leading to fluorescence.....	9
1.7.	Steps leading to intersystem crossing.....	11
1.8.	Schematic representation of the reflection principle.....	12
1.9.	Schematic representation of Herzberg type I (electronic) predissociation.....	13
1.10.	Schematic representation of Herzberg type II (vibrational) predissociation...	14
1.11.	Molecular model of adiabatic cooling by collisions during expansion from a reservoir with Maxwellian velocity distribution into the directed molecular flow with a narrow distribution around the flow velocity u	19

1.12.	Vapour pressure p_s of argon and local pressure p_{loc} as a function of normalised distance $z^* = z/d$ from the nozzle for different stagnation pressures p_0 in the reservoir.....	21
1.13.	Laser ablation.....	22
1.14.	TOF scheme.....	25
1.15.	(a) One- and (b) two-colour resonance enhanced multiphoton ionization (REMPI) schemes.....	28
1.16.	(a) A pair of Newton spheres with spherical coordinates r (not shown), θ , and φ , where θ is the polar angle defined with respect to the z axis (vertical axis in the figure), φ is the azimuthal angle, and r is the sphere radius. Two events are shown in (a) with equal and opposite momentum. (b) By summing up a large number of events (here for particle B), a surface pattern emerges as shown. Most of the surface intensity of this example is at the poles, representative of a typical $\cos^2\theta$ distribution.....	32
1.17.	(A): The imaging approach for measuring Newton spheres from photodissociation. (a) Photodissociation of molecules in a molecular beam using a linearly polarized laser. (b) Conversion of the photofragment molecules making up the Newton spheres into ions by laser ionization. (c) Projection of the ion spheres onto a two-dimensional (2-D) detector. (d) Mathematical transformation of the 2-D image back to the three-dimensional data of step (a). (B): Schematic representation of the electrostatic lens used for velocity map imaging of photodissociation.....	35

1.18.	Typical ion imaging setup, consisting of a homogenous extraction field E , a drift region of length L and a position-sensitive detector (phosphor screen in combination with a CCD camera).....	40
1.19.	(a) The upper panel depicts the spatial evolution of the ion cloud on its way to the detector for the case of a <i>delayed extraction</i> of the ion cloud ($\tau = 250$ ns). A space focus appears in the drift region after which the axial width of the ion cloud increases rapidly. The lower panel shows the time width of the ion cloud at the detector as a function of the photofragment velocity u_0 ($c = 1000$ m/s). The different curves correspond to different delay times τ . ΔT increases almost linearly over a wide range of photofragment velocities as well as extraction delays. The dependency of ΔT on τ shows a minimum at zero delay times (DC extraction).....	42
2.1.	Schematic view of the slice imaging apparatus.....	53
2.2.	Scaled schematic of the ion optics (drawing units in mm).....	54
2.3.	Schematic view of the molecular beam apparatus utilized to perform the CID experiments.....	59
2.4.	Schematic diagram of the experimental arrangement indicating the two different configurations used to measure fragmentation cross sections by: (a) “conventional” CID method with mass selection and reflectron detector and (b) crossed molecular beams arrangement with a retarding potential analyzer	62

2.5.	Intensity of “beam off” (solid line) and “beam on” (dashed line) signal as a function of grid voltage in the simplest case of an ion with only one fragmentation channel.....	66
3.1.	Piezo valve design for operation with corrosive gases.....	74
3.2.	(a) I-atom photofragment images at three dissociation wavelengths. At 235 nm, the experiment is performed with a single color. (b) Kinetic energy release (KER) distributions obtained by appropriate radial integration of the slice images shown in caption (a). (c) Angular distributions obtained by appropriate integrating the slice images shown in caption (a).....	76
3.3.	I*-photofragment images, KER, and angular distributions.....	77
3.4.	Cl-photofragment images, KER, and angular distributions.....	77
3.5.	Cl*-photofragment images, KER, and angular distributions.....	78
3.6.	Schematic drawing of the potential energy surfaces for the states involved in ICl absorption from Yabushita <i>et al.</i>	82
4.1.	(Top) Cl-photofragment slice images following the photolysis of ICl at 235.326 nm recorded using (a) He and (b) Xe as the carrier gas. (Bottom) Cl*-photofragment slice images following the photolysis of ICl at 235.195 nm recorded using (c) He and (d) Xe as the carrier gas.....	94

4.2.	KER distributions of $\text{Cl}(^2P_{3/2})$, $\text{Cl}(^2P_{1/2})$, $\text{I}(^2P_{3/2})$, and $\text{I}(^2P_{1/2})$ photofragments are shown in panels (a), (b), (c), and (d), respectively. The black and red lines represent KER distributions obtained using He and Xe as the carrier gas, respectively. The red marks indicate the peak position of the fast component: 1.81 and 2.55 eV in the case of $\text{Cl}(^2P_{3/2})$, and 2.50 in the case of $\text{Cl}(^2P_{1/2})$	95
4.3.	(Top) I-photofragment slice images following the photolysis of ICl at 235 nm recorded using (a) He and (b) Xe as the carrier gas. The experiment was performed with two colors. (Bottom) I*-photofragment slice images following the photolysis of ICl at 235 nm recorded using (c) He and (d) Xe as the carrier gas.....	97
4.4.	Speed distribution of Cl photofragments. The red line presents the fitted exponential function.....	100
4.5.	Speed Gaussian fit to the KER distribution of the Cl-photofragments. In the legend, n denotes the number of Xe atoms in the cluster, the second number the peak position in eV, and the percentage the contribution of each peak (cluster) to the total peak area without counting the residual peak (the broad peak at 1.5 eV).....	101
5.1.	Mass spectra of niobium oxide clusters Nb_xO_y^+ obtained at $V_{\text{grid}} \approx 0$, with beam crossing (dashed line) and without beam crossing (solid line). The Δ indicates the hydrated clusters (see text for details).....	112

5.2.	The fragmentation of the NbO_8^+ (a) and NbO_{10}^+ (b) clusters. The arrows with the labels indicate the kinetic energy and the size of the corresponding fragments.....	114
5.3.	Reflectron TOF spectrum of the mass-selected NbO_8^+ cluster, showing the fragments formed after collisions with Kr atoms in beam-gas cell arrangement.....	115
5.4.	The fragmentation of the Nb_2O_8^+ cluster.....	116
5.5.	Fragmentation cross sections of NbO_y^+ clusters. The values were obtained from the crossed beam (CB) experiments with secondary Ne beam at different laboratory collision energies (■ 1500 eV, × 1800 eV, + 500 eV) and the beam-gas cell (BG) experiments using Kr as the collision gas (O) at 1500 eV collision energy.....	118
5.6.	Comparison of experimentally determined fragmentation cross sections (CB experiments at collision energy 1500 eV), and calculated geometrical cross section for NbO_y^+ clusters.....	120
5.7.	Nb_2O_y^+ clusters fragmentation cross sections obtained from the crossed beam experiments at $E_{\text{Lab}}=1500$ eV and the calculated geometrical cross section for structures from Refs. 14 and 41.....	121

6.1.	Mass spectra of $Y_xO_y^+$ clusters (labeled as x,y) obtained at $V_{\text{grid}}=0$, with beam crossing (dashed line, red) and without beam crossing (solid line, black). The Δ indicates the hydrated clusters (see text for details).....	138
6.2.	Relative ion intensity of (a) YO_5^+ , (b) YO_7^+ , (c) YO_9^+ and (d) YO_{11}^+ versus retarding potential, with beam crossing (circles) and without beam crossing (squares). The arrows indicate the laboratory kinetic energies E_{Lab} of the corresponding fragment ions. The kinetic energy distribution of the ions is obtained by taking the negative differential.....	140
6.3.	Fragmentation of (a) $Y_2O_3^+$ and (b) $Y_2O_4^+$, with beam crossing (circles) and without beam crossing (squares).....	141
6.4.	The optimized cation ground-state and low-energy structures for the YO_{2k+1}^+ ($k = 1-6$) clusters along with bond lengths, multiplicities and relative energies RE.....	143
6.5.	Variation of the binding energy difference ΔE_b of the YO_{2k+1}^+ , ($k = 1-6$) cluster ions with the number of O_2 ligands.....	149
6.6.	Comparison of relative fragmentation cross sections of YO_y^+ clusters, obtained using different acceleration voltages V_{acc} , as a function of number of oxygen atoms, y	151

6.7. Comparison between the experimental (squares) and theoretical (circles) cross sections at 1500 eV laboratory energy. The experimental values have been normalized to the theoretical ones..... 153

LIST OF TABLES

Table

3.1.	KER spectra assignments for all channels.....	79
3.2.	Anisotropy parameter results.....	79
5.1.	Ratio of ions detected after collisions to the initial parent ions at different acceleration energies.....	124
6.1.	Fragmentation channels of $Y_2O_y^+$ clusters and their fragmentation products...	141
6.2.	Calculated structures (symmetries), multiplicities, total binding energies E_b , relative energies RE , and binding energy differences ΔE_b of YO_{2k+1}^+ clusters obtained at the DFT/B3LYP level of theory.....	144

Chapter I

Introduction

1.1. Theory

1.1.1. Light and matter interaction (absorption, emission, induced emission)

Light can be defined as an electromagnetic wave, which is the combination of an electric and a magnetic wave, having amplitudes E and B , respectively. These waves are at right angles and are described by Equation 1.1 and Equation 1.2, respectively.

$$E_y = E_0 \sin(2\pi\nu t - kx) \quad (1.1)$$

$$B_z = B_0 \sin(2\pi\nu t - kx) \quad (1.2)$$

In Equation 1.1 and Equation 1.2, E_0 and B_0 are the maximum amplitudes of the electric and the magnetic waves, respectively, and y and z are the directions of the vectors \vec{E} and \vec{B} . These waves have the same frequency $2\pi\nu$ and they are in phase since the constant k is the same. Figure 1.1 shows the electric and the magnetic component of plane-polarised radiation.* The

* Plane-polarised radiation was used for better illustration of the components.

polarisation plane is taken to be the plane that contains the direction of oscillation of the electric wave, E , and the direction of propagation. This is because usually any interaction between matter and electromagnetic radiation is taking place through the electric component.

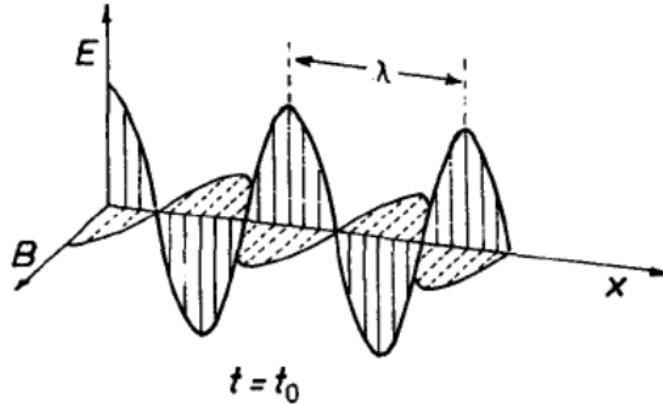


Figure 1.1. The variation of the electric and the magnetic component of an electromagnetic wave, with wavelength λ , as it propagates along the x-axis. Taken from Ref. 1.

Figure 1.2 illustrates a system (atomic or molecular) that consists of two states m and n (which may be electronic, vibrational or rotational). The energy separation between these states is ΔE .

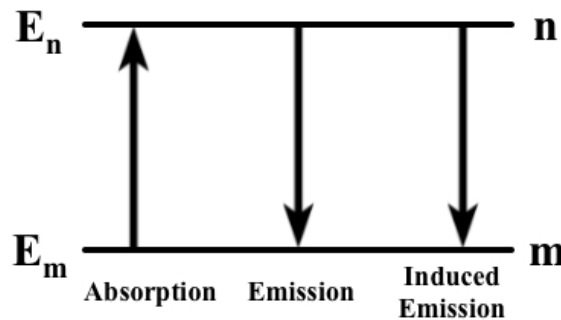


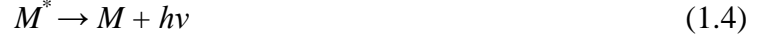
Figure 1.2. Absorption and emission processes in a two-state system. Reproduced from Ref. 2.

When this system interacts with electromagnetic radiation of appropriate energy, three different processes may take place:

Absorption: During this process the system, M , absorbs a photon and is excited from state m to state n .



1. **Spontaneous emission:** In this process, the excited system M^* (in state n), relaxes to state m by emitting a photon of energy ΔE .



2. **Induced emission:** This process is different from the spontaneous emission, because a photon of appropriate energy induces the relaxation of the excited system M^* from state n to state m .



The rate of change in population of state n during absorption is given by the following equation

$$\frac{dN_n}{dt} = N_m B_{nm} \rho(\tilde{\nu}) \quad (1.6)$$

Spontaneous and stimulated emission act in competition with absorption. The combined population change rate from these two processes is given by Equation 1.7.

$$-\frac{dN_n}{dt} = N_n (A_{nm} + B_{nm} \rho(\tilde{\nu})) \quad (1.7)$$

In Equations 1.6 and 1.7, A_{nm} and B_{nm} are the Einstein coefficients and $\rho(\tilde{\nu})$ is the spectral density of the radiation, which can be calculated using Equation 1.8.

$$\rho(\tilde{\nu}) = \frac{8\pi h c \tilde{\nu}^3}{\exp\left(\frac{hc \tilde{\nu}}{kT}\right) - 1} \quad (1.8)$$

When the system is at equilibrium, the populations N_m and N_n of the states m and n respectively, are connected through a Boltzmann distribution, as shown by Equation 1.9, in which g_n and g_m are the degeneracies of states n and m .

$$\frac{N_n}{N_m} = \frac{g_n}{g_m} \exp\left(-\frac{\Delta E}{kT}\right) \quad (1.9)$$

The Einstein coefficient is linked with the wavefunctions ψ_m and ψ_n of the states m and n , respectively, through the transition moment R_{nm} , which is given by Equation 1.10.

$$R_{nm} = \int \psi_n^* \mu \psi_m d\tau \quad (1.10)$$

Equation 1.10 refers to the interaction of the electric component of the radiation with the system, when an electronic transition is concerned. In this equation μ is the electric dipole moment operator, which can be calculated in the following way

$$\mu = \sum_i q_i r_i \quad (1.11)$$

where \vec{r} and q are the position vector and the charge of the particles.

The square of the transition moment, R_{nm} , is called the transition probability and it is connected to the Einstein coefficient through Equation 1.12, in which $|R_{nm}|$ is the magnitude of the vector \vec{R}_{nm} .

$$B_{nm} = \frac{8\pi^3}{(4\pi\epsilon_0)3h^2} |R_{nm}|^2 \quad (1.12)$$

1.1.2. Spin-orbit coupling

In the simplest case of a diatomic molecule, the orbital angular momenta of all electrons in the molecule are coupled producing L and all the spin momenta are coupled resulting in S . If there is no highly charged nucleus (i.e. heavy atom) in the molecule, the spin-orbit coupling between L and S is weak, and instead of being coupled to each other they are coupled to the electrostatic field created by the two nuclear charges. This case is known as Hund's case (a) and it is illustrated in Figure 1.3.

Due to the high strength of the coupling of vector L to the electrostatic field, the consequent frequency of precession about the internuclear axis is so high that the magnitude of L cannot be defined. This means that L is not a quantum number. Only Λ , which is the orbital angular momentum along the internuclear axis can be defined. Λ can obtain values 0, 1, 2, ...

The coupling of S to the internuclear axis is not affected by the electrostatic field. Instead it is affected by the magnetic field along the axis, which is created by the orbital motion of electrons. The component of S along the internuclear axis is Σ , which can have values $S, S - 1, \dots, -S$.

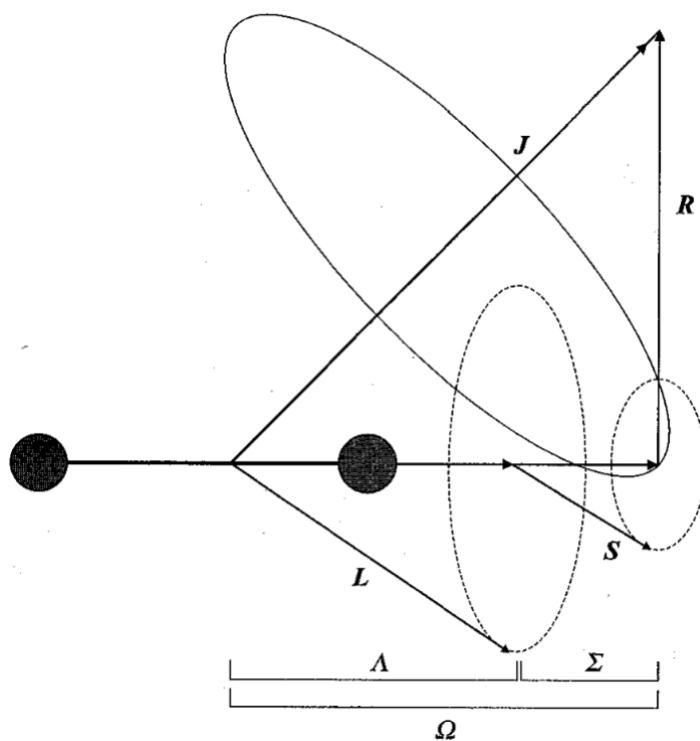


Figure 1.3. Schematic representation of Hund's case (a). Taken from Ref. 3.

The component of the total (orbital and spin) angular momentum along the internuclear axis, Ω , is given by Equation 1.13.

$$\Omega = |\Lambda + \Sigma| \quad (1.13)$$

Hund's case (a) is the one most commonly encountered. However, in the presence of a highly charged nucleus (heavy atom) in the molecule, the spin-orbit coupling might be sufficient,

so that L and S are not coupled to the electrostatic field of the nuclei. This case is depicted in Figure 1.3 and it is known as Hund's case (c). In Hund's case (c) L and S are coupled together, forming J_α which couples to the internuclear axis, along which Ω lies. In this case Λ is no longer a good quantum number and each state is labelled taking into account the value of Ω .

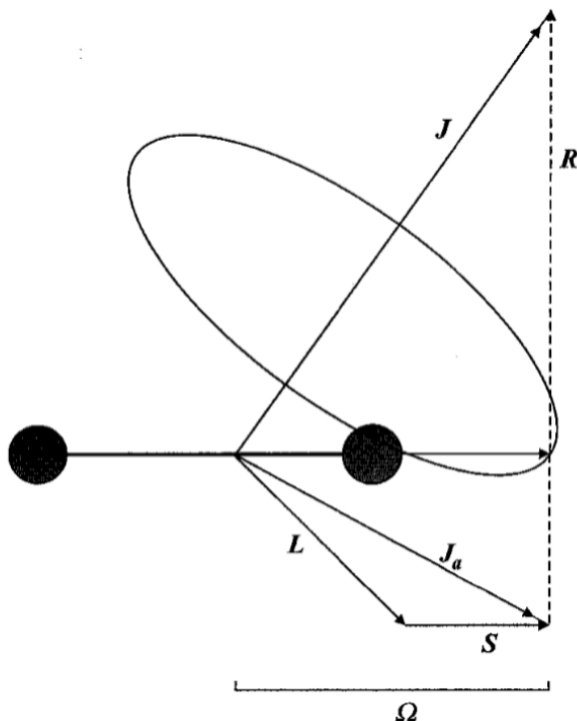


Figure 1.4. Schematic representation of Hund's case (c). Taken from Ref. 3.

1.1.3. Non-dissociative decay mechanisms

1.1.3.1. Jablonski diagrams

Electronically excited states, because of their formation by photon absorption, have excess energy. These excited states have relatively short lifetimes and there are several different ways to lose the excess energy and return to the ground state. The excited state deactivation pathways are traditionally represented by a Jablonski diagram (Figure 1.5).

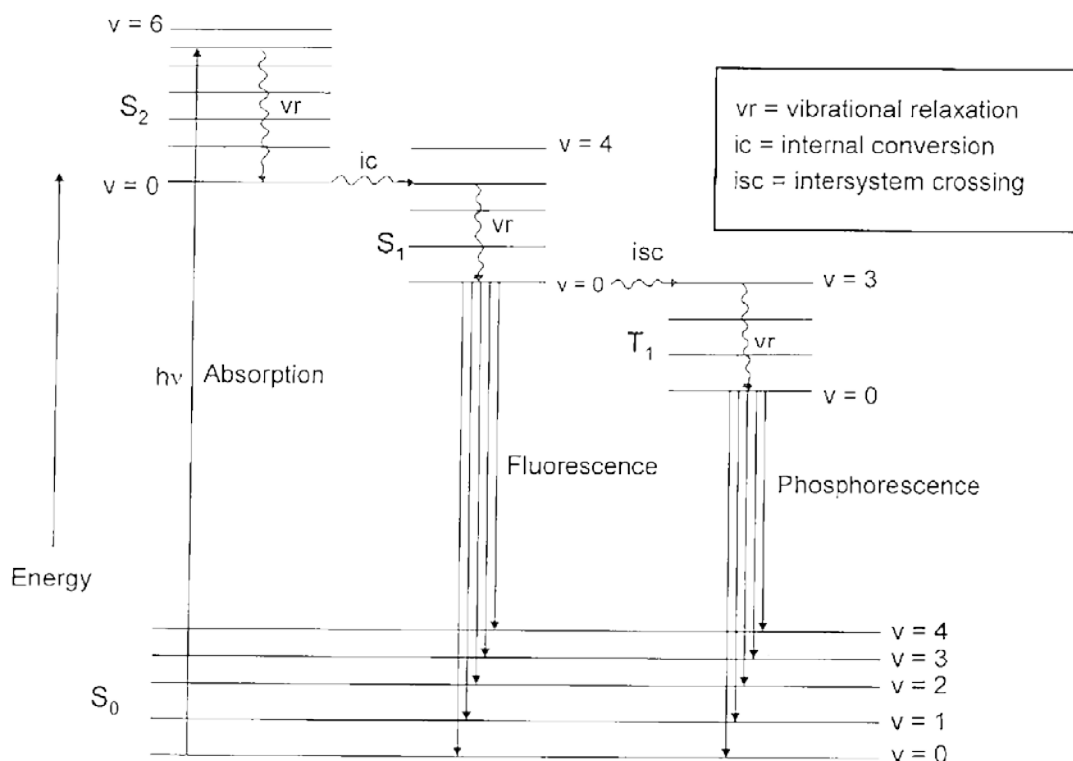


Figure 1.5. Jablonski diagram illustrating the photophysical processes in an electronically excited state. Taken from Ref. 4.

More specifically, a Jablonski diagram gives information for the following processes:

- The electronic states (singlets and triplets) and their relative energies. The states are denoted as S₀, S₁, T₁ etc.
- The vibrational levels associated with each electronic state.
- The possible, radiative or radiationless, transitions between the states.

In the following sections the possible deactivation pathways will be described in more detail. For generalisation purposes the processes described here concern photochemistry in non-isolated environments, e.g. solution phase. In the experiments presented in this thesis, which were carried out using molecular beams, vibrational relaxation does not occur due to isolation of the studied molecule.

1.1.3.2. Vibrational relaxation

After the initial absorption, the prepared electronically excited state is also associated with vibrational excitation. The only exception to this is when the electronically excited state is prepared by a transition to its ground vibrational level (0-0 transition). Vibrational relaxation (second step in Figure 1.6.) involves transitions between the excited vibrational state and the ground vibrational state of given electronic state. The excess energy is redistributed to other degrees of freedom of the system or it is transferred through collisions to the surroundings of the system.

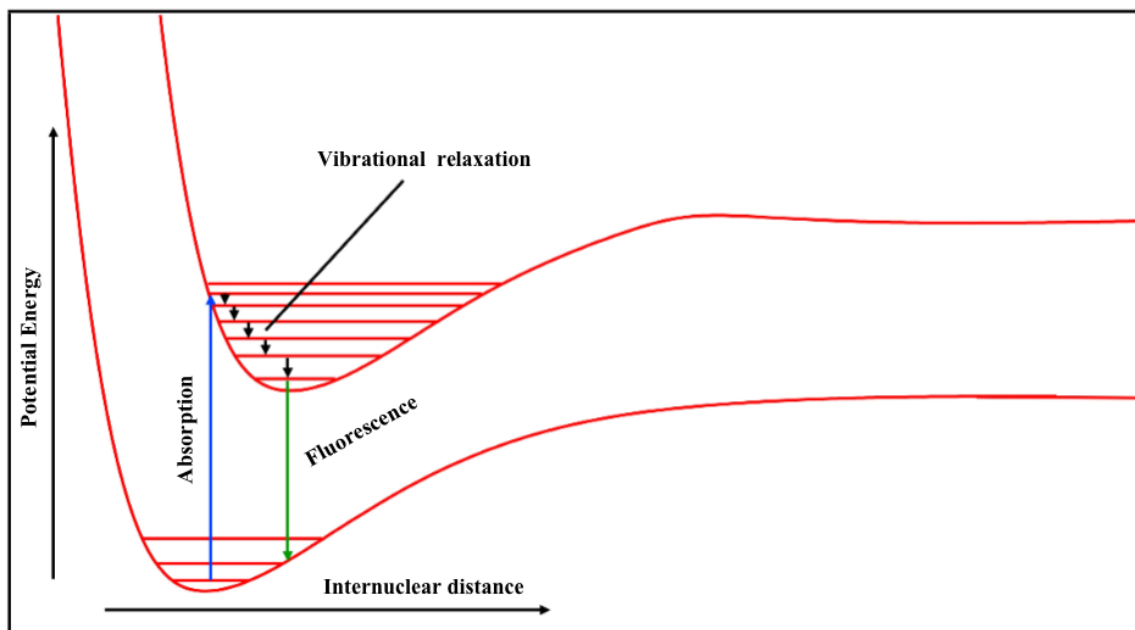


Figure 1.6. Steps leading to fluorescence. After the initial absorption to a vibrational level of an electronically excited state, the system relaxes to the ground vibrational level of the excited state by transferring energy to the surroundings. Then the fluorescence takes place to the ground electronic state.

1.1.3.3. Fluorescence

After the initial photon absorption, which excites the molecule to a vibrational level of an electronically excited state, the interaction of the system with its surroundings allows its relaxation to the ground vibrational level of the excited state. The photon absorption and the vibrational relaxation are the first two steps shown in Figure 1.6. Fluorescence (shown as the third step in Figure 1.6) involves the radiative transition between two states of the same multiplicity. This process takes place from the ground vibrational level of the lowest excited electronic state ($S_1, \nu = 0$) to the ground electronic state, S_0 , as described by Equation 1.14.



This process takes place in a vertical way, according to the Franck-Condon principle. A typical timescale for fluorescence emission is 10^{-9} – 10^{-6} s.

1.1.3.4. Internal conversion

Internal conversion (IC) is a radiationless transition from a higher energy electronic state to a lower energy electronic state of the same multiplicity. The small energy gap between the two vibrational levels allows the rapid energy transfer between the two electronic states.

When internal conversion takes place between two excited states, the energy transfer is so rapid that other radiative and non-radiative processes do not occur from the upper electronic state as they are unable to compete with internal conversion. When internal conversion occurs between an excited electronic state and ground state, the rate is generally much slower due to the greater energy gap. Typical timescales for internal conversion are 10^{-14} – 10^{-11} s when occurring between excited electronic states and 10^{-9} – 10^{-7} s when occurring between excited and ground electronic states.

1.1.3.5. Intersystem crossing

Intersystem crossing (ISC) deactivation mechanism involves a spin-forbidden transition between two electronic states of different multiplicity. After the initial excitation the system

relaxes through vibrational relaxation within the excited electronic state, just as in the case of IC (above). If one of the vibrational levels is isoenergetic with another vibrational level of a state with different multiplicity, there is some probability of a spin-forbidden transition to take place. This process is illustrated in Figure 1.7.

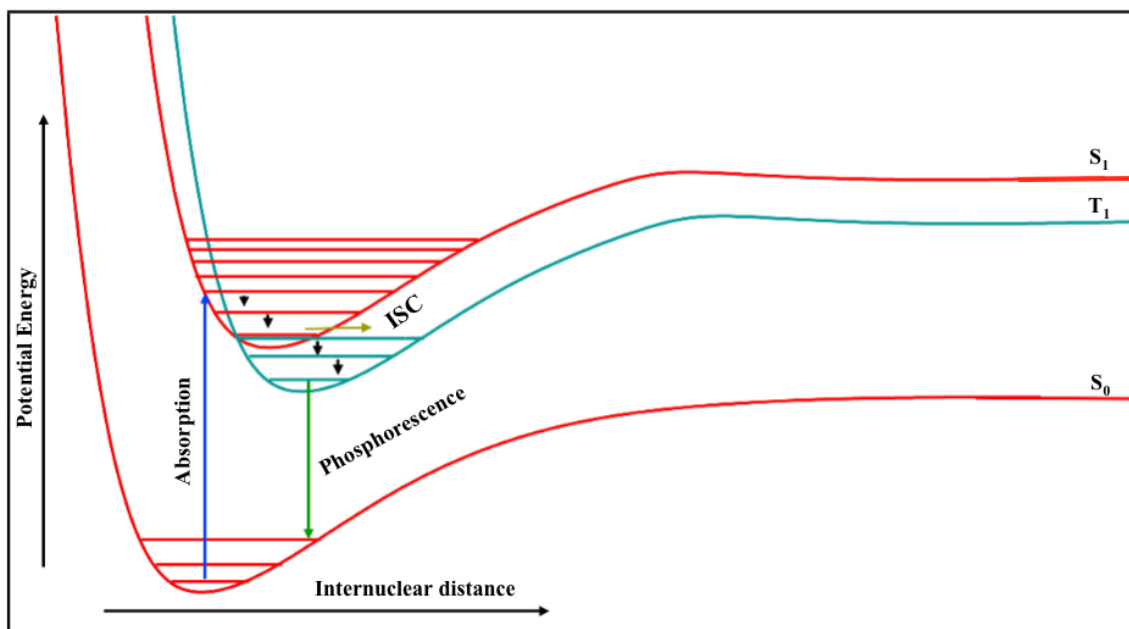


Figure 1.7. Steps leading to intersystem crossing. After the initial absorption to a vibrational level of an electronically excited state, a spin-forbidden transition between isoenergetic vibrational levels within electronic states of different multiplicity is occurring.

1.1.4. Dissociation mechanisms

1.1.4.1. Direct dissociation and the reflection principle

Direct dissociation is the simplest dissociation pathway. During a direct dissociation process the parent molecule is promoted to an excited electronic state via photon absorption. Following the photon absorption fragmentation takes place immediately without the presence of any barrier or other dynamical constraint. Due to this fact the lifetime of the excited state is extremely short (less than a vibrational period).

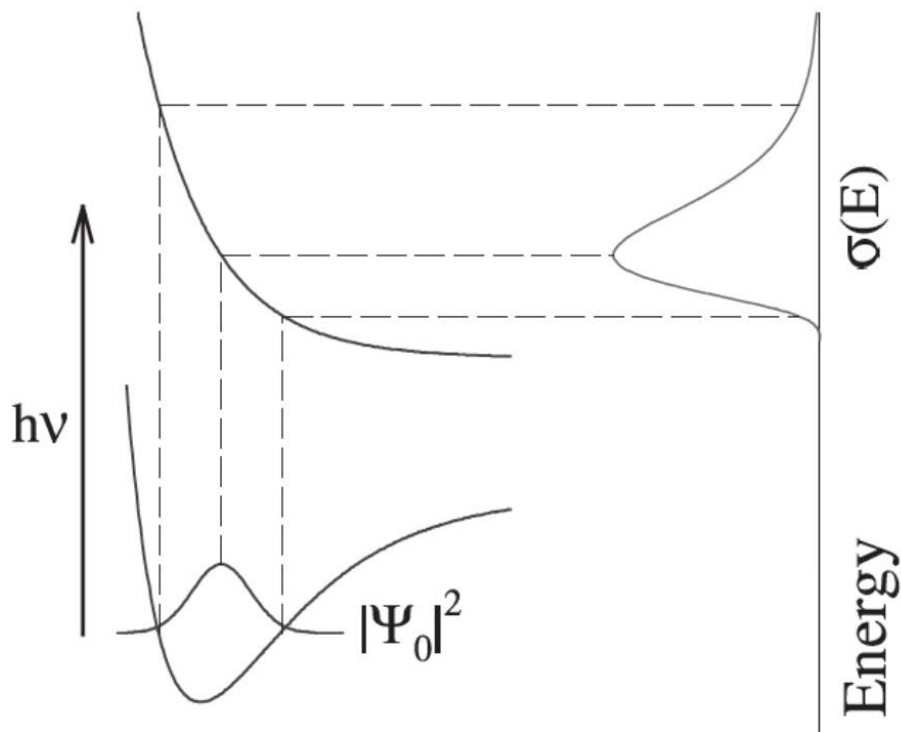


Figure 1.8. Schematic representation of the reflection principle. The ground state wavepacket is promoted onto an excited state surface after absorption of a photon. The absorption spectrum is the result of excitation process projection on an energy axis. Taken from Ref. 5.

Because of the very short lifetime of the direct dissociation process, the absorption spectrum and the state distribution of the products only depend on the initial state distribution of the parent molecule. This effect is known as the *reflection principle*⁵ and it is schematically illustrated in Figure 1.8.

1.1.4.2. Predissociation

A second type of dissociation mechanism is predissociation. In this case the dissociation proceeds on a different electronic state from the one to which the initial excitation took place. Many different variations of this mechanism exist, but they can be described as general cases detailed by Herzberg.⁶

Figure 1.9 illustrates the mechanism for a Herzberg type I predissociation process. After the initial excitation to a bound electronic state, internal conversion takes place to a dissociative state.

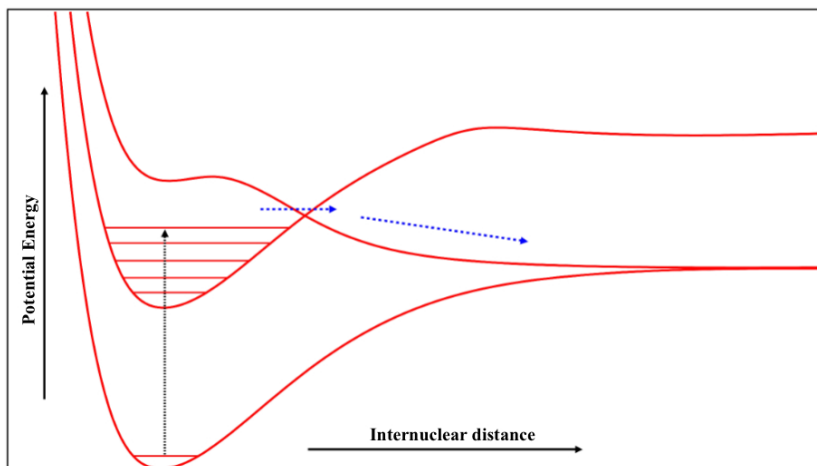


Figure 1.9. Schematic representation of Herzberg type I (electronic) predissociation

Often this happens via a conical intersection. The efficiency of this action depends on the position of the conical intersection between the two states in a multidimensional space and the coupling efficiency between the two states. If the coupling between the states is not so efficient, the predissociation is slow which leads to vibrational rearrangement in the excited state before the internal conversion. On the other hand, if the coupling is efficient, the predissociation is very fast leading to a continuum.

In Herzberg type II predissociation, which is depicted by Figure 1.10, the dissociation is preceded by specific vibrations of the molecular framework. In this mechanism the system needs to overcome a barrier through motions orthogonal to the dissociative coordinate. In an alternative case these motions are necessary for the system to go through a conical intersection.

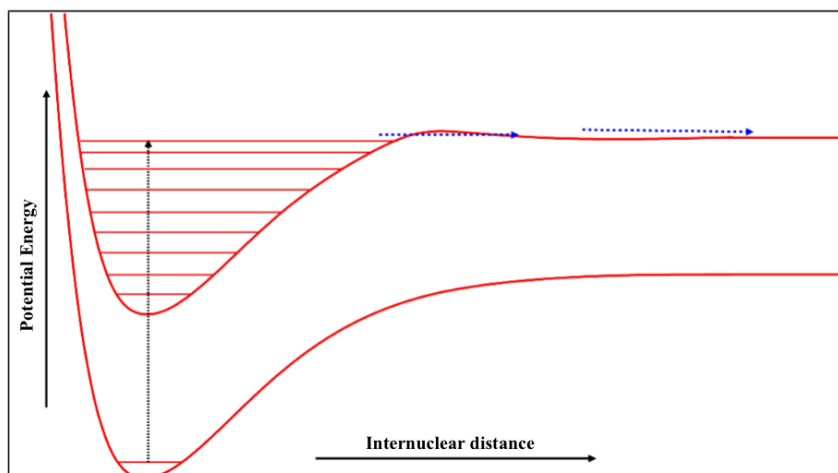


Figure 1.10. Schematic representation of Herzberg type II (vibrational) predissociation.

1.1.5. Clusters

1.1.5.1. Introduction

The physical and chemical properties of small atomic and molecular clusters have been the object of intensive experimental and theoretical investigations in the last few decades.^{7,8,9,10,11} Clusters play an important role in many different areas of scientific and common interest. The interest in clusters has been increased due to the rapid progress in nanosciences and nanotechnologies and their need for new materials. The novel molecules, such as metal oxide clusters can be possibly utilized in the future as building blocks to such new materials, which would exploit their unique properties. Clusters are vital components of the novel electronic, magnetic, and optical devices that are being developed everyday in nanotechnology centers throughout the world.

Clusters have been defined as aggregates of atoms or molecules ranging from dimmers to conglomerates of $\sim 10^n$ atomic or molecular units, where n may reach as high as six or seven. These species are held together by bonds other than covalent bonds, e.g., weak Van der Waals interactions, hydrogen, metallic or ionic bonds.

Their size is intermediate between individual atoms and molecules, and the condensed (bulk) phase of a particular substance. Clusters may be used to “bridge the gap” between the chemical and physical characteristics of isolated atoms and molecules in the gas phase, and the corresponding properties of their bulk materials. However, depending on the size and the certain system under investigation, the properties may be uniquely their own, i.e. they often have characteristics substantially different from their analogs in the molecular and bulk forms. These unique properties of clusters arise from a large number of:

1. energetically close isomeric structures, where the number of isomers grows huge with increasing cluster size
2. internal degrees of freedom, and
3. closely spaced energy levels.

Clusters, in general, are characterized by a high surface-to-volume ratio, but – at the same time – their small volume rapidly approaches bulk behavior. Thus they can provide bulk-like conditions and at the same time, because of their finite size, a possibility to measure observables, inaccessible in the bulk (e.g., fragments of photolysis of a molecule in cluster can escape from the cluster, while they are usually trapped in the bulk).

The method to form an intense beam of clusters depends on desired material and composition. In the case of rare gas and molecular clusters a high rate of particles can be delivered by a strong supersonic expansion, which is described in Section [1.1.5.2](#). Metal oxide cluster ions are relatively easy to produce using a number of generation techniques employed in modern cluster ion sources. For our experimental studies, the preferred method for producing gaseous metal oxide cluster ions is laser vaporization (ablation) of a pure metal target, described in Section [1.1.5.3](#).

Various mass-spectroscopic techniques are then used to analyze the size distribution of the produced clusters. In particular, time-of-flight (TOF) mass spectrometry (Section [1.2.1](#)) is a relatively simple and powerful tool. From the size distribution, i.e. from relative intensities of clusters in mass spectrum it is possible to obtain some information concerning cluster stability (identify the stoichiometries that are the most stable). The mass spectra of produced clusters

often shows local irregularities that are attributed to the particular stability of the corresponding clusters.

In our first slice imaging study on rare gas clusters, we observed changes in photochemical behaviour of pyrrole (Py) when seeded in Xe, and attributed this phenomenon to cluster formation between Xe and Py. We presented there a strong correlation between cluster formation and control of N-H bond fission. In the following study, the new experimental and theoretical results led to a detailed understanding of the control mechanism.

In our studies of transition metal oxide clusters, we have used photofragmentation spectroscopy¹² and later collision-induced dissociation (CID) to study the stability and the structure of transition metal oxide clusters. In the first of our photofragmentation studies on metal oxide clusters, we presented the mass spectra of the positive titanium oxide cluster ions Ti_xO_y^+ formed in our cluster source and we studied the interaction of UV photons with these aggregates.¹³ In the next study, we used photofragmentation of mass-selected clusters to explore further the fragmentation processes and pathways of small Ti_xO_y^+ clusters in a more controlled manner.¹⁴ Mass selected Ti_xO_y^+ clusters were also studied using standard CID technique with a beam cell.¹⁵ In our recent experiments, we studied the stability and the structure of iron-oxide clusters employing the beam-cell CID technique, and also a novel CID method based on crossed beams, recently developed in our lab.^{16,17} Detailed description of both techniques is given in Section 2.2.1.

1.1.5.2. Generation of rare gas clusters by supersonic expansion

Clusters are here formed in the adiabatic cooling process when streaming from a high-pressure region before the nozzle exit into the low-pressure vacuum chamber.

During a supersonic expansion the mean free path, λ , of the gas molecules is much smaller than the diameter of the nozzle orifice. This means that the molecules escaping through the hole experience many collisions. This kind of expansion can be described by the hydrodynamic-flow model. According to this model, the expansion takes place so rapidly that no

heat exchange occurs between the gas and the walls. Subsequently, the expansion is adiabatic and the enthalpy per mole of gas is conserved.

The total energy, E , of a mole of gas with mass M can be written as the sum of its internal energy $U = U_{trans} + U_{vib} + U_{rot}$, its potential energy pV and the kinetic flow energy $1/2Mv^2$ of the gas expanding into the vacuum with a mean flow $u(z)$ in the z direction. According to conservation of energy, the total energy before the expansion must be equal to the total energy after the expansion, as shown by Equation 1.15.

$$U_0 + p_0V_0 + \frac{1}{2}Mv_0^2 = U + pV + \frac{1}{2}Mv^2 \quad (1.15)$$

If the mass flow through the nozzle hole is small compared to the total mass of the gas, the assumption that the gas in the reservoir is in thermal equilibrium can be made. This assumption implies that $v_0 = 0$. Since the gas expansion takes place into the vacuum, the final pressure of the gas will be very small ($p \ll p_0$). Application of these approximations to Equation 1.15 leads to Equation 1.16, which describes a cold beam with small internal energy.

$$U_0 + p_0V_0 = U + \frac{1}{2}Mv^2 \quad (1.16)$$

When the flow velocity, v , exceeds the local velocity of sound $c(p; T)$, a supersonic expansion occurs. In an ideal case the internal energy after the expansion, U , would be equal to zero ($U = 0$). This means that $T = 0$.

The internal energy decrease leads to a decrease in the relative velocity of the molecules. In a microscopic ensemble of molecules, this effect can be understood in the following way. During adiabatic expansion faster molecules collide with slower molecules flying in front of them, transferring kinetic energy, as shown in Figure 1.11.

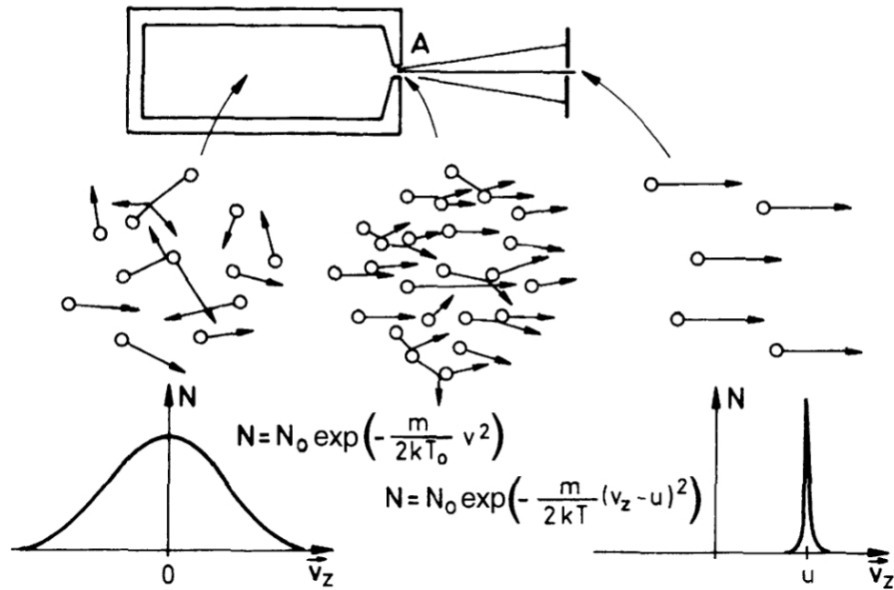


Figure 1.11. Molecular model of adiabatic cooling by collisions during expansion from a reservoir with Maxwellian velocity distribution into the directed molecular flow with a narrow distribution around the flow velocity u . Taken from Ref. 18.

The decrease of the relative velocity and the decrease of density result in the decrease of energy transfer. Head-on collisions (which have zero impact parameter) will narrow the velocity distribution, $n(v_{\parallel})$, of velocity components parallel to the flow direction. This velocity distribution can be described by a modified Maxwellian distribution, as shown by Equation 1.17 (where the flow direction is the z -axis).

$$n(v_z) = C_1 \exp\left(-\frac{m(v_z - u)^2}{2kT_{\parallel}}\right) \quad (1.17)$$

As shown in Figure 1.11, due to their small relative velocities Δv , atoms A or molecules M with mass m have the probability to recombine forming weakly bound systems A_n or M_n ($n = 2, 3, \dots$). This can happen if the small energy $1/2m\Delta v^2$ of their relative motion is transferred *via* collisions to a third body or the walls of the nozzle.

From a thermodynamic point of view, condensation occurs when the vapour pressure of the condensing substance becomes lower than the total local pressure. The vapour pressure in the

expanding beam, as described by Equation 1.18, decreases exponentially with decreasing temperature.

$$p_s = A \exp\left(-\frac{B}{T}\right) \quad (1.18)$$

The total pressure decreases as a result of the decreasing density in the expanding gas and the decreasing temperature, as shown in Figure 1.12. If enough collisions take place when $p_s \leq p_t$, then recombination and cluster formation can occur.

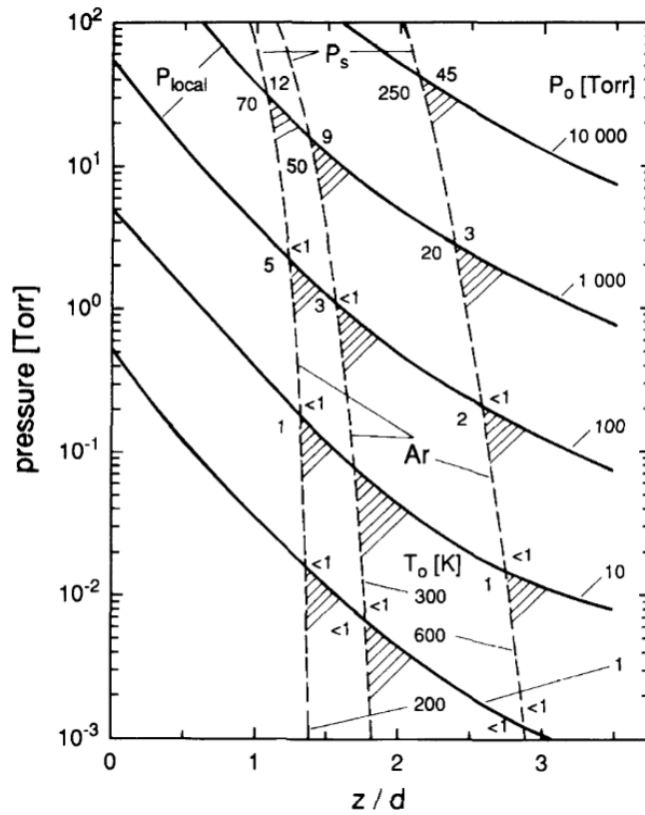


Figure 1.12. Vapour pressure p_s of argon and local pressure p_{loc} as a function of normalised distance $z^* = z/d$ from the nozzle for different stagnation pressures p_0 in the reservoir. Condensation can take place in the hatched areas. Taken from Ref. 18.

1.1.5.3. Generation of metal oxide clusters by laser vaporization

This technique makes use of the absorption of laser radiation by a surface of the target in the presence of O_2 . The metal rod is placed just in front of the nozzle orifice and irradiated by a laser beam. Laser pulses are focused onto a small spot on the surface which is typically 0.05–0.2 mm in diameter.¹⁹ When the laser radiation is absorbed at a solid surface, electromagnetic energy is converted first into electronic excitation and then into thermal, chemical, and mechanical energy to cause evaporation, excitation, and plasma formation. The created plume is a mixture of energetic species including atoms, molecules, electrons, ions and clusters. The plume, which has a highly directed dense shape, expands rapidly from the target surface in the vacuum chamber and is crossed perpendicularly, a few millimeters above the target surface with pulsed O_2 supersonic jet (or alternatively O_2 seeded in a carrier gas), as shown in Figure 1.13. The jet is introduced into the apparatus via a pulsed nozzle. Metal oxide clusters are formed in the plasma-oxygen jet mixing region as a result of association reactions between the metal atoms and ions contained in the plasma with the O_2 molecules.

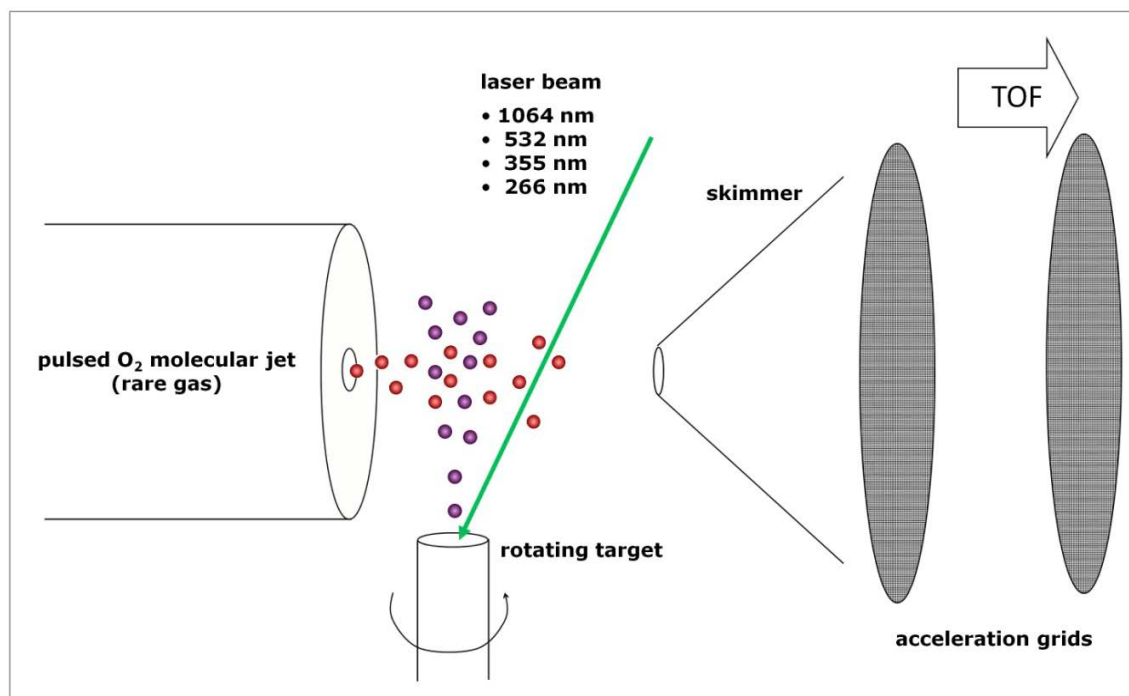


Figure 1.13. Laser ablation

The mixing of the laser ablated plasma with the O₂ in a plasma confining element, such as cluster growth channel, forms large M_xO_y (M = ablated metal atom) clusters with a broad range of stoichiometries. In such a closed space, the cluster growth is assisted by multiple collisions between the O₂ molecules and the metal ions. The cluster source used in our lab is an open configuration laser vaporization source without a cluster growth channel, i.e. with free expansion of the laser ablated plume and O₂ molecular beam in vacuum. After the laser ablation from a metallic surface, the clusters are formed exclusively by collisions in the mixing region of the ablation plume with the O₂ molecular beam. This results in production of clusters of the type M_xO_y, containing only one metal atom, as previously seen.^{17,20,21,22} This observation is different from some previous experimental studies,^{23,24,25,26} where a narrow channel was employed to promote the growth of smaller clusters into larger ones by multiple collisions.

1.2. Experimental techniques

1.2.1. Mass Spectrometry

Mass spectrometry (MS) is a method of quantitative, qualitative, isotopic and structural chemical analysis, based on the difference in molecular masses. The basic principle of MS is to convert analyzed sample molecules, either inorganic or organic compounds, into the form of ionized gas, to separate these ions according to their mass-to-charge ratio (m/z), and to detect them qualitatively by their respective m/z , and quantitatively in proportion to their abundance. A mass spectrum of the molecule is thus produced, as a plot of ion abundance versus m/z . The creation of positive ions of sample molecules is described by Equation 1.21:



where M is the sample molecule, $M^{+\bullet}$ is the molecular ion (a radical cation with an odd number of electrons) and e^{-} is ejected electron. The measured quantity in a mass spectrometry experiment is the m/z ratio, with m being the ion's mass and z the ion's charge. In most cases, a singly charged ion is formed, so the m/z is equal to the mass of the ion. Since the mass of the ejected

electron is very small, it is assumed that the mass of the molecular ion is equivalent to the mass of the neutral sample molecule.

1.2.1.1. Ionisation and fragmentation

The ionisation process can take place using a variety of sources - the sample may be ionized thermally, by very strong electric fields or by impacting energetic electrons, ions or photons. Some ionization techniques are very energetic and transfer to the system much more energy than what is needed for the ionisation. The excess energy can be redistributed as electronic, vibrational and rotational excitation of the molecular ion. This excitation (especially vibrational) may lead to fragmentation via two different fragmentation pathways (described by Equation 1.22 and 1.23).



Equation 1.22 describes the formation of a cation with an even number of electrons and a radical, whereas Equation 1.23 describes the formation of a new radical cation and a molecule. Fragmentation of the radical cation $M^{+\bullet}$ usually occurs by expulsion of a radical species leaving an even-electron cation. (Equation 1.22). This ion (A^+) may fragment further by loss of closed-shell molecules to form another even-electron ion. This is generally referred to as the even electron rule.

1.2.1.2. Linear time-of-flight (TOF) mass spectrometer

Several mass-spectroscopic techniques have been developed, among which time-of-flight (TOF) mass spectrometry is a relatively simple and powerful tool. Figure 1.14 displays a schematic representation of a Wiley-McLaren linear time-of-flight (TOF) mass spectrometer.²⁷ The analyser consists of two accelerating regions (s and d) and a field-free region D , as shown in Figure 1.14. The Wiley-McLaren technique uses two flat ring electrodes covered with a very fine mesh grid to form a homogeneous electric field along the TOF axis.

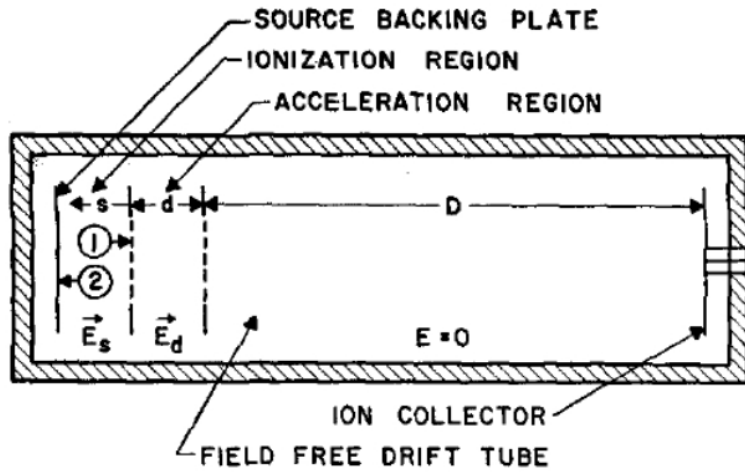


Figure 1.14. Schematic representation of a Wiley-McLaren time-of-flight mass analyser. Taken from Ref. 27.

The ions are created between the first two electrodes and accelerated out of the source into the field-free drift region. Each ion with mass m and total charge $q = ze$ is accelerated by a potential U . The electric potential energy, E_{el} , is converted into kinetic energy, E_k of the ions, as shown by the following equation:

$$E_k = E_{el} = \frac{mv^2}{2} = qU = zeU \quad (1.24)$$

Thus, all the ions with the same charge acquire the same kinetic energy during the acceleration step. Following their acceleration, the ions are moving with constant speed through the field-free region towards a detector. From Equation 1.24 the speed v of the ions can be expressed in the following way:

$$v = \left(\frac{2zeU}{m} \right)^{1/2} \quad (1.25)$$

The necessary time for the ions, to cover the length L of the drift tube, is given by Equation 1.26

$$t = \frac{L}{v} \quad (1.26)$$

Combination of Equation 1.25 and Equation 1.26 leads to an expression of the mass-to-charge ratio, m/z , as a function of the time-of-flight, t :

$$\left(\frac{m}{z}\right)^{1/2} = \left(\frac{\sqrt{2eU}}{L}\right)t \quad (1.27)$$

From Equation 1.27 can be seen that the ions are separated based on the different mass to charge ratio (m/z) during their flight towards the detector. Taking into account that the drift tube length, L , and the acceleration potential, U , are constant for a specific spectrometer, the terms in the parenthesis of Equation 1.27 can be replaced by a constant A , indicating that the relationship between \sqrt{m} and t is linear as shown in Equation 1.28:

$$\left(\frac{m}{z}\right)^{1/2} = At + B \quad (1.28)$$

The constant B is added in order to allow the correction of the measured time zero, which may not correspond to the true time zero.

1.2.2. Resonance enhanced multi-photon ionization (REMPI)

For the study of high energy electronic states in a single photon experiment, the absorption of a vacuum ultraviolet (VUV) photon is necessary. However, the generation of VUV radiation, using lasers, is not a routinely performed process. Alternatively, these high energy states can be studied using multiphoton transitions and photons with wavelengths in the visible or near ultraviolet range. One of the most widely used multiphoton techniques is resonance enhanced multiphoton ionisation (REMPI).

REMPI is a process occurring in two separate steps. In the first step, absorption of one or more photons leads the system to an electronically excited state. For this kind of process to take place the following conditions must be valid:

- The light intensity should be high enough to allow the simultaneous absorption of multiple photons.
- The combined energy of the photons must satisfy the resonance condition $E_2 - E_1 = 2h\nu$.

- All the selection rules must be satisfied.

In the second step of a REMPI process the excited system absorbs one or more photons to climb above its ionization limit. The total ionization probability of a system decreases as the number of the photons needed increases. However, a REMPI process has much larger probability to occur than the equivalent non-resonant process.

Depending on the system, a variety of REMPI schemes can be used. As shown in Figure 1.15(a), both the resonant excitation to the high lying intermediate state and the ionization step can be done using one laser (i.e. photons of the same energy). This case is known as a one-colour ionisation scheme (1+1 REMPI). However, two lasers may be used in a so-called two-colour experiment. In this kind of experiment the first laser is used to excite the system to the intermediate state and the second laser, which is tuned to a different wavelength, is used for the ionization step (1+1' REMPI). This process is schematically represented in Figure 1.15(b).

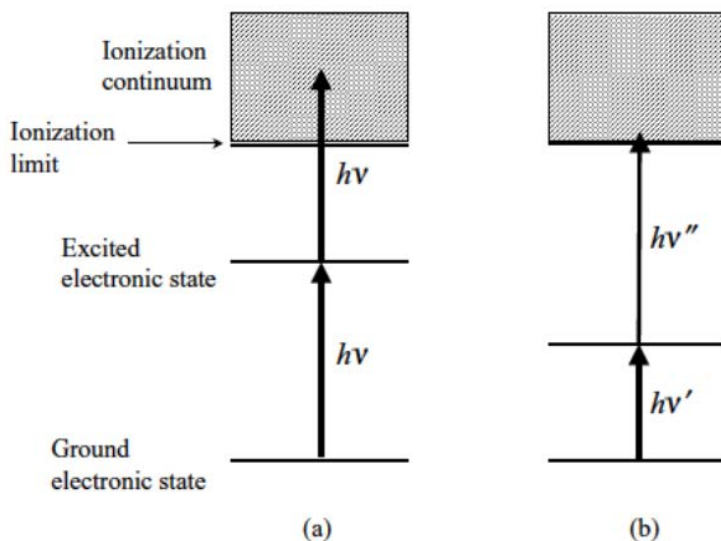


Figure 1.15. (a) One- and (b) two-colour resonance enhanced multiphoton ionization (REMPI) schemes.

Taken from Ref. 28.

The notation used for a one-colour REMPI process has the form $(m + n)$, where m is the number of photons used for the excitation step and n is the number of photons used for the

ionization step. When a two-colour REMPI scheme is used the notation takes the form $(m + n')$, denoting that the photons have different energies.

1.2.3. Velocity map imaging

Ion imaging is a multiplex detection technique which allows the simultaneous measurement of rotational, vibrational, electronic and kinetic energy release of products of unimolecular and bimolecular reactions. It was first demonstrated by Chandler and Houston in their pioneering study of 1987 "Two-dimensional imaging of state selected photodissociation products detected by multiphoton ionization".²⁹ Even though the energy resolution was limiting low around 15%–20%, it was shown for the first time that ion imaging could be applied in the field of molecular reaction dynamics in order to obtain insights on the photodissociation dynamics.

Eppink and Parker introduced Velocity Map Imaging (VMI) that improved the relatively low resolution in 1997.³⁰ Velocity map imaging is based on the use of an inhomogeneous extraction field to accelerate and focus ions onto the imaging plane in such a way that their arrival positions depend on the initial velocities only, i.e. all ions with the same velocity will hit the detector at the same point, regardless the exact position of their creation. By extracting all the ions along a direction normal to the detector's surface, we are in essence projecting the 3D velocity distribution onto a two-dimensional (2D) plane.

The main advantage of velocity map imaging is thus the ability to map velocity independent of origin of formation, and without grids – transmission is thus 100% and without grid distortions. In a nutshell, the VMI experiment involves the following experimental steps:

1. Photodissociation of molecules in a molecular beam using a linearly polarized laser with the polarization direction parallel to the detector face.
2. Conversion of the photofragment molecules into ions by a state-selective REMPI scheme by using a second laser (colour) with polarization parallel to the detector face.
3. Projection of the ion spheres onto a two-dimensional (2-D) detector which is time-gated to detect the species of interest.

4. Mathematical transformation of the 2-D image back to the three-dimensional data of step (i) and subsequent analysis for speed distribution and angular distribution extraction.

1.2.3.1. Newton spheres

The target of the molecular dynamics field is the full understanding of physical or chemical processes (chemical reactions, photoionisation, photodissociation). For the accomplishment of this goal the knowledge of the potential energy surface of the process and the dynamics on this surface are necessary. Specification of the properties of the reactants (internal temperature, rotational angular momentum, etc.) and characterisation of the products, using simplified models, can lead to understanding of a particular process. The majority of processes described in this thesis are simple unimolecular events, namely photodissociation and photoionisation, which are described by Equations 1.19 and 1.20, respectively.



Let us consider the photodissociation process described by Equation 1.19, following the energy conservation principle. We have that Total Kinetic Energy Release (TKER), i.e. the total excess energy left over after subtracting the internal energy of the A and B products.

$$TKER = KER_A + KER_B = h\nu - D_0(AB) - E_{\text{int}}(A) - E_{\text{int}}(B) \quad (1.21)$$

where D_0 is the bond dissociation energy, and KER and E_{int} the fragment's kinetic and internal energy, respectively.

Every photodissociation or photoionisation event produces two counter-fragments, which have equal momentum but fly towards opposite directions. The conservation of momentum relates the momentum and thus the velocity vectors of the nascent fragments as:

$$m_A \mathbf{v}_A + m_B \mathbf{v}_B = 0 \quad (1.22)$$

Conservation of momentum and energy results in the kinetic energy partitioning:

$$\begin{aligned}
 KER_A &= \frac{M_B}{M_{AB}} \times TKER \\
 KER_B &= \frac{M_A}{M_{AB}} \times TKER
 \end{aligned}
 \tag{1.22}$$

Thus, in the case of photoionization $M_e \ll M_{M^+}$, the photoelectron receives essentially all $TKER$.

Repetition of the same event many times leads to the formation of spherical distributions of fragments, which are known as Newton spheres. The size of the Newton spheres is proportional to the fragment's speed, and gives information about the distribution of internal and translational energy of the specific process.

Figure 1.16 shows schematically creation of the Newton spheres by laser photodissociation of molecule AB to fragments A and B, where $m_A < m_B$.

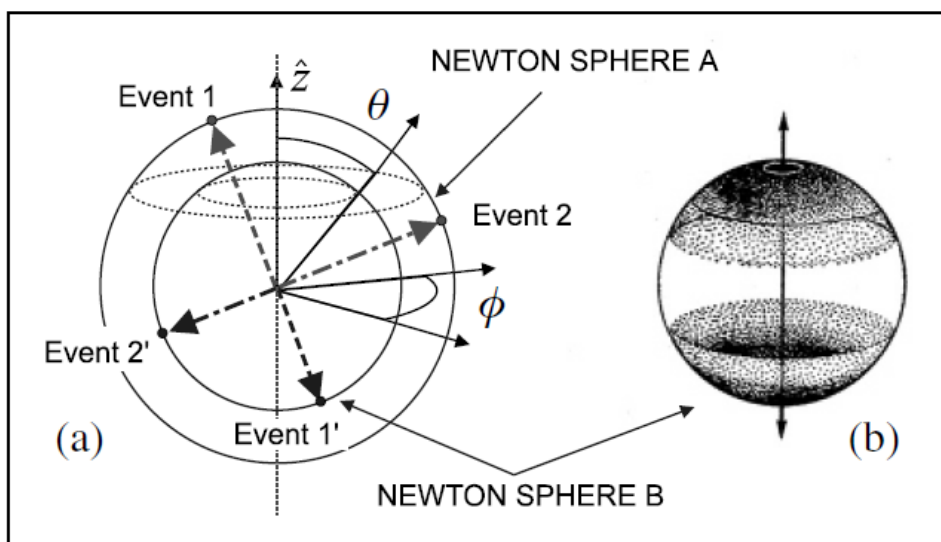


Figure 1.16. (a) A pair of Newton spheres with spherical coordinates r (not shown), θ , and ϕ , where θ is the polar angle defined with respect to the z axis (vertical axis in the figure), ϕ is the azimuthal angle, and r is the sphere radius. Two events are shown in (a) with equal and opposite momentum. (b) By summing up a large number of events (here for particle B), a surface pattern emerges as shown. Most of the surface intensity of this example is at the poles, representative of a typical $\cos^2\theta$ distribution. Taken from Ref. 31.

In the ideal case, all the parent molecules AB are located at the same origin $(x,y,z=0,0,0)$ without a spread in the origin $(\Delta x,\Delta y,\Delta z=0,0,0)$, and with zero initial velocity $(v_x,v_y,v_z=0,0,0)$ without a velocity spread $(\Delta v_x,\Delta v_y,\Delta v_z=0,0,0)$. In the first dissociation event shown in Figure 1.16, fragment A is sent upwards and B downwards, while in the second event the two fragments are sent again in opposite directions but with a different polar angle θ . Each dissociation event results in fragments with identical speed, but the fragments recoil along varying directions (velocities). Every fragment A falls somewhere on the Newton velocity sphere A, and the same applies for B. When summing up the measurements of the A and B velocities for a large number of events (Figure 1.16(b)), any pattern that might appear on sphere A is identical to the pattern observed for Newton sphere B.

1.2.3.2. Velocity map imaging of photodissociation

In the field of molecular dynamics research, velocity map imaging has made a great impact in photodissociation of diatomic and small polyatomic molecules. Small molecules dissociate into smaller fragments with a limited number of internal energy states, leading to widely spaced and thus more resolvable product Newton spheres.

From product photofragment images of a hypothetical diatomic molecule AB, we can quantify the most important photodissociation properties: the A–B bond energy of the ground state, the symmetry of the ground and excited states, product yields for various dissociation channels, angular distributions etc. For example, from the product KER distribution and from energy balance the internal state distribution of both fragments can be determined.

The surface pattern of the Newton sphere of photodissociation fragments is characterized via the beta (β) parameter and higher order alignment parameters as needed. Direct dissociation of a diatomic molecule occurs on a time-scale much shorter than a classical rotation period. The fragments recoil instantly parallel or perpendicular to the polarization direction of the light field, with an angular distribution given by the equation:

$$I(\theta) = [1 + \beta P_2(\cos\theta)] / 4\pi \quad (1.22)$$

In this equation θ is the angle between the light polarization direction and the direction of the recoil of the fragments, as shown in Figure 1.16, and $P_2(\cos\theta) = (3\cos^2\theta - 1)/2$ is Legendre polynomial of second order. The parameter β in this expression is equal to 2 for a parallel transition, $I(\theta) \sim \cos^2\theta$, and -1 for a perpendicular one, $I(\theta) \sim \sin^2\theta$. In general, the value of β lies in between these extreme values, and can fall short of these limiting values because of some rotation of the molecular axis while the products separate from one another. For $\beta = 0$, the angular distribution is isotropic in space.

1.2.3.3. The velocity mapping experiment

A velocity map imaging experiment of a photodissociation process involves many steps as shown in Figure 1.17(A). The first step is the creation of Newton spheres by photodissociation of a molecule, which is introduced to the vacuum chamber in the form of a molecular beam. The parent molecules should have preferably narrow distribution of quantum states, which is easily obtained by seeding the molecule (without clusters formation) in the cold supersonic jet expansion of a pulsed molecular beam.

After photodissociation the photofragments are state-selectively converted to ions by resonant enhanced laser ionisation. Since the mass of the photoelectron is negligible compared to the mass of the ion ($M_{e^-} \ll M_{M^+}$), and the photoelectron receives essentially all *TKER*. Thus, the ejection of an electron by the ionization laser does not change the original recoil velocity of the photofragments significantly, and its position at any time following the photolysis is nearly the same as it would have been as a neutral. Thus, the three-dimensional (3D) velocity distribution of the ions will be identical to the 3D velocity distribution of the nascent photofragments.

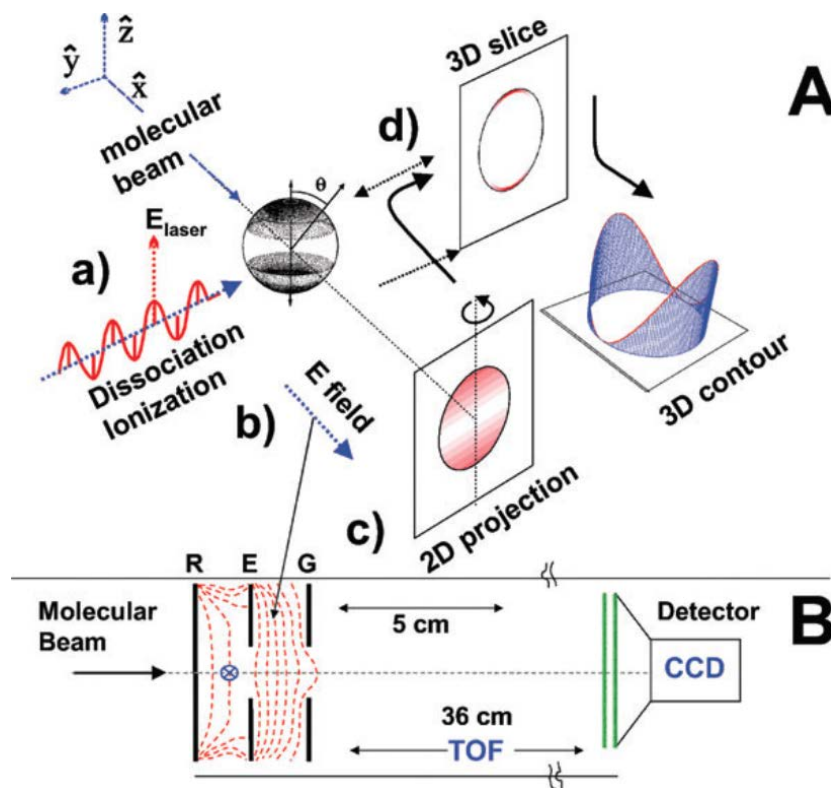


Figure 1.17. (A): The imaging approach for measuring Newton spheres from photodissociation. (a) Photodissociation of molecules in a molecular beam using a linearly polarized laser. (b) Conversion of the photofragment molecules making up the Newton spheres into ions by laser ionization. (c) Projection of the ion spheres onto a two-dimensional (2-D) detector. (d) Mathematical transformation of the 2-D image back to the three-dimensional data of step (a). (B): Schematic representation of the electrostatic lens used for velocity map imaging of photodissociation. Taken from Ref. 32.

The expanding ionic Newton spheres are then accelerated and projected onto a 2D position sensitive detector using ion optics. The VMI ion optics configuration is very similar to the Wiley-McLaren arrangement, the only difference is that for VMI the two grid electrodes are replaced by a pair of flat electrodes with circular opening of finite radius, forming electrostatic lenses. Figure 1.17B depicts a basic design of an electrostatic lens used for the acceleration of the ionic Newton spheres. This electrostatic lens is an assembly of three electrodes. The first is the repeller (R), the second is the extractor (E) and the last is a ground electrode (G). The electrodes are plates of 70 mm diameter with the electrode spacing of 15 mm, and the holes are for the repeller 1 or 2 mm and 20 mm for extractor and ground electrode. Application of voltages on these electrodes leads to the creation of an inhomogeneous electric field, whose potential

contours are bent and are the optical analogy of a lens. A skimmed molecular beam passes through a small hole in the repeller plate. Laser beam crosses the molecular beam between the repeller and the extractor and forms ions, which are then accelerated and fly through the TOF tube to the imaging detector.

In the case of a photofragment recoil with the initial velocity v_y , perpendicular to the detection axis x , most of the ions lie at the outer edge of the disk with a radius R :

$$R \approx v_y \times \text{TOF} \approx D(\text{KER}/qV)^{1/2} \quad (1.23)$$

where KER is kinetic energy release of the photofragment, D is the length of the field-free region of TOF tube, q the photofragment charge, and V the accelerating voltage. The TOF of the photofragment with the mass m is given by the equation:

$$t \approx D / v_x \approx D(m/2qV)^{1/2} \quad (1.24)$$

These equations imply that if the detector is gated at the proper time of flight t , corresponding to the mass m of the photofragment, all particles with the same kinetic energy will appear at the same radius R on the detector.

Eppink and Parker showed that by adjusting specific ratio of the potential of the repeller and the extractor V_E/V_R (simply by changing the extractor voltage) all ions with the same initial velocity $\{|v_x|, v_y, v_z\}$ arrive at the same point in the focal plane, irrespective of their point of formation. The "focusing" is important because the molecular beam has a finite width on the order of few millimeters. Thus dissociation takes place at different positions in the molecular beam and this spatial spread results to blurring of the image and limiting velocity resolution.

The final step is the mathematical reconstruction of the projection, which leads to the recovery of the initial 3D distribution. To extract quantitative data from the 2D images one needs to reconstruct the 3D velocity distribution. For photodissociation experiments, in which linearly polarized lasers are commonly used, the configuration is such that the polarization direction of the photolysis and probe lasers are maintained parallel to each other and to the imaging plane. The resulting photofragment angular distribution is cylindrically symmetric and thus an inverse Abel transform can be applied to extract the 3D distribution.^{33,34} The reconstructed images

represent the intensity profile of planar cuts through the 3D distributions along the symmetry axis, i.e., they are equivalent to polar plots of the photofragment angular distributions $I(\rho, \theta)$, where ρ is the distance from the center of the image and θ the polar angle with respect to the symmetry axis.

1.2.4. Slice imaging

Slice imaging³⁵ represents a new approach to the widely used methods of two-dimensional (2D) ion imaging and velocity map imaging (VMI). In these conventional methods inverse Abel transformation is used in order to invert the two-dimensional (2D) images to give the full three-dimensional (3D) speed distribution of photofragments from molecular photodissociation. The final result of the inverse Abel transformation is the center slice of the photofragment distribution. In order to use the Abel transform, images have to possess an axis of cylindrical symmetry parallel to the imaging plane. For two color experiments, such cylindrical symmetry is achieved when both the photolysis and probe laser polarization directions are parallel to each other and the imaging plane. One disadvantage of using the Abel transformation is introducing an artificial noise, particularly that along the symmetry axis.

In this alternative approach to ion imaging, introduced by Kitsopoulos and coworkers³⁵, the photofragment speed and the angular distributions are measured directly from the images without the need of inverse Abel transformation. This is achieved by using delayed pulsed extraction of the ions formed following photodissociation. Delaying the extraction field with respect to laser ionization causes a sufficient velocity spread in the ion cloud such that the time width of the ion packet at the detector is on the order of 500 ns. In addition, a narrow detector time gate is used (40 ns) to acquire only the *center slice* of the ion packet. The resulting image is equivalent to that obtained in VMI experiment after performing the inverse Abel transformation, however, the artificial noise introduced by this transform is eliminated. The performance of the slice imaging method remains comparable to that achieved with the VMI method.

In their later study Papadakis and Kitsopoulos³⁶ showed that it is possible to perform velocity map imaging and slice imaging using a single field consisting of two electrodes, which represents an improvement of the multielectrode geometries used before. In this new design a

single repeller and a grounded extractor are sufficient to achieve both velocity mapping and slicing. The energy resolution of this new geometry is competitive to the multielectrode ones - for imaging both photoelectrons and photofragments a resolution of $\sim 1\%$ in velocity is achieved. Besides its compactness, the advantages of this new geometry are its ability to focus large volumes. Another advantage of the method is its achromaticity – in a typical VMI the focal plane of the particles with different initial center of mass velocities (different initial KER) does not overlap with the detector plane, whereas in this this method the focusing is independent on of the initial velocity.

In order to achieve focusing the starting position of the particles along the TOF axis has to be at a specific distance from either the repeller or the extractor. Unlike the existing VMI and slicing methods where the focusing is achieved by adjusting the voltage on the second field (ion lens) in this new geometry the focus is found by moving the laser position along the TOF axis. They also performed ion trajectory simulations using SIMION 7.0³⁷ and showed that the focusing is maintained, independent of the repeller voltage.

A scheme of a conventional ion imaging setup is presented in Figure 1.18. Ions are fomed in a homogenous extraction field E and accelerated towards the position-sensitive imaging detector (PSD). The extraction field is coupled to a field-free drift region of length L that prolongs the flight time of the ions towards the detector and allows mass resolution.

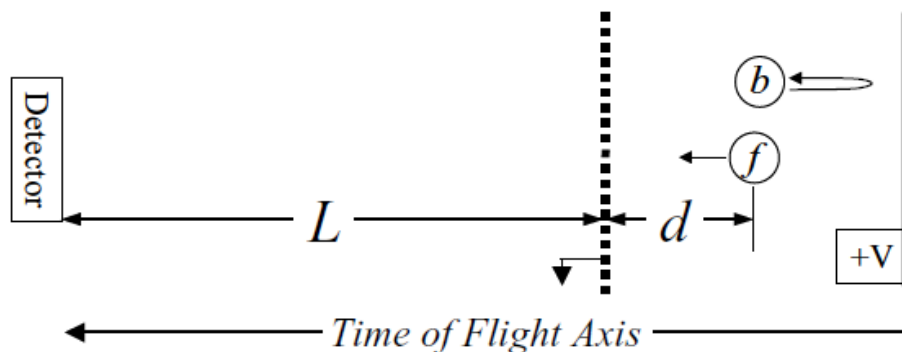


Figure 1.18. Typical ion imaging setup, consisting of a homogenous extraction field E , a drift region of length L and a position-sensitive detector (phosphor screen in combination with a CCD camera).

In addition this field-free region allows sufficient time for the ion cloud to expand in diameter, in the plane parallel to the detector plane, thus achieving better energy resolution. The time-of-flight T of an ion of a given mass m and charge q is given with the Equation 1.25.

$$T(d, v_0) = \frac{1}{a} \left[\sqrt{v_0^2 + 2ad} - v_0 \right] + \frac{L}{\sqrt{v_0^2 + 2ad}}, \quad (1.25)$$

where v_0 is the component of the initial velocity along the TOF axis, $a = qE/m$ is the acceleration of the electric field, and d is position of the particle with respect to the extractor electrode. The value of the initial particle velocity v_0 is positive for the particles initially scattered towards the detector (“forward” – f), and negative for those initially moving away from the detector (“backward” – b). The initial velocity v_0 becomes:

$$v_0 = c + u_0 \cos(\alpha) \quad (1.26)$$

where c is the velocity of the molecular beam, u_0 is the photofragments recoil velocity, and α is the angle between the direction of the photofragments and the TOF axis.

The ion trajectory simulations³⁶ of a photofragment imaging experiment following the photodissociation of a diatomic molecule ($A_2 \rightarrow 2A$) showed that for this case of direct extraction (constant DC extraction field) there is always *crushing* of the ion Newton sphere along the TOF axis. The ion trajectories revealed that although the vertical dimension of the ion cloud (Δy) spreads considerably during its flight towards the detector, the horizontal size (Δx) remains nearly the same. For that reason they proposed the use of delayed pulsed extraction, in which dissociation and ionization take place in field-free conditions and the extraction field is pulsed on after a time delay τ . The position of the ions with respect to the extractor grid are given with the following expressions:

$$d = d_0 - c\tau \quad (1.27)$$

$$d_f = d_0 - (c + u_0)\tau = d - u_0\tau \quad (1.28)$$

$$d_b = d_0 - (c - u_0)\tau = d + u_0\tau \quad (1.29)$$

where d_0 is the starting position of the ions ($\tau = 0$); d_f is the position of the forward-scattered ions ($\alpha = 0$) and d_b is the position of the backward-scattered ions ($\alpha = \pi$) after time delay τ , (the moment when the extraction field is pulsed on). In this case, the temporal spread of the ion cloud along the TOF axis becomes:

$$\Delta T = \left| T_f(s_f, v_f) - T_b(s_b, v_b) \right| \quad (1.30)$$

The ion trajectory simulations were also performed for the case of delayed extraction, and the results are presented in the Figure 1.19. The upper panel shows the spatial evolution of the ion cloud on its way to the detector when using a delay of 250 ns. From the evolution of the ion cloud we observe the initial increase in the width Δx during the delay time τ . After switching on the acceleration, Δx decreases, then the ions are focused a few centimeters after the extractor grid, and subsequently the ion cloud expands rapidly. The increase in the width Δx results in larger temporal spread of the ion packet. In Figure 1.19. (b) the temporal spread of the ion packet along the TOF axis is plotted as a function of velocity u_0 for various extraction delays τ .

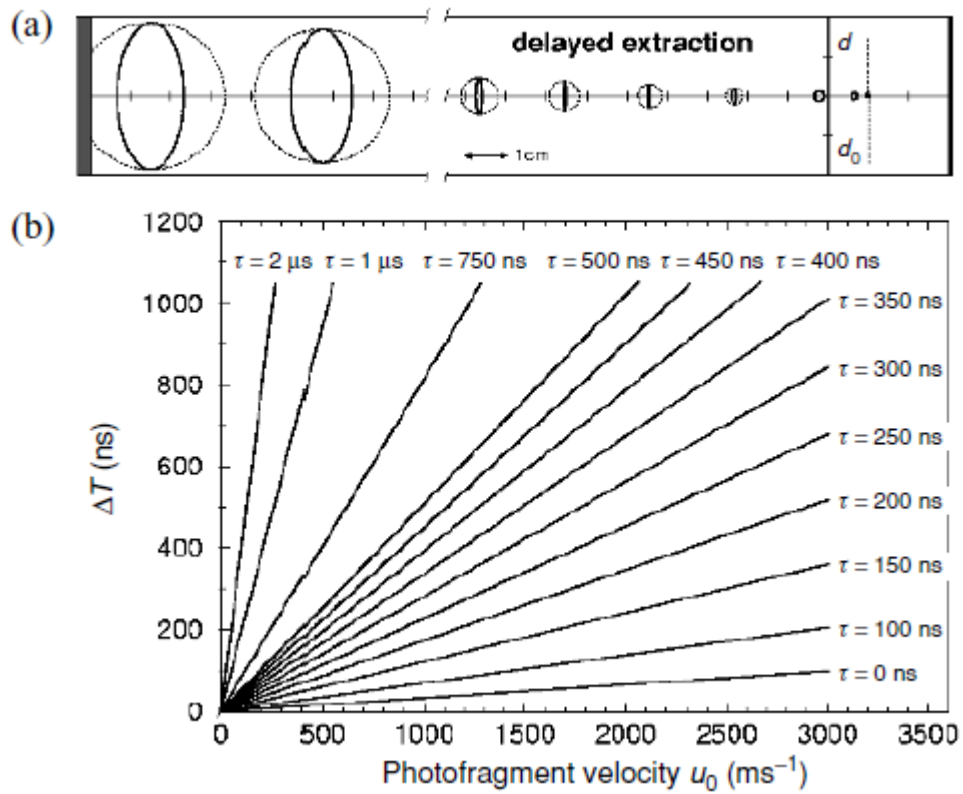


Fig. 1.19. (a) The upper panel depicts the spatial evolution of the ion cloud on its way to the detector for the case of a *delayed extraction* of the ion cloud ($\tau = 250$ ns). A space focus appears in the drift region after which the axial width of the ion cloud increases rapidly. (b) The lower panel shows the time width of the ion cloud at the detector as a function of the photofragment velocity u_0 ($c = 1000$ m/s). The different curves correspond to different delay times τ . ΔT increases almost linearly over a wide range of photofragment velocities as well as extraction delays. The dependency of ΔT on τ shows a minimum at zero delay times (DC extraction).

1.2.5 Collision-induced dissociation

In order to gain more deeper insight about the stability and the structure of the clusters one method is to supply them with an excess of energy leading to their fragmentation and to identify/analyze the fragmentation products. Usually, the energy deposition in the cluster occurs either by photon absorption in photofragmentation experiments or by collisional activation with a gas in collision-induced dissociation (CID) experiments.

In some mass-spectrometric investigations, collision-induced processes are considered a nuisance. For example, in the study of metastable dissociation significant effort is necessary to eliminate the influence of collision processes induced by the residual gas. However, the investigations by McLafferty,^{38,39,40,41} Jennings⁴² and Beynon^{43,44,45,46,47,48} have shown that collision-induced processes can in fact provide a wealth of valuable information about ions, for example about their structures, and the mechanisms of their formation and decomposition.

The technique of collision-induced dissociation (CID) has been proven to be a powerful tool for obtaining information about the stability, the bonding, and the structure of ionic species. Numerous groups have applied CID to investigate a wide variety of cluster systems (e.g. metal,⁴⁹ metal oxide,²³ carbon⁵⁰ and silicon⁵¹ clusters).

When cluster ions (AB^+), possessing a high translational kinetic energy (a few hundred of eV or even more) collide with neutral atoms or molecules (N), the main collisional processes are the following:



With the exception of elastic or inelastic scattering in all the other reaction channels, the ratio m/q of the initial cluster decreases, either by reducing m or by increasing q .¹⁷ These processes can be generally classified into two categories: (i) non-dissociative collisions, where the parent cluster ion does not break up as a consequence of the collision; and (ii) dissociative collisions, where the ion fragments before reaching the detector.

The first reaction (1.31) indicates elastic or inelastic scattering of a fast cluster ion with a steady (this is an approximation) neutral target atom (or molecule). In the first case, the total kinetic energy of the collision partners remains unchanged. In the case of inelastic scattering, part of the translational energy of the cluster ion is converted into internal energy of both the projectile and the target, which is denoted with the asterisk.

Charge transfer (1.32) represents a class of reactions where electrons are exchanged between the projectile and the target, which leads to charge exchange. This process becomes more important when the target gas has a low ionization potential (IP). For this reason, the most commonly used collision gas is helium since it has a very high IP, 24.5 eV.⁵² Scattering of the ion beam is also minimal, because of its small cross section, and the gas is inexpensive and fast to pump away. Charge stripping (1.33) is normally observed at collision energies of about 1 keV. As all of the latest three processes can only result from electronic excitation, this suggests that collision activation under these conditions leads at least in part to electronic excitation.

However, especially for larger molecules, the mechanisms of collisional activation are more likely to involve vibrational excitation. In this case, it may occur through impulsive collision of the target atom or molecule with a selected atom or group of atoms in the region of the collision site. If the ions have gained sufficient vibrational energy during the collision, this can subsequently lead to their dissociation. Thus, the process of CID, illustrated by the Equation 1.34, can be considered as consisting of two distinct consecutive events. In the first step, collisions between the projectile ions and the target gas lead to the formation of activated ions AB^{+*} (Equation 1.31). The second step is unimolecular decomposition of the activated ions:



The conservation of energy and of momentum imply that only a fraction of the translational energy is converted into internal energy under inelastic conditions. The maximum

amount of energy available for conversion to internal energy, is actually the kinetic energy in the centre of mass coordinate system, E_{cm} , given by the following equation:

$$E_{\text{cm}} = E_{\text{lab}} \frac{M_t}{M_i + M_t} \quad (1.37).$$

where M_i is the mass of the ion, M_t is the mass of the stationary target molecule, and E_{lab} the ion kinetic energy in the laboratory frame of reference. Consequently, an increase in the ion kinetic energy or in the target gas mass increases the energy available for the conversion. At low collision energies (low E_{cm}) and lower molecular mass ions, a relatively large fraction of this maximum is converted to internal energy. This fraction decreases with the increase in collision energy, and at high collision energies, that is in the range of kiloelectronvolts, the conversion to internal energy is relatively inefficient, so that the mean internal energy of ions activated in low and high energy collisions may be quite similar.

When a parent ion with mass m_p having initial kinetic energy E_{Lab} in the laboratory frame dissociates into a fragment with mass m_F , then – neglecting the center of mass kinetic energy release from dissociation, which is typically a few eVs – the laboratory kinetic energy of the fragment m_F is as follows:

$$E_F = (E_{\text{Lab}})(m_F / m_p) \quad (1.38).$$

According to the Equation 1.38 the fragmentation products possess lower kinetic energy. This relation can be used to separate fragments from the parents using detection devices sensitive to the kinetic energy of the incident ions. Such devices are reflectron and retarding field energy analyzer (RFEA), both used in our laboratory for CID experiments in two different arrangements: beam-gas cell and crossed molecular beams (see Section 2.2.1 and Ref. 17).

References

- ¹ M. Klessinger and J. Michl, *Excited States and Photo-Chemistry of Organic Molecules* (Wiley, New York, 1995).
- ² J. Hollas, *Modern Spectroscopy* (Wiley, New York, 2004).
- ³ J. Brown and A. Carrington, *Rotational Spectroscopy of Diatomic Molecules, Cambridge Molecular Science* (Cambridge University Press, Cambridge, 2003).
- ⁴ B. Wardle, *Principles and applications of photochemistry* (Wiley, Chichester, 2009).
- ⁵ R. Schinke, *Photodissociation Dynamics* (Cambridge University Press, Cambridge, 1993).
- ⁶ G. Herzberg, *Molecular Spectra and Molecular Structure, Vol. III. Electronic Spectra and Electronic Structure of Polyatomic Molecules* (Van Nostrand Reinhold, New York, 1966).
- ⁷ P. Jena, S.N. Khanna, and B.K. Rao, (eds) *Physics and Chemistry of Finite Systems: From Clusters to Crystals* (NATO ASI Series) (Kluwer Academic Publishers, Dordrecht, 1992).
- ⁸ H. Haberland, (ed.) *Clusters of Atoms and Molecules* (Springer Series in Chemical Physics) (Springer Verlag, Berlin Heidelberg, 1994).
- ⁹ M.A. Duncan, (ed.) *Advances in Metal and Semiconductor Clusters, Vol. I. Spectroscopy and Dynamics* (JAI Press, Greenwich, 1993).
- ¹⁰ M.A. Duncan, (ed.) *Advances in Metal and Semiconductor Clusters, Vol. II. Cluster Reactions* (JAI Press, Greenwich, 1994).
- ¹¹ M.A. Duncan, (ed.) *Advances in Metal and Semiconductor Clusters, Vol. III. Spectroscopy and Structure* (JAI Press, Greenwich, 1995).
- ¹² S.E. Kooi and A.W. Castleman, Jr., “Photofragmentation of vanadium oxide cations”, *J. Phys. Chem. A* **103**, 5671 (1999).
- ¹³ M. Velegarakis and A. Sfounis, “Formation and photodecomposition of cationic titanium oxide clusters”, *Appl. Phys. A* **97**, 765 (2009).
- ¹⁴ M. Jadraque, B. Sierra, A. Sfounis, and M. Velegarakis, “Photofragmentation of mass-selected titanium oxide cluster cations”, *Appl. Phys. B* **100**, 587 (2010).
- ¹⁵ M. Velegarakis, M. Massaouti, and M. Jadraque, “Collision-induced dissociation studies on gas-phase titanium oxide cluster cations”, *Appl. Phys. A* **108**, 127 (2012).

- ¹⁶ G. Mpourmpakis, M. Velegarakis, C. Miheasan, and A. N. Andriotis, “Symmetry-switching molecular $\text{Fe}(\text{O}_2)_n^+$ clusters”, *J. Phys. Chem. A* **115**, 7456 (2011).
- ¹⁷ M. Velegarakis, C. Miheasan, and M. Jadraque, “Collision-induced dissociation studies on $\text{Fe}(\text{O}_2)_n^+$ ($n = 1-6$) clusters: application of a new technique based on crossed molecular beams”, *J. Phys. Chem. A* **117**, 2891 (2013).
- ¹⁸ W. Demtroder, *Laser spectroscopy: Basic Concepts and Instrumentation* (Advanced texts in physics) (Springer Verlag, Berlin 2003).
- ¹⁹ K. Dreisewerd, M. Schürenberg, M. Karas, and F. Hillenkamp, “Influence of the laser intensity and spot size on the desorption of molecules and ions in matrix-assisted laser desorption/ionization with a uniform beam profile”, *Int. J. Mass Spectrom. Ion Proc.* **141**, 127 (1995).
- ²⁰ C. Lüder, D. Prekas, and M. Velegarakis, “Ion-size effects in the growth sequences of metal-ion-doped noble gas clusters”, *Laser Chem.* **17**, 109 (1997).
- ²¹ D. Prekas, C. Lüder, and M. Velegarakis, “Structural transitions in metal-ion-doped noble gas clusters: Experiments and molecular dynamics simulation”, *J. Chem. Phys.* **108**, 4450 (1998).
- ²² M. Velegarakis, “Stability, structure and optical properties of metal ion-doped noble gas clusters”, In *Advances in Metal and Semiconductor Clusters, Vol. V*, ed. M. A. Duncan (JAI Press, London, 2001) p. 227.
- ²³ H. T. Deng, K. P. Kerns, and A. W. Castleman, Jr., “Formation, structures, and reactivities of niobium oxide cluster ions”, *J. Phys. Chem.* **100**, 13386 (1996).
- ²⁴ A. Fielicke, G. Meijer, and G. von Helden, “Infrared spectroscopy of niobium oxide cluster cations in a molecular beam: identifying the clusters structures”, *J. Am. Chem. Soc.* **125**, 3659 (2003).
- ²⁵ K. S. Molek, T. D. Jaeger, and M. A. Duncan, “Photodissociation of vanadium, niobium and tantalum oxide cluster cations”, *J. Chem. Phys.* **123**, 144313/1 (2005).
- ²⁶ K. Athanassenas, D. Kreisle, B.A. Collings, D.M. Rayner, and P.A. Hackett, “Ionization potentials of niobium oxide clusters”, *Chem. Phys. Lett.* **213**, 105 (1993).
- ²⁷ W. C. Wiley and I. H. McLaren, “Time-of-flight mass spectrometer with improved resolution”, *Rev. Sci. Instrum.* **26**(12), 1150 (1955).
- ²⁸ A. Ellis, M. Feher, and T. Wright, *Electronic and Photoelectron Spectroscopy:*

Fundamentals and Case Studies (Cambridge University Press, Cambridge, 2005).

²⁹ D. W. Chandler and P. L. Houston, “Two-dimensional imaging of state-selected photodissociation products detected by multiphoton ionization”, *J. Chem. Phys.* **87**(2), 1445 (1987).

³⁰ A. T. J. B. Eppink and D. H. Parker, “Velocity map imaging of ions and electrons using electrostatic lenses: Application in photoelectron and photofragment ion imaging of molecular oxygen”, *Rev. Sci. Instrum.* **68**, 3477 (1997).

³¹ B. Whitaker, *Imaging in Molecular Dynamics: Technology and Applications* (Cambridge University Press, Cambridge, 2003).

³² M. N. R. Ashfold, N. H. Nahler, A. J. Orr-Ewing, O. P. J. Vieuxmaire, R. L. Toomes, T. N. Kitsopoulos, I. A. Garcia, D. A. Chestakov, S.-M. Wu, and D. H. Parker, “Imaging the dynamics of gas phase reactions”, *Phys. Chem. Chem. Phys.* **8**, 26 (2006).

³³ A. J. R. Heck and D. W. Chandler, “Imaging techniques for the study of chemical reaction dynamics”, *Annu. Rev. Phys. Chem.* **46**, 335 (1995).

³⁴ B. J. Whitaker, “Photo-ion imaging techniques and future directions in reactive scattering”, In *Research in Chemical Kinetics, Vol. I*, eds. R. G. Compton, G. Hancock (Elsevier, Amsterdam, 1993) p. 307.

³⁵ C. R. Gebhardt, T. P. Rakitzis, P. C. Samartzis, V. Ladopoulos, and T. N. Kitsopoulos, “A new approach to ion imaging and velocity mapping”, *Rev. Sci. Instrum.* **72**, 3848 (2001).

³⁶ V. Papadakis and T. N. Kitsopoulos, “Slice imaging and velocity mapping using a single field”, *Rev. Sci. Instrum.* **77**, 083101 (2006).

³⁷ www.simion.com

³⁸ W. F. Haddon and F. W. McLafferty, “Metastable ion characteristics. VII. Collision-induced metastables”, *J. Am. Chem. Soc.* **90**, 4745 (1968).

³⁹ W. F. Haddon and F. W. McLafferty, *Anal. Chem.* **41**, 31 (1969).

⁴⁰ F. W. McLafferty, P. F. Bente III, R. Kornfeld, S.-C. Tsai, and I. Howe., *J. Am. Chem. Soc.* **95**, 2120 (1973).

⁴¹ F. W. McLafferty, R. Kornfeld, W. F. Haddon, K. Levsen, I. Sakai, P. F. Bente III, S.-C. Tsai, and H. D. R. Schuddemage, “Application of collisional activation spectra to elucidation of organic ion structures”, *J. Am. Chem. Soc.* **95**, 3886 (1973).

- ⁴² K. R. Jennings, "Collision-induced decompositions of aromatic molecular ions", *Int. J. Mass Spectrom. Ion Phys.* **1**, 227 (1968).
- ⁴³ J. H. Beynon, R. M. Caprioli, and T. Ast, "A simple modification of mass spectrometer for the study of collision-induced fragmentations", *Int. J. Mass Spectrom. Ion Phys.* **7**, 88 (1971).
- ⁴⁴ R. G. Cooks, J. H. Beynon, and T. Ast, "Stripping reactions of gaseous ions in the mass spectrometer", *J. Am. Chem. Soc.* **94**, 1004 (1972).
- ⁴⁵ T. Ast, J. H. Beynon, and R. G. Cooks, "Long-lived states of rare gas ions. An ion kinetic energy study", *J. Am. Chem. Soc.* **94**, 6611 (1972).
- ⁴⁶ J. H. Beynon, R. M. Caprioli, W. E. Baitinger, and J. W. Amy, "The ion kinetic energy spectra of some aromatic hydrocarbons", *Org. Mass Spectrom.* **3**, 455 (1970).
- ⁴⁷ J. H. Beynon, A. Mathias, and A. E. Williams, "Doubly charged ion mass spectra of some simple aromatic compounds", *Org. Mass Spectrom.* **5**, 303 (1971).
- ⁴⁸ T. Keough, J. H. Beynon, and R. G. Cooks, "-E Mass spectra", *J. Am. Chem. Soc.* **95**, 1695 (1973).
- ⁴⁹ W. Begemann, S. Dreihöfer, K. H. Meiwes-Broer, and H. O. Lutz, "Sputtered metal cluster ions: Unimolecular decomposition and collision induced fragmentation", *Z. Phys. D* **3**, 183 (1986).
- ⁵⁰ G. von Helden, M.T. Hsu, N. Gotts, and M.T. Bowers, "Carbon cluster cations with up to 84 atoms: structures, formation mechanism, and reactivity", *J. Phys. Chem.* **97**, 8182 (1993).
- ⁵¹ M.F. Jarrold, "Drift Tube Studies of Atomic Clusters", *J. Phys. Chem.* **99**, 11 (1995).
- ⁵² H.M. Rosenstock, K. Draxl, B.W. Steiner and J.T. Herron, "Energetics of gaseous ions", *J. Phys. Chem. Ref. Data* **6**, supplement 1, 1 (1977).

Chapter II

Experimental Apparatus and Methods

The experiments described in this thesis relate to photodissociation studies of ICl and collision-induced dissociation studies of transition metal oxide clusters – yttrium and niobium. The photodissociation studies presented in Chapter III and IV were performed using slice imaging apparatus “DIAMANTE” in the Laboratory for Molecular Dynamics of the Institute for Electronic Structures and Lasers (IESL). The cluster studies presented in Chapter V and VI were performed in the Laboratory for Cluster Dynamics of the IESL using cluster apparatus “ARIADNE”.

2.1. The slice imaging experimental apparatus

A schematic of the photofragment imaging spectrometer used in this study is presented in Figure 2.1. The apparatus consists of two differentially pumped regions:

- (A) a source chamber (Region A in Figure 2.1), and
- (B) a detector chamber (Region B in Figure 2.1).

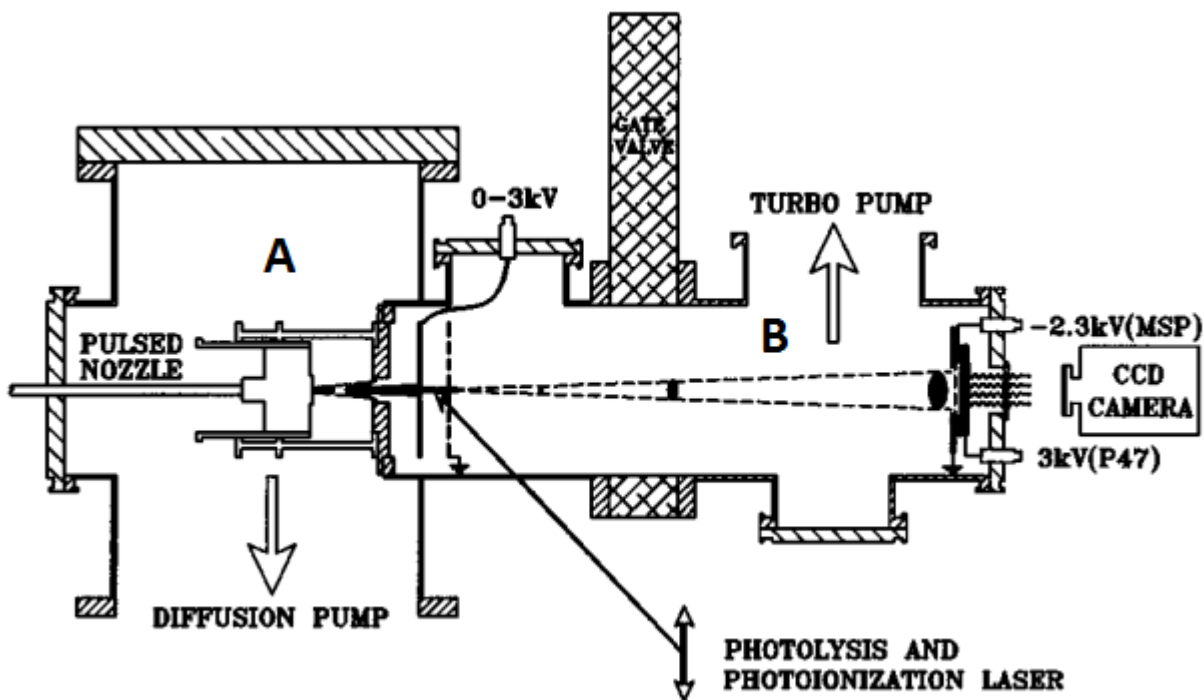


Figure 2.1. Schematic view of the slice imaging apparatus.

The source chamber is pumped by a baffled 3000 l/s oil diffusion pump (Leybold, DI 3000) that is backed by a Leybold Trivac D65B rotary mechanical pump at a speed of 65 m³/h. This chamber is fitted with a home-built piezoelectrically actuated nozzle valve (1 mm diameter) operating at 10 Hz, which provides the molecular beam. The basic valve design is based on original work of Trickl-Proch¹ with a modification similar to work of Liu and co-workers² and similarly Wodtke and co-workers.³

The detector chamber is pumped by a 600 l/s turbo-molecular pump (Leybold, Turbovac 600) that is backed by a Leybold Trivac D25B rotary pump at a speed of 25 m³/h. The chamber is equipped with an ion optics assembly. A schematic of the new ion optics design⁴ used in our slice imaging experiments is shown in Figure 2.2.

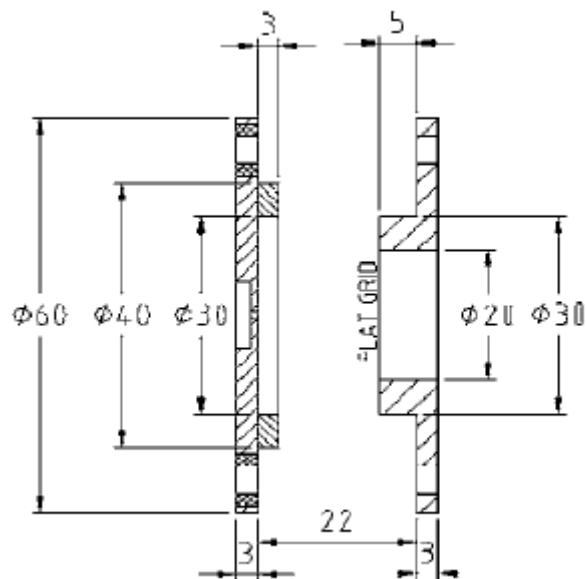


Figure 2.2. Scaled schematic of the ion optics (drawing units in mm).

The optics consist of two electrodes: a repeller electrode, that also serves to collimate the molecular beam and the extractor, and a grounded extractor (flat grid). A small step on both the repeller and extractor electrodes were introduced in order to achieve velocity mapping conditions. The lens operating voltage is not as critical as in the case of the conventional velocity mapping geometry described in the pioneering paper of Eppink and Parker.⁵

A supersonic molecular beam is formed by supersonic expansion into the source vacuum chamber via the nozzle valve. A stagnation pressure of $P_0 \leq 1$ bar and a nozzle diameter of 1 mm are used in order to minimize cluster formation during the expansion. Approximately 5 cm from the nozzle orifice the expansion is skimmed using a $\phi 1.5$ mm skimmer (Beam Dynamics), which also serves as means of differentially pumping the two regions of the apparatus, before it enters the detection chamber where the ion optics is positioned. After passing through the ~ 2 mm diameter hole in the repeller electrode, the molecular beam is intersected at right angle by the photolysis/photofragment ionization (probe) laser at the geometric focus position of a single-electrode repeller-grid arrangement.

The photodissociation dynamics experiments reported in this thesis were conducted using one or two color schemes. The laser light was generated by two tunable lasers firing at 10 Hz: (1) a Nd^{3+} :YAG (BMI series 5000) pumping a master oscillator-power oscillator system (MOPO

Spectra Physics 730DT10), and (2) an excimer-pumped (Lambda Physik LPX, operating with XeCl) pulsed-dye laser (LPD3000) using the appropriate dye.

In a two-color experiment, two counter-propagating laser beams, a photolysis and a probe, are focused onto the collimated molecular beam using 30 cm lenses. The interaction region is located midway between the repeller and extractor electrodes. The photolysis laser is used to generate neutral fragments. After a suitable time delay the probe laser is used to state specifically ionize one of these fragments via resonant enhanced multiphoton ionization (REMPI). Here, the probe pulse is delayed with respect to the photolysis pulse, in order to allow a sufficient density of photofragments to build up prior to the REMPI detection. Moreover, the time delay between photolysis and photoionization is carefully monitored in order to avoid photofragment “fly-out” affecting the accuracy of branching ratio measurements, while at the same time avoiding zero delay between the lasers to minimize multiphoton processes. Typically the delay is set at ~ 10 ns, with the photolysis preceding the ionization. In a one-color experiment, the photolysis laser pulse is also used for the REMPI of the nascent photofragments. The laser power is maintained at about 3–5 mJ/pulse in order to minimize space-charge effects from excessive ion production in the interaction region.

The velocity distribution of the photofragments produces a Doppler energy shift in the resonant transition used for their REMPI which is larger than the probe-laser bandwidth. In order to ensure that all photofragment velocities are detected with equal probability, it is necessary to scan the laser over the Doppler width of the resonant transition.

For the slicing experiments, the repeller is pulsed ON at the appropriate time delay (a few hundreds of ns) following the photolysis and ionization. The ions produced are then accelerated by the ion optics along the axis of the machine towards a position sensitive detector located approximately 45 cm from the interaction region. Ions of different masses are separated by time-of-flight (TOF) during their field-free trajectory on route to the detector. The detector consists of a dual, imaging-quality MCP array coupled to a phosphor screen and has an effective diameter of 40 mm. After passing through the TOF region they hit the surface of the front MCP. For each ion detected, the MCPs produce a large amount of electrons at the rear side. These electrons are accelerated onto the phosphor screen and create a spot of phosphorescence. Discrimination between the ions of interest and the undesired background ions is achieved by

“gating” the detector through the application of a high-voltage pulse to the anode. The timing of the experiment is controlled using a pulse generator (DG535 by Stanford Research Systems) and is optimized by monitoring the ion signal which appears on a 150 MHz oscilloscope (Hameg HM1507). During the “gated” operation, signal monitoring is stopped as the high voltage pulse applied to the anode will capacitively couple to the monitoring oscilloscope.

The image frame is recorded asynchronously every second (~10 laser shots) by a CCD camera and several thousand frames are averaged to form images. Each final image is appropriately integrated from its center over angle to obtain the speed distribution, and over radius to extract the angular distribution of the fragments. Background images are obtained either by tuning the photoionizing laser off-resonance or changing the timing of the laser pulse so that it arrives at the interaction region long after the molecular beam pulse has crossed this region (so that it probes the background), and these images are subtracted from the signal images.

2.1.2 Data analysis

The radial position ρ of the photofragments is related to its speed u via the relationship

$$\rho = ut \tag{2.1}$$

where t is the flight time of the photofragment from the interaction region to the detector. Time t is essentially a constant for all concentric ion clouds, as the laboratory velocity (extraction energy 0.5 – 3.0 keV) is much greater than the center-of-mass velocity of the photofragments (typically 0.5 – 3 eV).

The energy of the fragments E is proportional to the radius of the recorded images r , which is measured in pixels. Equation 2.1 is the relation connecting these two quantities.

$$E = kr^2 \tag{2.2}$$

In this equation k is the proportionality constant, the calibration factor, with energy units that is dependent on the experiment parameters such as repeller voltage and the spatial position of the photolysis laser. The calibration factor k can be determined experimentally using a well-studied photodissociation process. The system of choice should have an accurately known dissociation

energy D_0 and the produced fragments should have known internal energy E_{int} . For this process the total kinetic energy release (TKER) is expressed in the following way

$$\text{TKER} = E_0 + E_{\text{phot}} - D_0 - E_{\text{int}} \quad (2.3)$$

where E_0 is the initial internal energy of the molecule, which in a molecular beam experiment is generally assumed to be zero, and E_{phot} is the photon energy. From the kinetic energy of the calibrant fragment, the calibration factor can be derived. The velocity distributions derived from the images are converted to KER distributions. Each final image is appropriately integrated from its center over angle to obtain the speed distribution, and over radius to extract the angular distribution of the fragments.

2.2 The cluster experimental apparatus

The cluster experimental apparatus consists of a laser vaporization (LaVa) source coupled to a collinear time-of-flight (TOF) mass spectrometer.⁶ The principles of LaVa source are described Section 1.2.5, while the principles of TOF mass spectrometer are given in Section 1.2.1.2. The experimental apparatus in operation in our laboratory is shown in Figure 2.3. In this figure only general construction is shown, while the two modifications will be presented later (Section 2.2.1). The apparatus is separated into three successive, differentially pumped vacuum chambers:

1. a source (main) chamber,
2. a separately pumped chamber with the acceleration and a field-free time-of-flight region,
3. and a detection (scattering) chamber.

The LaVa source is situated in the first, source chamber. The source chamber is pumped using diffusion pump (Leybold DI 3000 with a pumping speed of 3000 L/s) that is backed, first by a Roots vacuum pump (Leybold – RUVAC WA 251 with a pumping speed of 253 m³/h) and then by a Leybold Trivac D16B rotary mechanical pump at a speed of 16 m³/h. The operating pressure in the source region is $\sim 10^{-4}$ mbar.

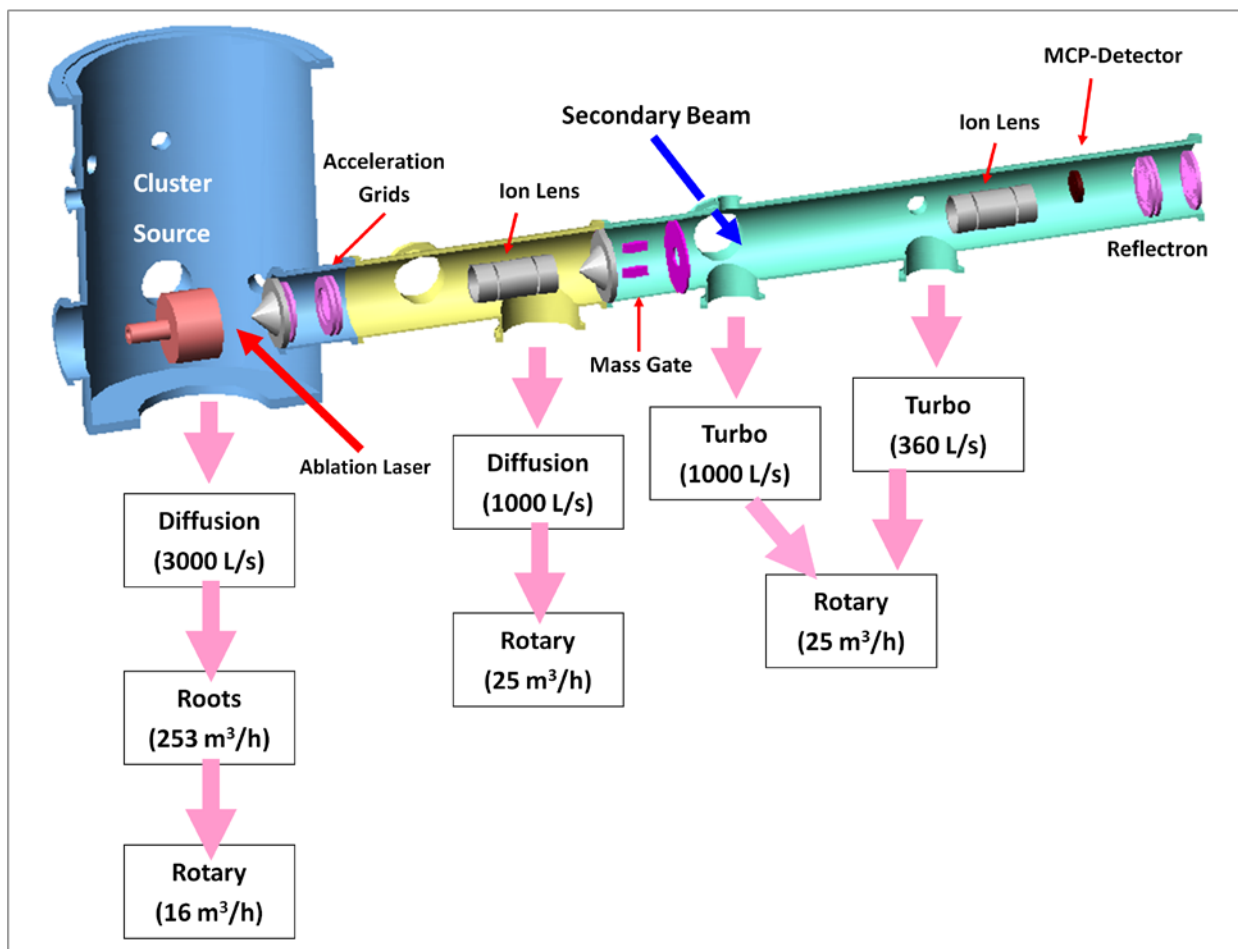


Figure 2.3. Schematic view of the molecular beam apparatus utilized to perform the CID experiments.

The acceleration region is separated from the source chamber with a 4 mm diameter conical skimmer. This region contains double-field (250 V/cm, 925 V/cm) pulsed acceleration electrodes for the TOF analysis of the produced cluster ions. Therefore, the acceleration takes place in two stages resulting in spatially focused cluster ions. The first field which is formed by two parallel flat grids, 8 cm apart, is located about 14 cm from the formation region. The relatively long field length allows us to accelerate the entire ion packet (typically 1–7 cm long) produced from the source. The acceleration region is pumped by a Leybold Heraeus DI 1000/2B diffusion pump (1000 L/s), which is backed by a Leybold Trivac D25B rotary pump (25 m³/h). The operating pressure inside the second chamber is $\sim 10^{-6}$ mbar.

The detection chamber, is pumped by two turbo pumps: Leybold Turbovac 1000 C (1000 L/s) and a smaller Leybold Turbovac 360 CSV (360 L/s) in parallel, and this allows for a

background pressure of $\sim 10^{-6}$ mbar under operating conditions, using the same backing, Leybold Trivac D25B rotary pump (25 m³/h).

Cluster ions are generated in the source (main) chamber using an open LaVa source (Fig. 1.13), without a growth channel. The cluster ions are formed by mixing the plasma plume, produced by the laser ablation of a rod of high purity metal, with a supersonic expansion of molecular oxygen. The metal rod is placed just in front of the nozzle orifice and irradiated by fundamental beam (1064 nm) or a higher harmonic (first harmonic at 532 nm, second harmonic at 355 nm or the fourth harmonic at 266 nm) of a homebuilt Q-switched Nd:YAG laser (pulse width 10 ns, repetition rate 10 Hz). The laser beam is focused on the target surface to a spot area ≤ 1 mm² using a lens with a 50 cm focal length. The rod is continuously rotating to ensure the laser is always ablating a fresh metal surface. The ablation plasma plume is crossed perpendicularly a few millimeters above the target surface with the pulsed O₂ molecular jet produced by a homemade pulsed nozzle (diameter 0.5 mm, $t_{\text{pulse}}=200$ μs). The valve is operating at room temperature and with a backing pressure of ~ 5 bar. The mixing takes place about 2–4 mm downstream from the nozzle orifice. The delay between the initial gas pulse and the laser pulse is approximately 1 μs during operation, and can be optimized in order to produce more clusters.

The vibrationally cold cationic clusters in the form of a supersonic jet flow are guided through the skimmer out of the source chamber, and the resulting pulsed molecular beam enters the acceleration region. A fast-switching high voltage circuit provides a variable voltage pulse V_{acc} (typically 1500 V), that starts the acceleration of the cluster ions existing in the cluster beam and constitutes the time origin for the TOF spectrum. The accelerated cluster ions possess laboratory-frame kinetic energy $E_{\text{Lab}}=q \cdot e \cdot V_{\text{acc}}$ (e is the electron charge and q the charge state of a given ion). Traversing a field-free region, the ions are separated according to their mass/charge (m/q) ratio and detected at different times, either directly in a linear arrangement, or after reflection from the reflectron assembly. The apparatus is equipped with two microchannel plate (MCP) detectors, and the TOF spectra are acquired with a 150 MHz computer-controlled digital oscilloscope (LeCroy 9410). The final TOF spectrum is obtained by averaging over 100–200 laser shots, and is transferred through a GPIB interface from the digital oscilloscope to a PC and

further processed using software developed in our laboratory. To synchronize the timing between the several pulsed components, coupled delay generators are used.

2.2.1 Conventional and crossed beams method

Two different CID methods have been applied to measure fragmentation cross sections of positively charged metal oxide clusters. The first one is the standard CID technique, where mass-selected clusters collide with noble gas atoms in a collision cell. The second experimental approach is based on crossed molecular beams. For the sake of comparison, both the conventional and the new setup are presented in Figure 2.4.

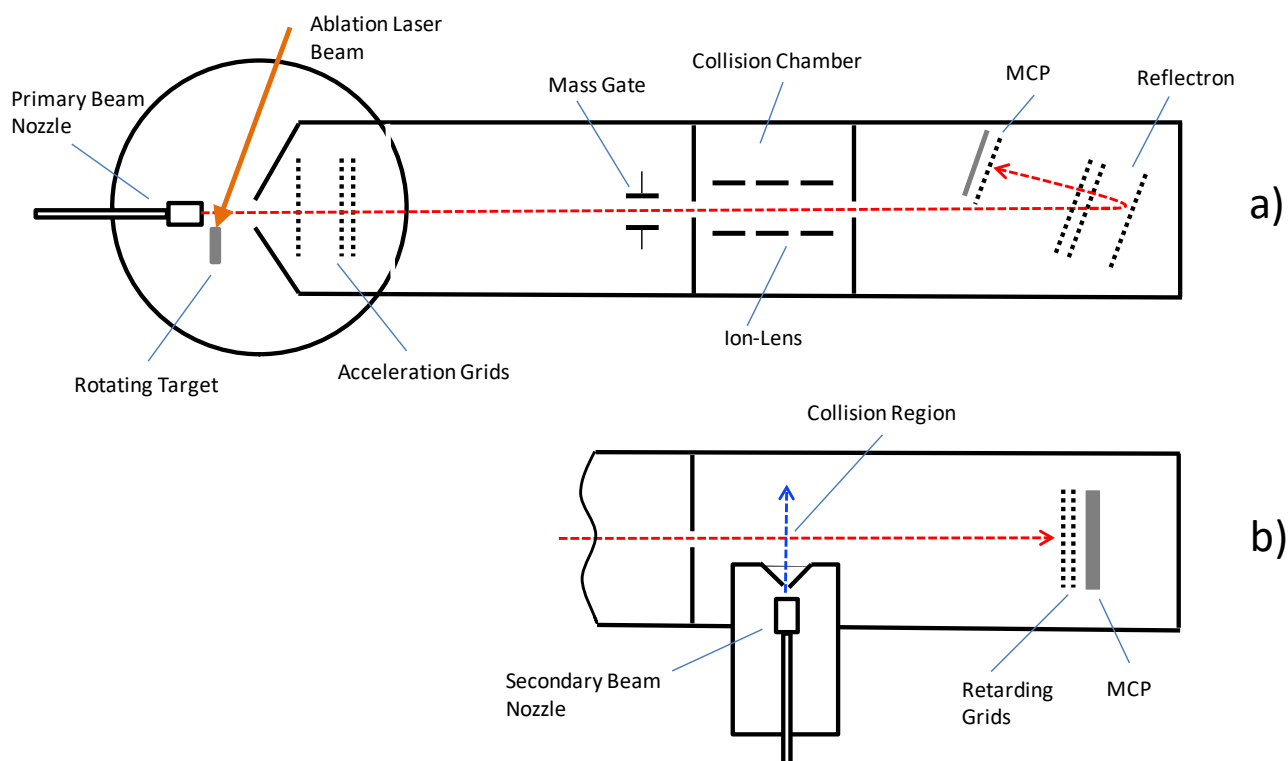


Figure 2.4. Schematic diagram of the experimental arrangement indicating the two different configurations used to measure fragmentation cross sections by: (a) “conventional” CID method with mass selection and reflectron detector and (b) crossed molecular beams arrangement with a retarding potential analyzer. (from Ref. 7)

Beam-Gas Cell Configuration – In the first case, presented in Figure 2.4(a), we have used the well established CID technique, which has been widely used concerning fragmentation of several cluster systems.^{8,9} This method has been applied to small gas-phase titanium oxide clusters (Ti_xO_y^+) in our laboratory, and the experimental details and results are described in a previous paper by our group.¹⁰ In this conventional experimental setup, after acceleration step the cluster ions are mass-selected in order to study their individual properties. The mass selection is performed by a two-plate pulsed capacitor placed at the spatial focus (~ 1 m) of the Wiley-McLaren unit. A beam of mass-selected parent cluster ions passes through a 27-cm-long collision chamber filled with krypton (Kr) gas at a pressure of 6×10^{-4} mbar, where certain fraction undergoes fragmentation. Following fragmentation, the initially selected parent ion and all its possible fragment ions are separated with a reflectron setup.¹¹ The ions are here detected with an MCP detector after reflection from the reflectron. The mass-selected parent cluster and its fragments are recorded as different peaks in the same TOF mass spectrum.

This well established “conventional” CID method, is relatively simple but is time-consuming when measuring a series of clusters, due to the necessity of mass selection. It requires long-term stability of the cluster beam and also special care has to be paid to avoid signal losses because of the different focusing conditions for each particular cluster, different fragment’s flight paths through the reflectron, etc.

Crossed Molecular Beams – In the new crossed beam experimental setup, shown in Figure 2.4(b), that we introduced recently^{7,11}, no mass selection is needed. The technique utilizes a secondary beam of Ne atoms and a detector equipped with a retarding field energy analyzer (RFEA). Here the collision chamber is removed, and the primary cluster beam containing the entire distribution of cluster cations crosses perpendicularly, in the field-free zone of the mass spectrometer, the pulsed secondary Ne beam with pulse duration of 700 μs . The secondary beam is formed in a separated chamber by expansion through a nozzle similar to the primary beam nozzle (0.2 mm diameter, 3.5 bar backing pressure). The background pressure in the chamber with the secondary beam nozzle is maintained at $\sim 10^{-4}$ mbar by a 360 L/s turbo pump during the operation. This turbo pump is backed by a mechanical pump.

The secondary beam is skimmed with a 1 mm skimmer before entering into the main TOF-tube and interaction with the cluster beam. The volume of the interaction region of the two beams is $\sim 1 \times 1 \times 1 \text{ mm}^3$. In this assembly the MCP detector is situated along the ion beam at the end of the TOF tube, and the detection is performed directly in a linear arrangement. The RFEA consisting of two grids is inserted in front of the MCP detector and is used to selectively filter ions. The first grid is grounded, while the second one (closer to the MCP) is at a variable retarding potential (V_{grid}) and repels all ions possessing kinetic energy lower than $z \cdot e \cdot V_{\text{grid}}$.

Beam crossing experiments can be performed only by proper temporal overlapping of the two beams (configuration noted “beam on”). By introducing a 1-ms time delay, the beam crossing is avoided (“beam off”), while the background pressure is unchanged. This allows the discrimination of processes due to beam scattering from the (possible) background or metastable fragmentation. The fragmentation products have almost the same velocity as the parent, and they are detected as part of the same TOF peak but possess lower kinetic energy (Eq. 1.39) and therefore can be rejected by the RFEA, reducing the intensity of the peak. The RFEA has an energy resolution of about 5 %.

It is a significantly faster and more efficient method for obtaining fragmentation cross sections, without mass selection of the individual clusters. Furthermore, this method can provide information on additional reaction channels (besides fragmentation) activated by cluster ion-atom energetic collisions (such as multi-ionization or Coulomb explosion).

2.2.2 Fragmentation cross sections measurements

Assuming single collision conditions for our experiments, the fragmentation cross section Q can be determined from the equation:

$$Q = -\frac{1}{NL} \ln\left(\frac{I}{I_0}\right), \quad (2.4),$$

where I and I_0 are the transmitted intensities of the ion beam with and without the presence of the secondary beam, respectively, N is the number density of the target gas, and L is the length of

the beams crossing area. By measuring I and I_0 and considering that N and L are the same for all clusters, the relative fragmentation cross section for the cluster series can be determined.

In the case of beam-gas cell configuration, fragment ions, with lower kinetic energy than the parent, are recorded as different peaks in the reflectron TOF spectrum before the parent ion peak. The fragmentation cross section Q is determined from the parent intensity I_p , corresponding to parent peak in the TOF spectrum and the intensity $\sum I_F$ of all the fragment peaks using the relationship

$$Q = -\frac{1}{NL} \ln \left(\frac{I_p}{I_p + \sum I_F} \right) \quad (2.5),$$

where N is the number density of the target Kr-gas, and L is the length of the collision cell. These parameters (N and L) cannot be accurately measured¹ in the present experimental arrangement but are common for all the clusters investigated and therefore are not necessary for the comparison of different clusters measured under the same conditions.

In the case of crossed molecular beams, entire mass spectra are recorded at varying voltages applied on the RFEA grid (V_{grid}), in the range from 0 V to a value significantly higher than the accelerating voltage (V_{acc}). From such spectra, the intensity of each cluster can be measured and Figure 2.5 displays the expected evolution of one particular cluster's intensity as a function of RFEA potential, in the simplest case of a cluster having only one fragmentation channel ($AB^+ \rightarrow A^+ + B$). The solid line shows the intensity in the "beam off" configuration, and the dashed line displays the intensity expected in "beam on" configuration.

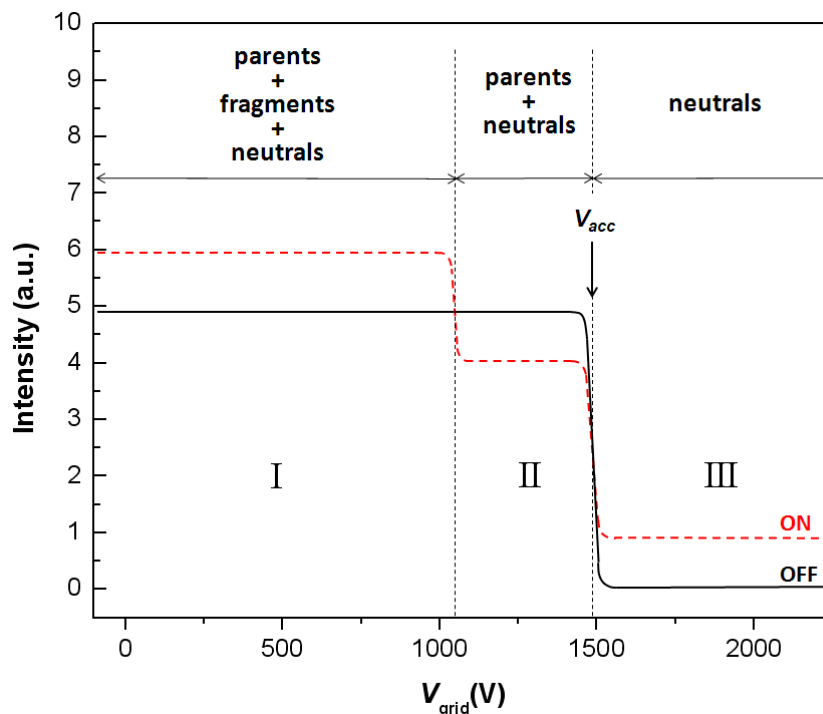


Figure 2.5. Intensity of “beam off” (solid line) and “beam on” (dashed line) signal as a function of grid voltage in the simplest case of an ion with only one fragmentation channel.

In the case of collisions (“beam on”), as the V_{grid} increases, attenuation of the cluster’s intensity is observed, due to rejection of fragment ions. This happens because fragmentation of a parent ion m_p accelerated to laboratory kinetic energy E_{Lab} will lead to a fragment m_F possessing kinetic energy E_F , which is a fraction of the parent’s kinetic energy (see Equation 1.39). The step-like decrease in the signal at a certain value of V_{grid} indicates the rejection of fragment ions with kinetic energy $E_F = q \cdot e \cdot V_{\text{grid}}$. As the laboratory velocity of the fragments is not expected to vary significantly, and considering all ions singly charged, their molecular masses can be determined from Equation 1.39, hence identifying the fragmentation mechanisms of the parent ions.

At low values of the RFEA voltage ($V_{\text{grid}} \approx 0$), initially formed clusters and newly formed fragments (ions and neutrals) will have the same TOF and contribute to the same peak, whose intensity represents the total signal⁷ (region I in Figure 2.5). Like the ions, fast neutrals impacting a MCP detector produce secondary electrons which result in a measurable signal. In this process,

the absolute detection efficiency for both ions and neutrals is similar.¹³ The neutrals' energy is given by the initial acceleration voltage, and it is not changed under the influence of the RFEA; therefore, the neutrals' contribution to the total MCP signal is constant and independent of the RFEA voltage. The signal is higher in “beam on” configuration than for “beam off” for every cluster in region I. The difference between the two signals corresponds to fragments (supplementary ions or neutrals formed from the parents).

Considering all the possible outcomes of cluster ion-atom collisions (Equations 1.31–1.36), this increase can be attributed to energetic neutral fragments (Equations 1.32 and 1.35) and/or to the creation of additional charged species by ionization (Equation 1.33) and Coulomb explosion (Equation 1.36).

At a RFEA voltage higher than the ionic fragments' kinetic energy but slightly lower than the acceleration voltage ($E_F < V_{\text{grid}} \lesssim V_{\text{acc}}$), all fragment ions are rejected and the measured intensity includes contributions from nonfragmented parents plus neutrals (region II). In this region, due to the rejection of ionic fragments, the “beam on” signal is lower than “beam off” signal. Finally, at V_{grid} significantly higher than the accelerating voltage ($V_{\text{grid}} \gg V_{\text{acc}}$) all charged species are rejected and only neutral species can reach the detector (region III).

Referring to Figure 2.5 and Equation 2.4, the fragmentation cross section for each particular cluster can be obtained by simply recording TOF spectra corresponding to regions II and III in Figure 2.5, and measuring the intensity of each cluster. The fragmentation cross section is given by the Equation 2.6:

$$Q = -\frac{1}{NL} \ln \left(\frac{I_{\text{II}}^{\text{ON}} - I_{\text{III}}^{\text{ON}}}{I_{\text{II}}^{\text{OFF}} - I_{\text{III}}^{\text{OFF}}} \right), \quad (2.6),$$

where $I_{\text{II}}^{\text{ON}}$ and $I_{\text{III}}^{\text{ON}}$ are signal intensities in “beam on” configuration in region II and III and $I_{\text{II}}^{\text{OFF}}$ and $I_{\text{III}}^{\text{OFF}}$ are “beam off” signal intensities in region II and III respectively (see Figure 2.5). $I_{\text{III}}^{\text{OFF}}$ is measured in order to take into account the possible metastable and background induced fragmentation. In our case, however, the amount of fragmentation in the “beam off” case is negligible.

References

- ¹ D. Proch and T. Trickl, “A high-intensity multi-purpose piezoelectric pulsed molecular beam source”, *Rev. Sci. Instrum.* **60**, 713 (1989).
- ² F. Dong, S.-H. Lee, and K. Liu, “F. Dong, S.-H. Lee, and K. Liu. Reactive excitation functions for $F + p\text{-H}_2 / n\text{-H}_2 / D_2$ and the vibrational branching for $F + HD$ ”, *J. Chem. Phys.* **113**, 3633 (2000).
- ³ Q. Ran, D. Matsiev, D. J. Auerbach, and A. M. Wodtke, “An advanced molecule-surface scattering instrument for study of vibrational energy transfer in gas-solid collisions”, *Rev. Sci. Instrum.* **78**, 104104 (2007).
- ⁴ V. Papadakis and T. N. Kitsopoulos, “Slice imaging and velocity mapping using a single field”, *Rev. Sci. Instrum.* **77**, 083101 (2006).
- ⁵ A. T. J. B. Eppink and D. H. Parker, “Velocity map imaging of ions and electrons using electrostatic lenses: Application in photoelectron and photofragment ion imaging of molecular oxygen”, *Rev. Sci. Instrum.* **68**, 3477 (1997).
- ⁶ W. C. Wiley and I. H. McLaren, “Time-of-flight mass spectrometer with improved resolution”, *Rev. Sci. Instrum.* **26**(12), 1150 (1955).
- ⁷ M. Velegarakis, C. Mihasan, and M. Jadraque, “Collision-induced dissociation studies on $Fe(O_2)_n^+$ ($n = 1\text{--}6$) clusters: application of a new technique based on crossed molecular beams”, *J. Phys. Chem. A* **117**, 2891 (2013).
- ⁸ H. T. Deng, K. P. Kerns, and A. W. Castleman, Jr., “Formation, structures, and reactivities of niobium oxide cluster ions”, *J. Phys. Chem.* **100**, 13386 (1996).
- ⁹ W. Begemann, S. Dreihöfer, K. H. Meiwes-Broer, and H. O. Lutz, “Sputtered metal cluster ions: Unimolecular decomposition and collision induced fragmentation”, *Z. Phys. D Atom. Mol. Cl.* **3**, 183 (1986).
- ¹⁰ M. Velegarakis, M. Massaouti, and M. Jadraque, “Collision-induced dissociation studies on gas-phase titanium oxide cluster cations”, *Appl. Phys. A: Mater. Sci. Process* **108**, 127 (2012).
- ¹¹ G. Mpourmpakis, M. Velegarakis, C. Mihasan, and A. N. Andriotis, “Symmetry-switching molecular $Fe(O_2)_n^+$ clusters”, *J. Phys. Chem. A* **115**, 7456 (2011).

¹¹ B.A. Mamyrin, “Laser assisted reflectron time-of-flight mass spectrometry”, *Int. J. Mass Spectrom. Ion Proc.* **131**, 1 (1994).

¹² J. J. H. van den Biesen, “Elastic Scattering I: Integral Cross Sections”, In *Atomic and Molecular Beam Methods, Vol. I*, ed. G. Scoles, (Oxford University Press, New York, 1988) p 472.

¹³ M. Barat, J. C. Brenot, J. A. Fayeton, and Y. J. Picard, “Absolute detection efficiency of a microchannel plate detector for neutral atoms”, *Rev. Sci. Instrum.* **71**, 2050 (2000).

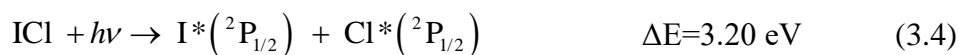
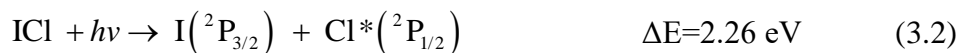
Chapter III

Ultraviolet photodissociation of iodine monochloride (ICl) at 235, 250, and 265 nm

3.1. Introduction

Well-characterized sources of spin-orbit excited atoms are necessary in order to study their relative chemical reactivity as compared to their ground state counterparts. Halogen atoms possess a wide range of spin-orbit coupling energies making them suitable candidates for such studies. Heteroatomic dihalogens such as ICl, BrCl, and IBr not only have very interesting photochemistry, worth studying on its own, but are premium photolytic sources for generation of excited state hot atoms.

In the case of ICl, the absorption exhibits two broad bands peaking at 270 nm and 470 nm, respectively.¹ A number of potential energy surfaces contribute to this absorption.^{2,3,4} Following the labeling of Yabushita,⁴ the main contributors to the visible band absorption from the ICl ground state ($X\ 0^+(\text{I})$) are the A $1(\text{I})$, B $0^+(\text{II})$, and C $1(\text{II})$ states which correlate to $\text{I}(^2\text{P}_{3/2}) + \text{Cl}(^2\text{P}_{3/2})$ and the $0^+(\text{III})$ and $1(\text{IV})$ states which correlate to $\text{I}(^2\text{P}_{3/2}) + \text{Cl}(^2\text{P}_{1/2})$. The two exit channels have threshold energies ΔE of 2.15 and 2.26 eV, respectively.⁵



Several groups have explored ICl photochemistry above 480 nm. DeVries *et al.*⁶ report photofragment spectroscopy results in the 480–530 nm range. Probing the Cl fragment, they determined that $\text{Cl}^*({}^2\text{P}_{1/2})$ comes from a parallel transition, while $\text{Cl}({}^2\text{P}_{3/2})$ has both parallel and perpendicular contributions, the latter attributed to curve crossing between B and 0^+ states. In contrast to Child and Bernstein,⁷ they conclude that the A state has minimal contribution to ICl absorption. Zare *et al.* investigated alignment and orientation of Cl photofragments between 490 and 560 nm,^{8,9,10} and report photofragment helicity oscillations due to the interference between A and B states.¹¹ In the UV band, Tonokura *et al.*⁵ studied ICl photolysis and non-adiabatic crossings in the 235–248 nm range and measured branching ratios of 0.68 for Cl^*/Cl and 0.71 for I^*/I , with B, 1(IV) and possibly ${}^3\Sigma^-$ states involved.

Recently we reported our results from slice imaging experiments following ICl excitation from 400 to 570 nm.¹² In agreement with previous work,⁶ we found that the Cl^*/Cl branching ratio increases with dissociation energy from 570 to 490 nm; however, this trend reverses from 490 nm down to 400 nm. The angular anisotropy (β) parameter for the I + Cl channel follows the same behavior, rising from -0.41 at 570 nm to 1.18 at 490 nm and subsequently dropping to -0.42 at 400 nm, while the I + Cl^* channel beta parameter ranges between 1.4 and 0.6 , following the I + Cl channel behavior down to 455 nm but exhibiting the opposite trend from 440 to 400 nm. These results are discussed in light of adiabatic curve crossings and the symmetry of the states involved.

In this chapter our results on the higher energy spectrum are presented. Three distinct wavelengths are studied 235 nm, 250 nm and 265 nm, covering essentially the half width of the absorption spectrum in this region. The results show an almost exclusive production of Cl^* with

ground state Iodine atoms, while the opposite is true for Cl, i.e., the concomitant production of I*.

3.2. Experimental setup

The slicing^{13,14} apparatus used in the experiments has been described in Section 2.1 in detail. A supersonic molecular beam of ICl seeded in He is formed with the seed gas flowing over solid ICl. Because of the low partial pressure of ICl we have used a modified version of the piezo valve shown in Figure 3.1.

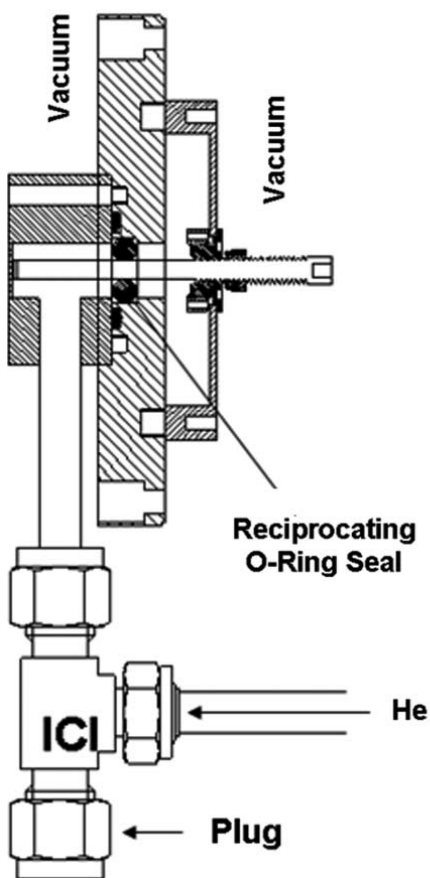


Figure 3.1. Piezo valve design for operation with corrosive gases.

The basic valve design is based on original work of Trickl-Proch¹⁵ with a modification similar to work of Liu and co-workers¹⁶ and similarly Wodtke and co-workers.¹⁷ In order to avoid the exposure of the piezo crystal to the corrosive gas, a bypass chamber is installed that is pressure separated from the piezo containing chamber via an reciprocating O-ring seal on the valve plunger shaft. In our setup we find essentially no degradation in the traditional performance of our pulsed valve using the traditional design.¹⁵ In addition, we have found that the closer the ICl sample lies to the valve orifice the denser the beam appears in ICl. We thus mount a “Swagelock-Type” TEE, one side of which is capped and loaded with solid ICl.

For the slicing experiments reported here, the repeller is pulsed ON at the appropriate time delay (~200 ns for ³⁵Cl, and ~300 ns for ¹²⁷I) following the photolysis and ionization. The pump laser (235nm, 250 nm, and 265 nm) in our experiments is produced by an Nd³⁺:YAG-pumped optical parametric oscillator-amplifier system (Spectra Physics MOPO). Probe laser is the frequency doubled output of an Excimer pumped (Lambda Physik LPX) dye laser (LPD3000) using the appropriate dye (Rhodamin 610 and Coumarin480 from Exciton and Radiant Dyes). The probe laser transitions used are Cl(²P_{3/2}) →→ 4p ²S_{1/2} at 234.632 nm, Cl*(²P_{1/2}) →→ 4p ²P_{1/2} at 235.204 nm, I(²P_{3/2}) →→ 6p ⁴D_{7/2} at 304.578 nm, I*(²P_{1/2}) →→ 6p ⁴D_{1/2} at 304.047 nm (numbers are laser readings).

3.3. Results

3.3.1. I-atom images

Representative images (235, 250, and 265 nm) of the I-atoms fragment distributions following ICl photolysis are presented in Figure 3.2(a) and indicative kinetic energy release (KER) distributions are shown in Figure 3.2(b). Ideally two peaks are expected in the KER peak distribution corresponding to channels (1) and (2). Clearly a whole series of peaks are observed. Overlaying the KER for various photolysis wavelengths we notice that several of these peaks remain un-shifted in energy. Peak assignments are listed in Table 3.1. We assign some of these peaks to “one-color” channels where the probe laser also serves as the photolysis. In addition, we

have been able to also identify contributions to the KER spectrum from contaminants in the molecular beam. Based on known bond dissociation energies we are able to assign these peaks to the presence of IBr in the source as well as I_2 , not surprising as recently performed experiments on CH_3Br could leave traces in the manifold and result in production of IBr.

Using the known dissociation energy for ICl, $D_0 = 2.15$ eV,^{12,18} in the case of 235 nm photolysis, the KER for production of Cl and Cl* is expected at 0.65 and 0.68 eV, respectively. Based on our calibration the main peak in the spectrum is at 0.65 eV, however, being able to distinguish the second channel would require energy resolution of $\Delta E/E \sim 4\%$. We have demonstrated that this resolution should be routinely available to us,¹⁹ however, as we saw in our recent study of ICl in the visible region, hot bands (rotational and even vibrational) hinder the resolution of Cl and Cl* channels.

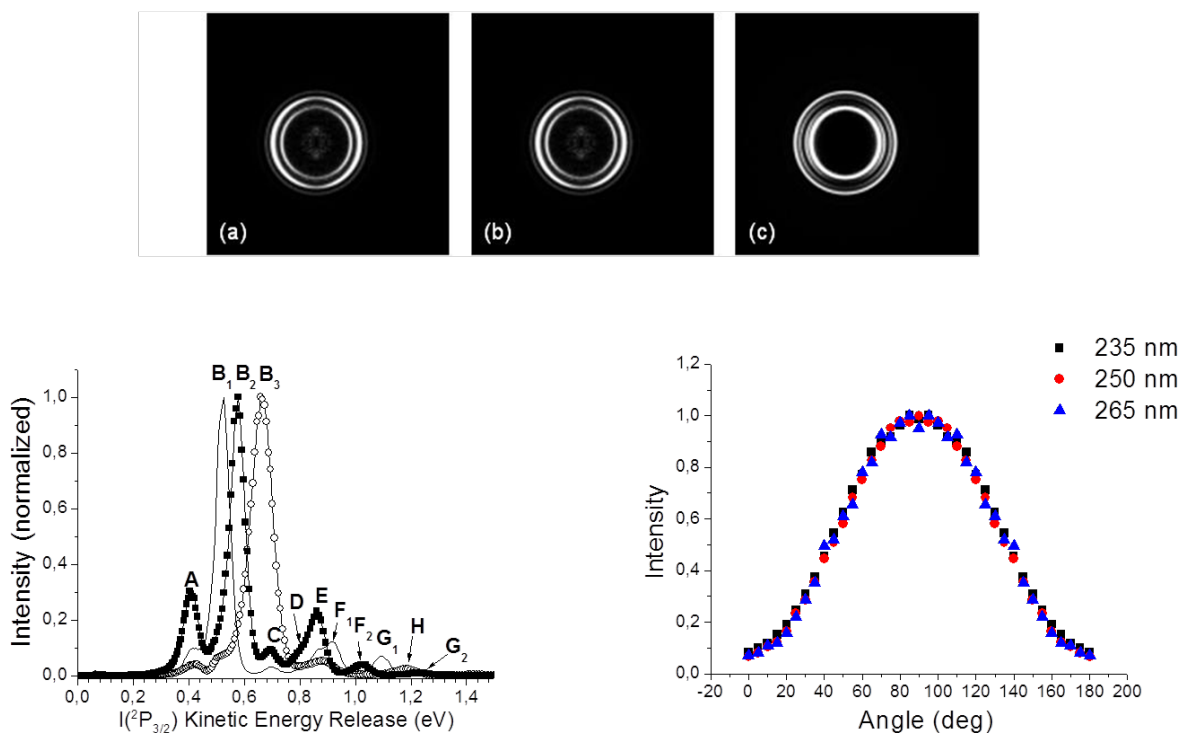


Figure 3.2. (a) I-atom photofragment images at three dissociation wavelengths. At 235 nm, the experiment is performed with a single color. (b) Kinetic energy release (KER) distributions obtained by appropriate radial integration of the slice images shown in caption (a). (c) Angular distributions obtained by appropriate integrating the slice images shown in caption (a).

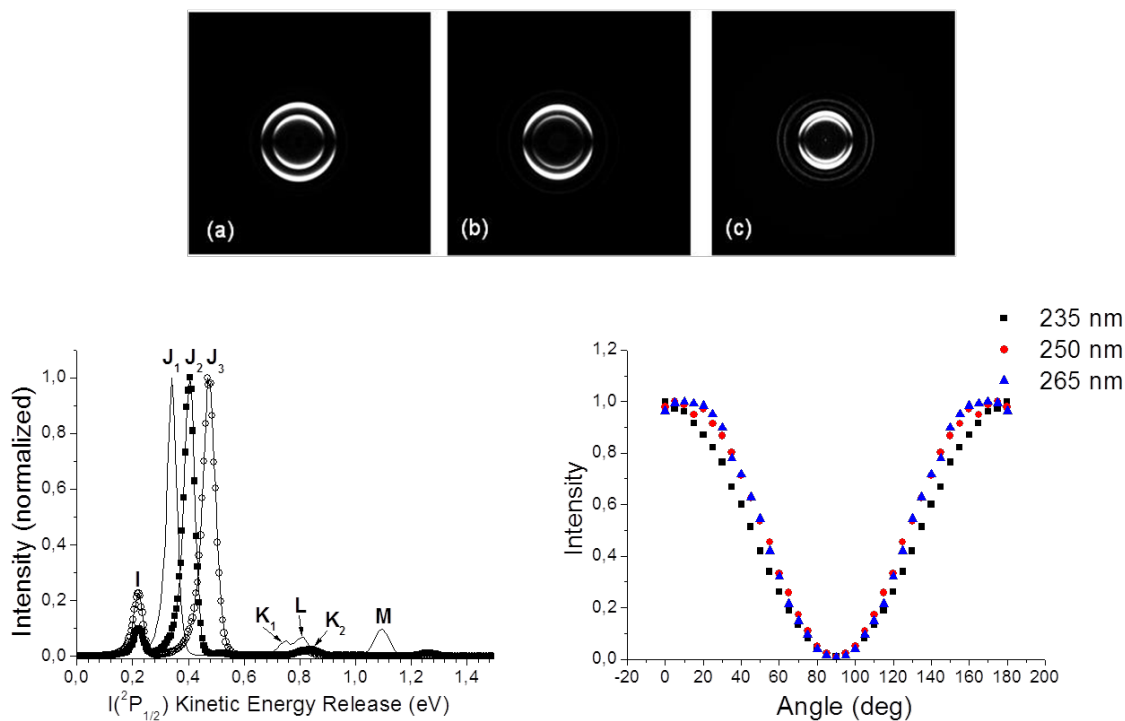


Figure 3.3. I*-photofragment images, KER, and angular distributions.

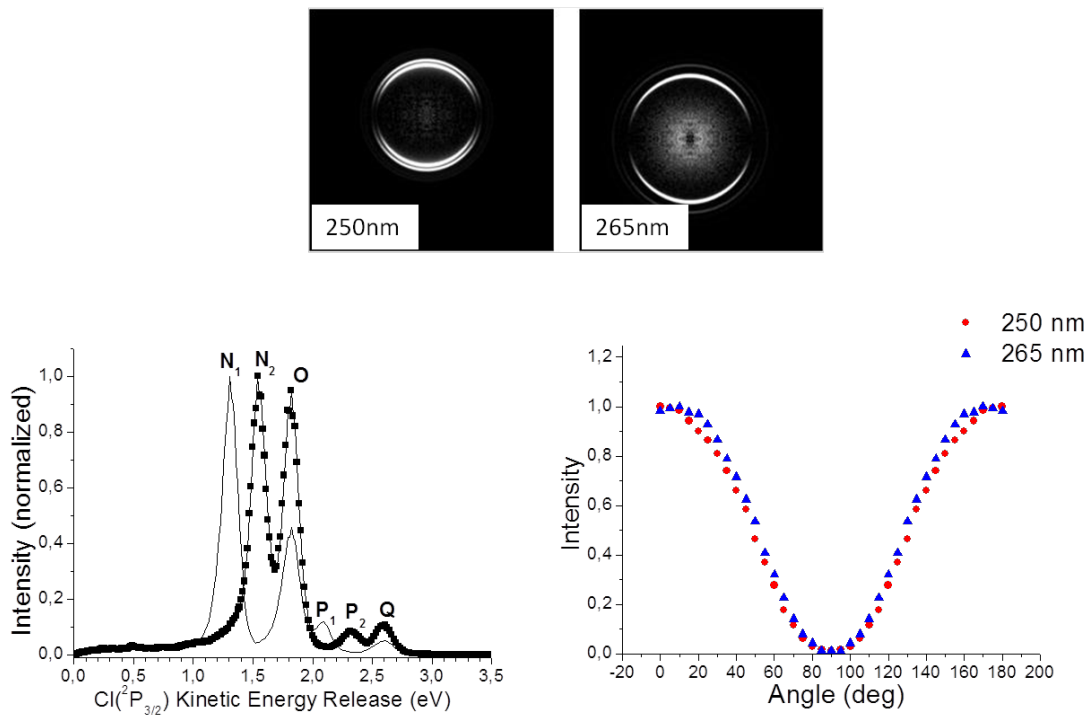


Figure 3.4. Cl-photofragment images, KER, and angular distributions.

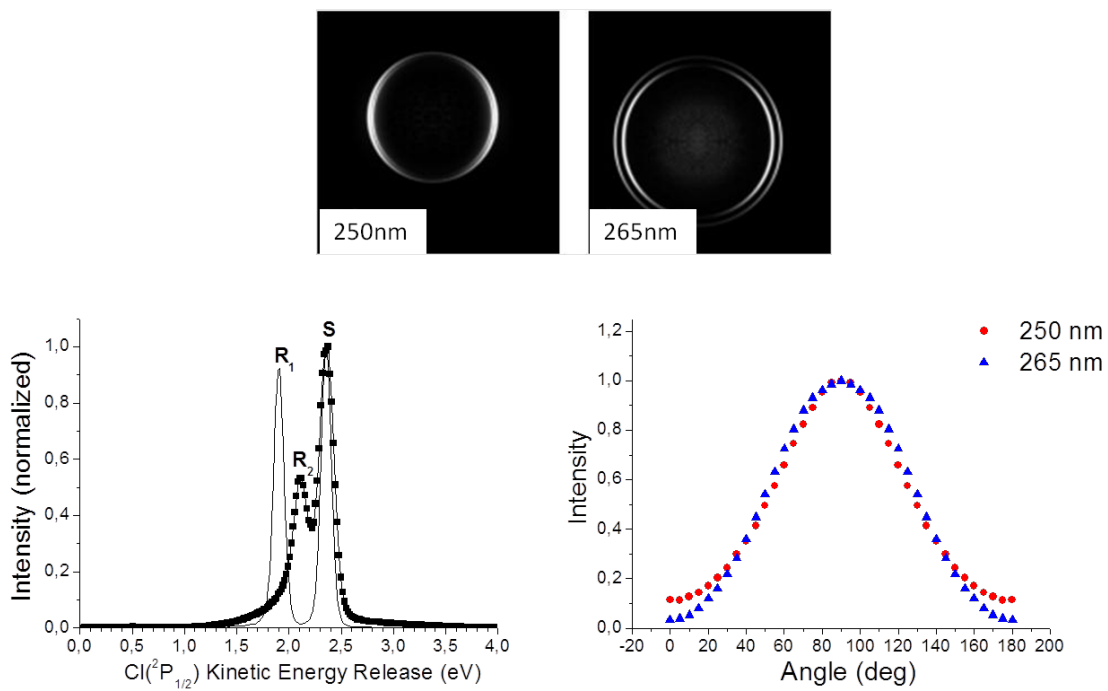


Figure 3.5. Cl*-photofragment images, KER, and angular distributions.

Table 3.1. KER spectra assignments for all channels

A	I+Cl/Cl* (304.5 nm)
B ₁	I+Cl/Cl* (265 nm)
B ₂	I+Cl/Cl* (250 nm)
B ₃	I+Cl/Cl* (235 nm)
C	I+Br* (304.5 nm)
D	I+I* (304.5 nm)
E	I+Br (304.5 nm)
F ₁	I +Br* (265 nm)
F ₂	I +Br* (250 nm)
G ₁	I +Br (265 nm)
G ₂	I +Br (250 nm)
I	I*+Cl (304.0 nm)
J ₁	I*+Cl (265 nm)
J ₂	I*+Cl (250 nm)
J ₃	I*+Cl (235 nm)
K ₁	I*+Br (265 nm)
K ₂	I*+Br (250 nm)
L	I*+I (304.0 nm)
N ₁	Cl+I* (265 nm)
N ₂	Cl+I* (250 nm)
O	Cl+I* (235 nm)
P ₁	Cl+I (265 nm)
P ₂	Cl+I (250 nm)
Q	Cl+I (235 nm)
R ₁	Cl*+I (265 nm)
R ₂	Cl*+I (250 nm)
S	Cl*+I (235 nm)

Table 3.2. Anisotropy parameter results

	β	SD(σ)
I		
235 nm	-0.76	0.05
250 nm	-0.87	0.01
265 nm	-0.88	0.03
I*		
235 nm	1.90	0.13
250 nm	1.65	0.05
265 nm	1.89	0.04
Cl		
235 nm	1.85	0.06
250 nm	1.93	0.06
265 nm	1.71	0.11
Cl*		
235 nm	-0.72	0.05
250 nm	-0.90	0.02
265 nm	-0.99	0.05

To help resolve the contribution of these two channels we consider spatial anisotropy of the I-atom photofragment and will make the comparison with the respective images of Cl and Cl* later. A typical angular distribution for I is shown in Figure 3.2 (c). In the case of I atoms we

did not check for atomic alignment as our results for Cl (see later) showed no significant alignment. We fit the angular distribution using the well know equation $I(\theta) \sim 1 + \beta P_2(\cos\theta)$ and the results are shown in Table 3.2. We observe a negative near limiting $\beta \sim -0.9$ value on the low energy side of the absorption (250 and 265 nm) and a slightly reduced value of -0.8 at 235 nm. The near limiting β value suggests that the dissociation most probably takes place on a single excited potential energy surface, i.e., non-adiabatic transitions are insignificant.

3.3.2. I*-atom images

Representative images (235, 250, and 265 nm) of the I*-atoms fragment distributions following ICl photolysis are presented in Figure 3.3(a) and indicative KER distributions are shown in Figure 3.3(b). As in the case of I-atoms described above, a whole series of “unexpected” peaks are observed, that are assigned and detailed assignments are listed in Table 3.1. Once again being able to distinguish the two channels (Cl/Cl*) is energetically not possible and will be elucidated by considering the angular distributions. Typical angular distribution for I is shown in Figure 3.3(c), and limiting values are observed as in the case of I photofragments, however, in the opposite positive limit of +2. We observe a $\beta \sim 1.9$ on either side of the absorption minimum and a slightly reduced value 1.65 at the maximum. Once again the near limiting β value suggests that the dissociation most probably takes place on a single potential energy surface, and possibly some non-adiabatic transitions manifest themselves near the absorption maximum at 250 nm; these will be discussed later.

3.3.3. Cl-atom images

Representative images (235, 250, and 265 nm) of the Cl-atoms fragment distributions following ICl photolysis are presented in Figure 3.4(a) and indicative KER distributions of the Cl-atom fragment are shown in Figure 3.4(b). The large S.O. splitting in Iodine atoms (0.94 eV) allows channels (1) and (3) to be clearly resolved. From the KER spectrum shown in Figure 3.4(b) we are able to extract the I/I* branching ratio for these two channels and find it to be $\sim 10\%$ throughout the wavelengths region studied. In addition β values for the I* channel are near

limiting (see Table 3.2) at ~ 1.9 . The β value for the I channel because of the weak signal yields large error bars, but we can safely conclude however that $\beta > 1$.

3.3.4. Cl*-atom images

Representative images (235, 250, and 265 nm) of the Cl*-atoms fragment distributions following ICl photolysis are presented in Figure 3.5(a) and indicative KER distributions of the Cl-atom fragment are shown in Figure 3.5(b). From the KER, within the signal to noise we observe no sibling I* production for the Cl* channel. In blowing up the image contrast we do see some “trace-evidence” that cannot be quantified leading us to conclude that the I/(I* + I) ratio for Cl* is $\sim 100\%$. The β values for Cl* reach -0.7 at 235 nm and approach the limiting value of -1.0 at lower energies.

3.4. Discussion

While there have been three previous experimental measurements of the ICl photodissociation in the region reported here,^{5,20,21} all three of them seem to differ not only in the branching ratios of the four possible channels but even in the angular distribution of the products leading to different excited electronic assignments. In Figure 3.6 we show a schematic of the most recent potential energy surfaces calculated by Yabushita.⁴

As mentioned earlier channel (4) than leads to I* + Cl* is essentially not observed, and is probably the single common observation in all studies of ICl in this region.^{5,20,21} This can be understood in terms of poor Franck-Condon factors in this energy range, between the X(0⁺, 2440) and the V(0⁺, 2422 and 2332) states, where the notation (pqrs) stands for electronic configuration $\sigma^p \pi^q \pi^r \sigma^{*s}$.^{4,5} In addition the 0⁺(V) state does not seem to cross with an other electronic state, and the large S.O. splitting in iodine sets this state well separated from the other excited electronic states in this region.

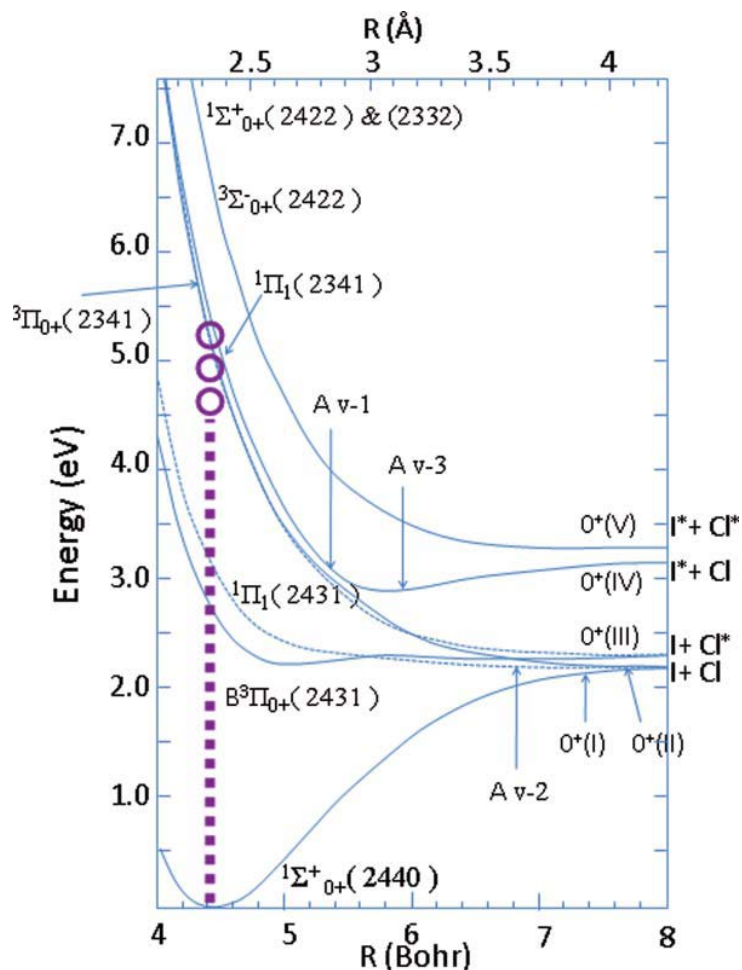


Figure 3.6. Schematic drawing of the potential energy surfaces for the states involved in ICl absorption from Yabushita (Ref. 4). The vertical dashed lines and the three circles indicated the region accessed in current experiments.

We now consider channel (2), the only remaining channel producing Cl*. Two sets of information are available depending on which photofragment species is being probed. Comparison of the Cl* and I results in Tables 3.1 and 3.2 leads to some interesting suggestions /assertions. Comparing the β values we notice that these are nearly identical within the statistical error bars, and though approaching a limiting value of -1 , the slight variation might be informative in deciphering these complex dynamics *albeit* diatomic species. Two factors could possibly reduce the β value: (a) non-prompt dissociation (excited-state lifetime) and (b) multiple electronic states of opposing symmetry involved. Based on the excited state potentials of Figure 3.6, the excitation energies in the present study are well above any “bound” part of the potentials

and the molecule is placed on the repulsive part of the excited states upon absorption of a photolysis photon. In addition the small rotational constant of ICl ($B \sim 0.1 \text{ cm}^{-1}$) implies slow rotational motion as expected for two heavy atoms such as Cl and I. Hence we see no reason for anything else except prompt dissociation of ICl in this part of the energy spectrum.

Considering the multiple surface scenario we examine the excited potential energy surfaces involved, i.e., the $^3\Pi_{0^+}$ (2341), $^1\Pi_1$ (2341), and $^3\Sigma_{0^+}^-$ (2422), that according to the calculations,^{2-4,5} are the major contributors to the absorption spectrum at the three wavelengths studied in the report. When considering the spin-orbit interaction in these states a series of $\Omega = 0$ and $\Omega = 1$ states result, of which, the states that correlate to the channel $\text{Cl}^* + \text{I}$ are the $1(\text{IV}, ^1\Pi_1)$ and the $0^+(\text{III}, ^3\Pi_{0^+})$ states.⁵ When the photolysis wavelength is 265 nm, β is essentially limiting so we can safely conclude that the $1(\text{IV})$ state is the dominate state involved. However, the calculated transition dipole moment strength in this region indicates that transitions to the $^3\Pi_{0^+}$, $^1\Pi_1$ and $^3\Sigma_{0^+}^-$ (2422) are approximately equivalent, and if anything the $^3\Pi_{0^+}$ shows the strongest propensity. So if the transition is to remain strictly perpendicular ($\beta \sim -1$), the contributions of the $\Omega = 0$ states must be somehow “eliminated.”

One possibility is the Avoided Crossing (Av2) at $\sim 6.8 \text{ \AA}$. The Landau-Zener probability is calculated to be $P_{LZ}^{\text{Av2}} \sim 91\%$ and this would be a great “sink” of any parallel-transition ($\Omega = 0$ excited state) contribution. The contribution of the $\Omega = 0$ states is greater at shorter wavelengths (see reduced β values in table 3.2), and we can estimate the contribution of the parallel component in our experimental data using the relation

$$I(\theta) = A \left[\frac{3}{2} \cos^2 \theta \right] + B \left[\frac{3}{4} \sin^2 \theta \right],$$

$$\text{where } A = \frac{1+\beta}{3} + B \left[\frac{3}{4} \sin^2 \theta \right], \text{ and } B=1-A.$$

For 235 nm, lowest wavelength studied here, $\beta = -0.7$ so, $A = 0.1$, and $B = 0.9$, which essentially means that our observed ratio of the *parallel* $0^+(\text{III})$ and $0^+(\text{IV})$ to *perpendicular* $1(\text{IV})$ contribution to the $\text{I} + \text{Cl}^*$ channel is

$$\frac{(I+Cl^*)_{\Omega=0}}{(I+Cl^*)_{\Omega=1}} \approx 0.11.$$

Based on the potential energy surfaces of Figure 3.6 we can attempt to predict the experimental ratios determined above. Specifically

$$\begin{aligned} \frac{(I+Cl^*)_{\Omega=0}}{(I+Cl^*)_{\Omega=1}} &= (1 - P_{LZ}^{Av2}) \frac{(1 - P_{LZ}^{Av1})\alpha(^3\Pi_{0^+}) + P_{LZ}^{Av1}\alpha(^3\Sigma_{0^+}^-)}{a(^1\Pi_1)}, \\ &= (1 - 0.91) \frac{(1 - 0.8) \cdot 179 + (0.8) \cdot 99}{157} = 0.07. \end{aligned}$$

where $P_{LZ}^{Av1} \sim 0.8$ is Landau-Zener transition probability for the avoided crossing between the $^3\Pi_{0^+}$ and $^3\Sigma_{0^+}^-$ at ~ 5.4 Å, and $\alpha(\Gamma)$ is the transition dipole moment for the respective electronic state.^{4,5} The agreement with the experiment is very good!

Continuing our “modeling” of the dynamics we can estimate the branching ratio between channels (1) and (3)

$$\begin{aligned} \frac{(I+Cl)}{(I^*+Cl)} &= \frac{\text{Channel(1)}}{\text{Channel(3)}}, \\ &= \frac{(P_{LZ}^{Av2}) \left[(1 - P_{LZ}^{Av1})\alpha(^3\Pi_{0^+}) + P_{LZ}^{Av1}\alpha(^3\Sigma_{0^+}^-) \right]}{P_{LZ}^{Av1}\alpha(^3\Pi_{0^+}) + (1 - P_{LZ}^{Av1})\alpha(^3\Sigma_{0^+}^-)}, \\ &= \frac{0.91 \cdot [(1 - 0.8) \cdot 179 + (0.8) \cdot 99]}{0.8 \cdot 99 + (1 - 0.8) \cdot 99} = 0.70. \end{aligned}$$

Analysis of the KER distributions of Cl photofragments at all wavelengths studied yields a propensity ratio for production of

$$\frac{(I+Cl)}{(I^*+Cl)} = \frac{\text{Channel(1)}}{\text{Channel(3)}} \approx 0.10,$$

in complete contrast with the theoretical predictions. If we were to “adjust” the theory numbers to fit our experimental observations, we would have $\alpha(^3\Sigma_{0^+}^-)$ reduced by a factor of five (20

instead of 99), and the $P_{LZ}^{Av1} \sim 0.9$ (instead of 0.8) and $P_{LZ}^{Av1} \sim 0.7$ (instead of 0.9). The major deviation appears to be the contribution of the ${}^3\Sigma_{0+}^-$ to the spectrum, as the curve-crossing probabilities are not that different for what theory predicts.

3.5. Conclusion

We have studied the photodissociation dynamics of ICl in the UV region between 235 and 265 nm. The spectrum in this region is dominated (~95%) by transitions to the ${}^3\Pi_{0+}$, ${}^1\Pi_1$ while the ${}^3\Sigma_{0+}^-$ excited state contributes only about 5% to the overall spectrum. The $I^* + Cl^*$ channels is not active in this region while the branching ratios of the remaining 3 channels are estimated at

$$\frac{(I+Cl)}{(I^*+Cl)} = \frac{\text{Channel(1)}}{\text{Channel(3)}} \approx 0.10, \frac{(I+Cl)}{(I+Cl^*)} = \frac{\text{Channel(1)}}{\text{Channel(2)}} \leq 0.10,$$

$$\frac{(I^*+Cl)}{(I+Cl^*)} = \frac{\text{Channel(3)}}{\text{Channel(2)}} \approx 1.$$

In other words the photolysis of the ICl in this region produces about equal amounts of Cl and Cl^* , with distinct kinetic energies, and distinct distributions in space, suggesting that ICl could potentially be used as a suitable precursor for studying the relative reactivity of Cl and Cl^* .

References

- ¹ D. J. Seery and D. Britton, “The continuous absorption spectra of chlorine, bromine, bromine chloride, iodine chloride, and iodine bromide”, *J. Phys. Chem.* **68**, 2263 (1964).
- ² K. Balasubramanian, “Relativistic calculations of the spectroscopic properties of low-lying states of ICl”, *J. Mol. Spectr.* **110**, 339 (1985).
- ³ K. Balasubramanian, “Relativistic configuration-interaction calculations of the low-lying states of ICl and ICl⁺”, *Chem. Phys.* **95**, 225 (1985).
- ⁴ S. Yabushita, “Potential energy curves of ICl and non-adiabatic interactions studied by the spin-orbit CI method”, *J. Mol. Struct.: THEOCHEM* **461–462**, 523 (1999).
- ⁵ K. Tonokura, Y. Matsumi, M. Kawasaki, H. L. Kim, S. Yabushita, S. Fujimura, and K. Saito, “Photodissociation of ICl at 235–248 nm”, *J. Chem. Phys.* **99**, 3461 (1993).
- ⁶ M. S. de Vries, N. J. A. van Veen, M. Hutchinson, and A. E. de Vries, “Curve crossing and repulsive potentials probed by laser induced half collisions: ICl and IBr”, *Chem. Phys.* **51**, 159 (1980).
- ⁷ M. S. Child and R. B. Bernstein, “Diatomic interhalogens: Systematics and implications of spectroscopic interatomic potentials and curve crossings”, *J. Chem. Phys.* **59**, 5916 (1973).
- ⁸ T. P. Rakitzis, S. A. Kandel, and R. N. Zare, “Photolysis of ICl causes mass-dependent interference in the Cl(²P_{3/2}) photofragment angular momentum distributions *J. Chem. Phys.* **108**, 8291 (1998).
- ⁹ T. P. Rakitzis, S. A. Kandel, A. A. Alexander, Z. W. Kim, and R. N. Zare, “Measurements of Cl atom photofragment angular momentum distributions in the photodissociation of Cl₂ and ICl. *J. Chem. Phys.* **110**, 3351 (1999).
- ¹⁰ A. J. Alexander and T. P. Rakitzis, “Effects of long-range potentials on polarization of chlorine atoms from photodissociation of ICl”, *Mol. Phys.* **103**, 1665 (2005).
- ¹¹ T. P. Rakitzis, S. A. Kandel, A. J. Alexander, Z. H. Kim, and R. N. Zare, “Photofragment helicity caused by matter-wave interference from multiple dissociative states”, *Science* **281**, 1346 (1998).
- ¹² P. C. Samartzis and T. N. Kitsopoulos, “Branching ratios and anisotropy parameters in icl photolysis from 400 to 570 nm using slice imaging”, *J. Chem. Phys.* **133**, 014301 (2010).

- ¹³ C. R. Gebhardt, T. P. Rakitzis, P. C. Samartzis, V. Ladopoulos, and T. N. Kitsopoulos, “A new approach to ion imaging and velocity mapping”, *Rev. Sci. Instrum.* **72**, 3848 (2001).
- ¹⁴ V. Papadakis and T. N. Kitsopoulos, “Slice imaging and velocity mapping using a single field”, *Rev. Sci. Instrum.* **77**, 083101 (2006).
- ¹⁵ D. Proch and T. Trickl, “A high-intensity multi-purpose piezoelectric pulsed molecular beam source”, *Rev. Sci. Instrum.* **60**, 713 (1989).
- ¹⁶ F. Dong, S.-H. Lee, and K. Liu, “F. Dong, S.-H. Lee, and K. Liu. Reactive excitation functions for $F + p\text{-H}_2 / n\text{-H}_2 / D_2$ and the vibrational branching for $F + HD$ ”, *J. Chem. Phys.* **113**, 3633 (2000).
- ¹⁷ Q. Ran, D. Matsiev, D. J. Auerbach, and A. M. Wodtke, “An advanced molecule-surface scattering instrument for study of vibrational energy transfer in gas-solid collisions”, *Rev. Sci. Instrum.* **78**, 104104 (2007).
- ¹⁸ G. Herzberg, *Molecular Spectra and Molecular Structure, Vol. I, Spectra of Diatomic Molecules* (Van Nostrand Reinhold, New York, 1950).
- ¹⁹ R. L. Toomes, P. C. Samartzis, T. P. Rakitzis, and T. N. Kitsopoulos, “Slice imaging of H-atom photofragments: effects of the REMPI detection process on the observed velocity distribution”, *Chem. Phys.* **301**, 209 (2004).
- ²⁰ C.-K. Ni and G. W. Flynn, “State and velocity distributions of Cl atoms produced in the photodissociation of ICI at 237 nm”, *Chem. Phys. Lett.* **210**, 333 (1993).
- ²¹ L. J. Rogers, M. N. R. Ashfold, Y. Matsumi, M. Kawasaki, and B. J. Whitaker, “The photodissociation of iodine monochloride at 235 nm”, *Chem. Phys. Lett.* **258**, 159 (1996).

Chapter IV

Driving photochemistry by clustering: The ICl-Xe case

4.1. Introduction

Understanding the photochemistry at the molecular level in the bulk requires an answer to the question: How does photodissociation change with solvation from the individual molecule to the corresponding bulk? Photodissociation studies in clusters are a viable approach to tackle this problem. In this respect, clustering of molecules with xenon atoms can provide a valuable insight: Xe as the rare gas atom serves as an archetype of chemically non-reactive solvent, yet its interaction can be strong enough to cause electronic effects. In addition, due to its high mass it tends to cluster easily with molecules in supersonic expansions.

Recent experimental and theoretical work on photolysis of pyrrole (Py) found drastic changes in photochemical behavior of pyrrole when seeded in Xe.^{1,2} The formation of Py-Xe clusters essentially “quenches” the N-H bond breaking for excitation wavelengths longer than 240 nm. This was explained² by qualitative altering of the shape of the excited state potential curve in the cluster. More recently, we have observed the influence of Xe clustering on HBr molecule.³ While in the pyrrole case, the *electronic interaction* of pyrrole molecule with a single Xe atom explained the experimental results, in the case of HBr it was the *mechanistic effects* of

*caging, delayed cage exit, and direct exit*⁴ that were implemented to explain the HBr molecule photodissociation in large Xe-clusters.

To understand the interplay between electronic and mechanistic effects of molecule-Xe clustering, we selected to study the effects of Xe on the photochemistry of ICl. The ICl/Xe system is closer to HBr/Xe case as a diatomic is also involved, so the mechanistic effects proposed for HBr/Xe might also apply. On the other hand, heteroatomic dihalogen molecules like ICl exhibit significant electronic interaction effects such as predissociation, curve crossings, and avoided crossings in the excited state potential curves,^{5,6,7} which might be affected by clustering with Xe.

In Chapter III the results of photodissociation experiments on ICl in UV region⁸ at three distinct wavelengths 235 nm, 250 nm, and 265 nm are discussed. This wavelength region covers essentially the half width of the absorption spectrum in this region. The results show an almost exclusive production of Cl* with ground state iodine atoms, while the opposite is true for Cl, i.e., the concomitant production of I*. In accordance with all previous studies of ICl in this region,^{7,9,10,11} we did not observe channel leading to I*+Cl* production, which is probably the single common observation.

In this chapter, slice imaging results on the 235 nm photolysis of ICl seeded in Xe and He are reported and compared. Following photolysis in Xe, Cl, and Cl* photofragment energy distributions become broader and appear at 0.1–0.15 eV *higher* kinetic energy than for the photolysis in He. For the I and I* fragment distributions, the change is more dramatic: the sharp rings at 0.65 eV (I+Cl* channel) and 0.47 eV (I*+Cl channel) of He photolysis are replaced in Xe with broad distributions extending from 0 all the way to 2.5 eV. Possible explanations for those observations are discussed in Section 4.4.

4.2. Experimental setup

The slice imaging technique used in the experiments has been described in Section 2.1. in detail. A supersonic molecular beam of ICl seeded in He or Xe (1100 mbar total backing pressure) is formed with the seed gas flowing over solid ICl at room temperature. This way we

generate ICl-Xe and ICl-He mixtures with ICl concentration <4%. For the ICl-Xe beam, the nozzle-laser pulse delay is adjusted so that the laser photons excite the species at the peak of the molecular beam velocity distribution, where the strong clustering regime prevails.³ For the ICl-He beam, the nozzle-laser delay is adjusted so that the laser excites the species arriving at the interaction region 40–50 μ s earlier than the peak of the molecular beam velocity distribution, thus, exciting only isolated ICl molecules. For the slicing experiments reported here, the repeller is pulsed ON at the appropriate time delay (\sim 200 ns for ³⁵Cl, and \sim 300 ns for ¹²⁷I) following the photolysis and ionization. The Cl and Cl* photofragment images are recorded in a one-color experiment where one photon is used to dissociate the ICl molecule followed by (2+1) REMPI (Resonance-Enhanced Multi-Photon Ionization) of the chlorine photofragment within the same laser pulse. The laser beam is generated by a Nd³⁺:YAG pumping a master oscillator power oscillator system (Spectra Physics MOPO). The probe laser transitions used for the detection of Cl and Cl* photofragments are Cl(²P_{3/2}) $\rightarrow\rightarrow$ 4p (²D_{3/2}⁰) at 235.326 nm and Cl*(²P_{1/2}) $\rightarrow\rightarrow$ 4p (²S_{1/2}⁰) at 235.195 nm (wavelengths corrected for laser drift).

The I and I* photofragment images are obtained in a two-color experiment following the photolysis of ICl at 235 nm and (2+1) REMPI of the photofragments, where the laser pulses are separated in time by about 10 ns. The probe laser beam is the frequency doubled output of an excimerpumped (Lambda Physik LPX, operating with XeCl) dye laser (LPD3000) using the appropriate dye (Rhodamin 610). The I and I* photofragments were probed via I(²P_{3/2}) $\rightarrow\rightarrow$ 6p (⁴D_{7/2}) at 304.553 nm and I(²P_{1/2}) $\rightarrow\rightarrow$ 6p (⁴D_{1/2}) transition at 304.024 nm, respectively. Background images are recorded with the lasers on and the molecular beam off and subtracted from the signal images.

4.3. Results

4.3.1. Cl and Cl* photofragments

Slice images of the Cl photofragments when using He and Xe as the carrier gases are shown in Figures 4.1(a) and 4.1(b), respectively. Figure 4.1(a), obtained when using He as the

carrier gas, shows two sharp rings: the inner one corresponds to the Cl+I* exit channel and the outer to the Cl+I channel. The two rings were used to calibrate the kinetic energy release (KER) distribution of Cl photofragments. In Figure 4.1(b), obtained with Xe as the carrier gas, we observe two diffuse rings and an intense feature in the center of the image.

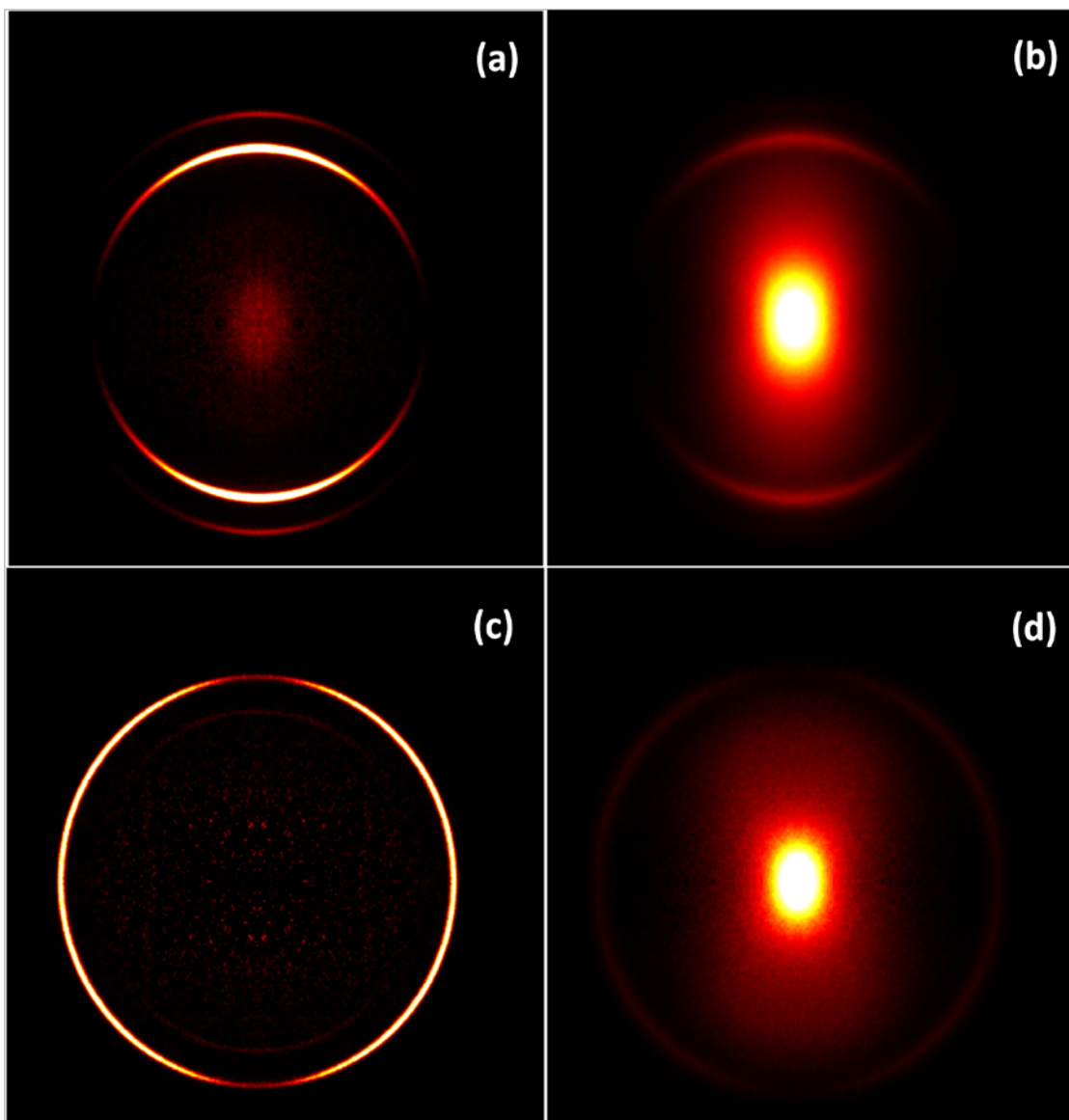


Figure 4.1. (Top) Cl-photofragment slice images following the photolysis of ICl at 235.326 nm recorded using (a) He and (b) Xe as the carrier gas. (Bottom) Cl*-photofragment slice images following the photolysis of ICl at 235.195 nm recorded using (c) He and (d) Xe as the carrier gas.

This central feature is indicative for the formation of clusters and usually appears as a result of caging processes in which the observed fragments lose their kinetic energy in inelastic collisions with the cluster constituents and are detected as near-zero-kinetic energy fragments.³

Figure 4.2(a) shows the KER spectra of the Cl photofragments obtained from the images in Figures 4.1(a) and 4.1(b) when using for calibration the value of $D_0(\text{ICl}) = 2.15$ eV.¹² In the KER spectrum obtained with He, we observe two distinct peaks at 1.71 and 2.45 eV corresponding to the I^* and I producing channels, respectively. When seeding in Xe, the KER spectrum differs substantially showing a slower, wide distribution of a statistical character peaking at around 0.1 eV and two high-energy peaks at 1.81 and 2.55 eV, which are substantially broader and faster when compared to the two peaks from ICl photodissociation in He.

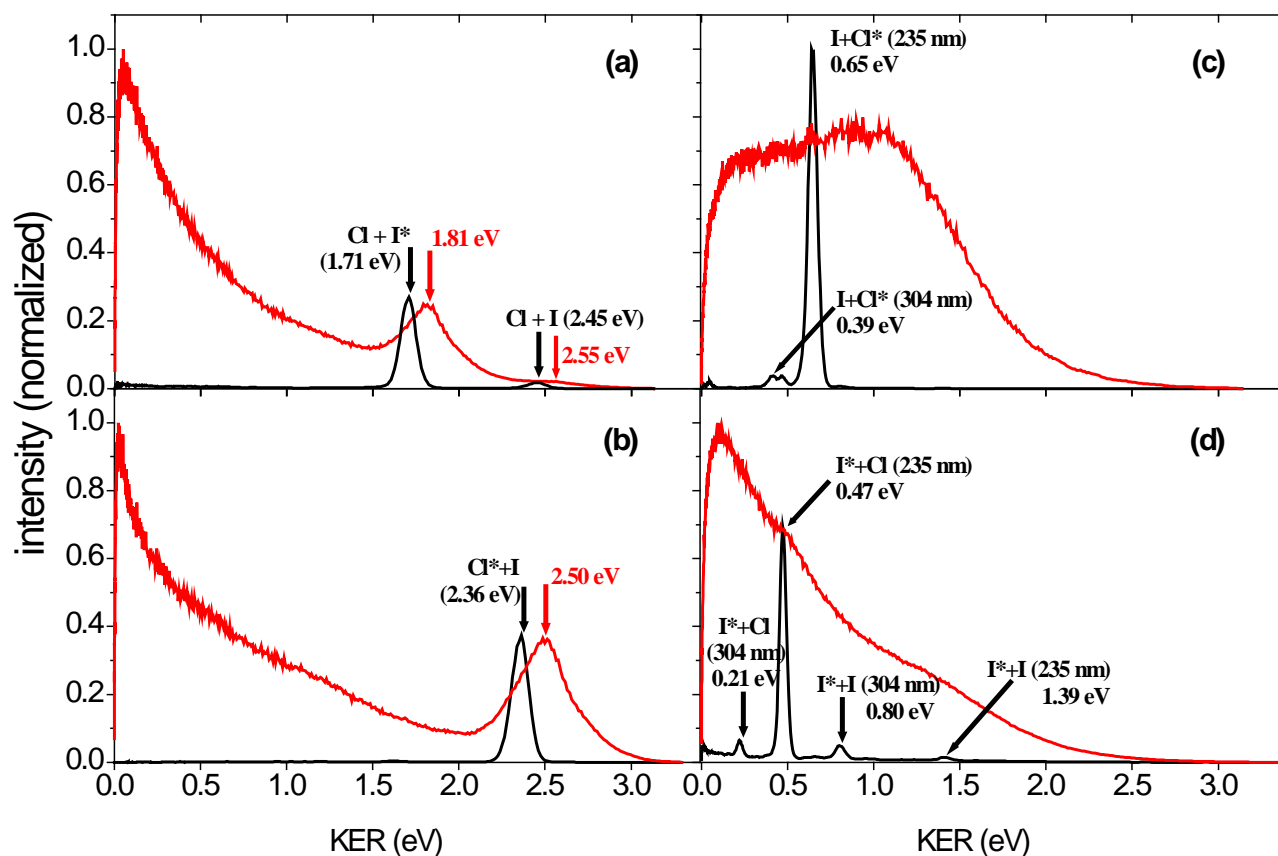


Figure 4.2. KER distributions of $\text{Cl}(^2P_{3/2})$, $\text{Cl}(^2P_{1/2})$, $\text{I}(^2P_{3/2})$, and $\text{I}(^2P_{1/2})$ photofragments are shown in panels (a), (b), (c), and (d), respectively. The black and red lines represent KER distributions obtained using He and Xe as the carrier gas, respectively. The red marks indicate the peak position of the fast component: 1.81 and 2.55 eV in the case of $\text{Cl}(^2P_{3/2})$, and 2.50 in the case of $\text{Cl}(^2P_{1/2})$.

Slice images of the Cl* photofragments when using He as the carrier gas (Figure 4.1(c)) exhibit an intense sharp ring which corresponds to Cl*+I exit channel at 235 nm. A second faint ring (not quite distinguishable in Figure 4.1(c)) appears at a smaller radius corresponding to a KER of 1.62 eV. Energetically this ring could be assigned to the Cl*+I* channel, however, our previous study⁸ has shown that this channel has zero propensity at this excitation wavelength. It is more likely that it is due to Cl+I channel, where the Cl photofragment undergoes non-resonant MPI. When using Xe as the carrier gas, the Cl* photofragment image consists of a diffuse ring and an intense central feature, as shown in Figure 4.1(d). Figure 4.2(b) shows the KER spectra of the Cl* photofragments obtained from the images in Figures 4.1(c) and 4.1(d). Similar to the case of the Cl photofragments, when using He we observe one peak at 2.36 eV corresponding to the Cl*+I channel, while the Xe KER features a wide distribution peaking at low kinetic energy and a wide high-energy peak at 2.50 eV which is broader and faster compared to the peak from photodissociation in He.

4.3.1. I and I* photofragments

Figures 4.3(a) and 4.3(b) show slice images of the I($^2P_{3/2}$) photofragments when using He and Xe as the carrier gas, respectively. The image obtained with He shows several rings with the outer one being the most intense. Weaker structures in the center of the image are due to impurities in the gas line, however, they do not interfere with our present analysis. A diffuse ring and a central feature are observed when seeding in Xe.

Figure 4.2(c) shows the KER spectra of the I photofragments obtained from the images in Figures 4.3(a) and 4.3(b). In the KER spectrum in He, we observe an intense peak at 0.65 eV corresponding to the I+Cl* channel at 235 nm, and a weak peak at 0.39 eV due to photolysis at 304.6 nm by the probe laser, while the additional inner rings of Figure 4.3(a) have no appreciable intensity in the KER spectrum and could be attributed to dissociative ionization of ICl or I₂ impurity. When seeding in Xe, we observe only a broad distribution extending to ~2.5 eV, which is significantly higher kinetic energy than that expected for the ICl monomer.

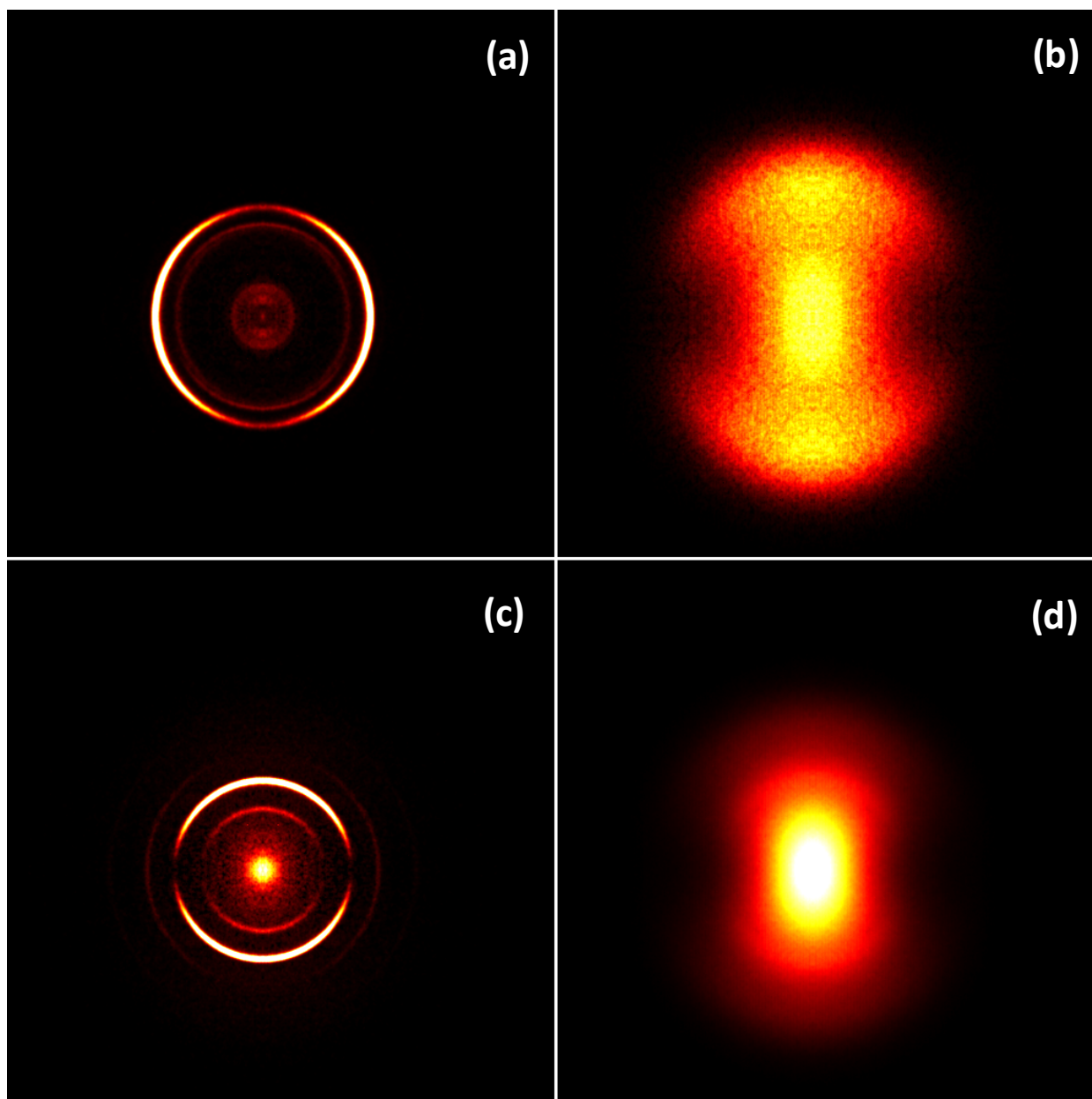


Figure 4.3. (Top) I-photofragment slice images following the photolysis of ICl at 235 nm recorded using (a) He and (b) Xe as the carrier gas. The experiment was performed with two colors. (Bottom) I*-photofragment slice images following the photolysis of ICl at 235 nm recorded using (c) He and (d) Xe as the carrier gas.

Figures 4.3(c) and 4.3(d) show slice images of the $I^*(^2P_{1/2})$ photofragments when using He and Xe as the carrier gas, respectively. The image obtained with He shows several sharp rings, which practically disappear in the case of Xe and a central feature, which could be

attributed to beam impurities, dissociative ionization, or even I₂/ICl cluster formation. In any case, the contribution of this feature to the overall signal is small as seen in Figure 4.2(d) and does not affect our analysis. Figure 4.2(d) shows the KER spectra of the I* photofragments obtained from the images in Figures 4.3(c) and 4.3(d). In the KER spectrum in He, we have identified the peaks as originating from the I*+Cl and I*+I exit channels of ICl and I₂ dissociation at 235 nm and 304 nm. When using Xe, we observe a broad distribution that peaks at low but extends to significantly higher (~2.5 eV) kinetic energy release than expected for the monomer. In Section 4.4, we discuss our findings based on a rather simplified model of cluster dynamics. This discussion points out the need of a detailed theoretical investigation.

4.4. Discussion

4.4.1. Cl and Cl* photofragments

The Cl and Cl* photofragment images obtained using He show only sharp rings as observed before⁸ due to photodissociation of the ICl monomer. For the Xe expansion, the images have two features: an intense “blob” feature in the middle of the image, and outer rings broader in distribution and higher in energy with respect to their He counterparts. The central feature points to cluster generation as outlined above. The broad distribution in the corresponding KER spectra of both Cl and Cl* decays exponentially up to ~2–2.5 eV suggesting that the fragments are formed as a result of dissociation of an ensemble of ICl-Xe clusters of different sizes. This part of the Cl and Cl* KER distributions can be well fit with the following function:

$$f(E) = A_1 e^{-B_1 E} , \quad (4.1)$$

or with an equivalent expression in the velocity space:

$$f(v) = A_1 e^{-B_1 E} , \quad (4.2)$$

as seen in Figure 4.4, where E and v are KER and speed of Cl photofragments, while A and B are the fitting coefficients. This statistical distribution fit is typical for fragments generated in a larger cluster, which lose their kinetic energy due to collisions on their way out of the cluster as

previously described by Buck and Farnik.^{3,4} Thus, we propose that this part of the distribution can be attributed to formation of large Xe_n clusters with ICl molecule(s) embedded inside. After ICl photodissociation, the fragments undergo either *delayed cage exit* or the *cage effect*.⁴ The Cl atoms interact several times with the surrounding Xe atoms and leave the cluster with lower velocity than in the case of dissociation of ICl monomer, thus, explaining the low kinetic energies observed. The fast rings are closer to ICl monomer photolysis as indicated by their angular distribution, however, they have increased kinetic energy release, inconsistent with an ICl monomer dissociation. A possible interpretation is the existence of small clusters consisting of several Xe atoms where ICl molecules are attached to the surface. Dissociation of the I-Cl bond in those clusters would leave $\text{Xe}_n\text{-I}$ fragments behind and could explain the higher kinetic energies of Cl according to

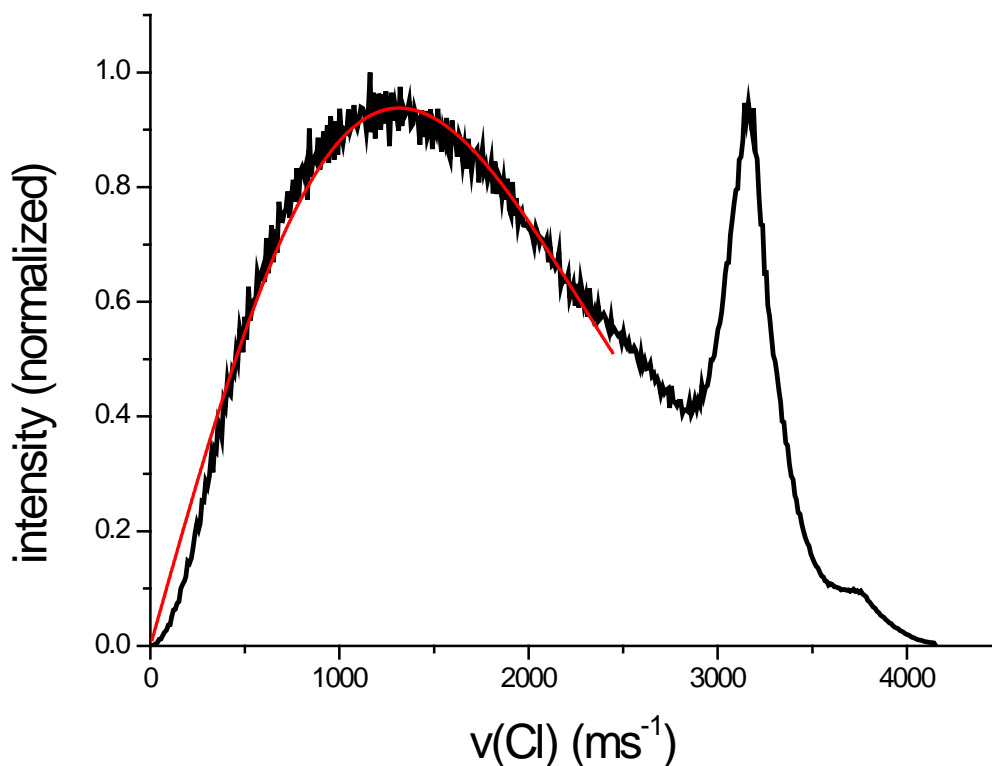


Figure 4.4. Speed distribution of Cl photofragments. The red line presents the fitted exponential function.

The KERs of Cl photofragments escaping from such clusters of increasing size are calculated based on the formula below:

$$E_{\text{Cl}} = (E_{\text{laser}} - D_0 - E_{\text{int}}) \times \frac{m_{\text{Xe}} \times n + m_{\text{I}}}{m_{\text{Xe}} \times n + m_{\text{I}} + m_{\text{Cl}}}, \quad (4.4)$$

where E_{laser} is the photon energy, D_0 the I-Cl bond energy, E_{int} the energy of internal degrees of freedom (I^* excitation), m_{Xe} the mass of Xe, and n the number of Xe atoms in the cluster. As the number n of Xe atoms in the cluster increases, the mass factor in Eq. 4.4 converges to 1 and the KER of the outgoing Cl photofragments increases, which explains the shift of the peak to higher kinetic energy. To evaluate the contribution of each cluster to the fast peak, we subtracted the exponential part $A_1 \exp(-B_1 E)$ accounting for the cage effect from the overall KER distribution. We fit the remainder with one broad Gaussian (peaking at 1.5 eV) accounting for subtraction imperfections and additional Gaussians (10 proved to be sufficient) of common width, each peaking at the energies calculated with Eq. 4.4. The result is shown in Figure 4.5. The best fit is obtained when assuming a mass distribution with 32% of ICl in the form of free monomer molecules, another 47% of ICl molecules form Xe-ICl clusters and the remaining 21% of ICl molecules from higher order clusters ($n = 2-9$). Note that although individually they have small contributions, the inclusion of higher order clusters is necessary in order to improve the fit quality on the fast side of the peak.

One can note several imperfections in the model: The Xe-I bond energy, which would shift KER lower, was not taken into account. Also, a certain amount of the energy that is available after photodissociation is consumed during the Xe cluster evaporation process. In addition, some energy is deposited in vibrational modes of the $\text{Xe}_n \cdot \cdot \cdot \text{I}$ fragment. Finally one could include clusters with additional ICl molecules either inside or on the surface of the cluster. Therefore, the above numbers for cluster distributions are only an approximation, aiming to show that the proposition of photolysis of cluster-surface-bound ICl can actually interpret our fast-peak data.

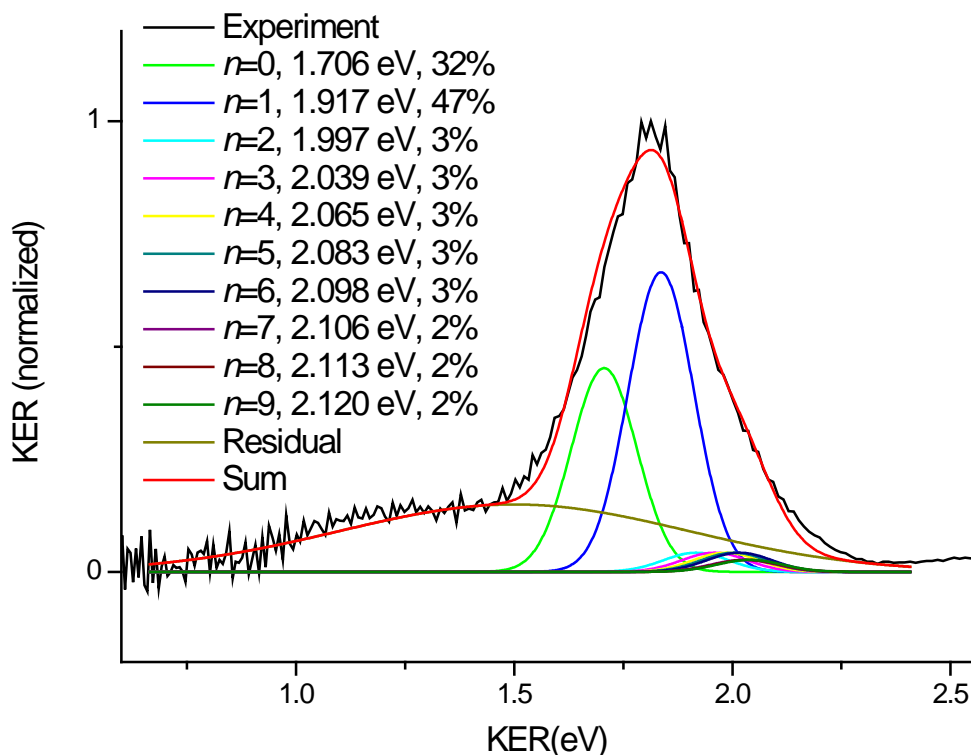


Figure 4.5. Speed Gaussian fit to the KER distribution of the Cl-photofragments. In the legend, n denotes the number of Xe atoms in the cluster, the second number the peak position in eV, and the percentage the contribution of each peak (cluster) to the total peak area without counting the residual peak (the broad peak at 1.5 eV).

Based on the above discussion, the Cl and Cl* data point to the existence of two cluster types: cage-like clusters where one or more ICl molecules are surrounded by Xe atoms and relatively small clusters with ICl molecule(s) on the surface where I is bound to the Xe atoms of the cluster. High level theoretical calculations should be able to confirm or disprove this conclusion. An alternative explanation may involve pure ICl clusters of a broad cluster size distribution. In the small clusters, essentially all the molecules reside on the surface and Cl atom can escape directly after the photodissociation without losing its kinetic energy in the collisions with the cluster constituents. This would yield the faster fragments since the Cl departs against the cluster mass analogically to the ICl-Xe $_n$ case. Again, the fast peak would be a sum of weighted shifted peaks calculated for (ICl) $_n$, $n = 0, \dots, \infty$ (the contribution from the very large

clusters would decrease and the shifting in energy would be negligible). The statistical distribution would then correspond to the Cl fragments originating from the interior of those $(\text{ICl})_n$ clusters that are large enough so that Cl could undergo the caging. We consider the $(\text{ICl})_n$ cluster case to be a weaker explanation of our results since it requires building of sufficiently large $(\text{ICl})_n$ clusters, which seems unlikely in view of the relatively low concentration of our ICl vapor in Xe. Calculating the mean Xe_n cluster size using the famous Hagedorn's formula³ for our experimental conditions, we obtain $n \approx 400$ for pure Xe expansion and assuming full opening of the valve in the middle of the gas pulse.³ Thus, we propose the more likely alternative to be the generation of xenon clusters with some ICl molecules, leading to mixed $\text{ICl}\cdot\text{Xe}_n$ or $(\text{ICl})_m\text{Xe}_n$ clusters.

4.4.2. I and I* photofragments

When it comes to I and I* distributions, Figures 4.2 and 4.3 and comparisons to Cl/Cl* fragments are extremely illuminating. The change in iodine fragment distribution from He to Xe expansion is more drastic than that of chlorine fragments and no rings are clearly visible. In addition, the angular distribution from monomers to clusters changes significantly. This is more evident in the case of $\text{I}(^2P_{3/2})$ (Figure 4.3 panels (a) and (b)), where the perpendicular angular distribution in He becomes parallel in Xe. Both the angular and KER distributions for the I and I* in Xe expansion are rather similar. Thus, the first conclusion one can draw is that the effect of Xe is more dramatic for iodine fragments, therefore, Xe should interact more with the iodine rather than the chlorine in the ICl. We shall use the two cluster types (cage-like and ICl-on-surface) proposed earlier for Cl/Cl* data to rationalize the I/I* observations as well. The lack of I/I* fast peaks matching the Cl/Cl* fast peaks at 1.81 eV, 2.55 eV, and 2.5 eV can be explained by the stereo-dynamics in the case of the clusters with surface-mounted ICl. If the ICl molecule preferably attaches (anchors) to Xe-cluster moiety, exclusively via the I atom, then upon “impulsive” photodissociation, the iodine photofragment would always be directed to and colliding with the Xe cluster, thus, losing kinetic energy. Therefore, no “direct”, fast distinct peaks would be observed for iodine photofragments. The broad iodine KER distribution features can be explained by cage-like clusters. Iodine KER values slower than that expected for the

monomer, can be explained by the *delayed cage exit* and the *cage effect* similarly to chlorine fragments above. However, distributions in Figures 4.2(c) and 4.2(d) include I/I* fragments with significantly higher KER than what would correspond to monomer dissociation, reaching 2.5 eV. Such faster-than-expected fragments have been observed and rationalized previously for acetylene in various clusters including Xe-clusters.^{13,14} The faster fragments were generated by multiphoton processes due to the cage effect: acetylene molecule was prevented to dissociate in the cluster and quenched to a vibrationally excited ground electronic state from which it was dissociated by the next photon yielding the fragment with a kinetic energy increased by the vibrational excitation. It is worth noting that essentially the same effect was observed also upon dissociation of HBr in rare gas clusters, where it however resulted in a well resolved additional ring at higher energies in the images.³ In the present case, caging to vibrationally excited ICl is possible but rather unlikely since it would also yield much faster Cl fragments than those observed. Another possible scenario would be generation of XeI molecule or XenI cluster upon ICl dissociation in the cluster and subsequent Xe-I dissociation in multiphoton process which would yield the faster I fragments. The formation of the Xe_nI would be consistent with the surface mounted ICl argument above, and the fact that we see no evidence for similar XeCl species generation further favors our suggestion that the ICl preferably anchors to the surface of the Xe_n cluster almost exclusively via the I-atom.

4.5. Conclusion

In this paper we present the dramatic effects that even a noble seed gas like Xe can have on the photochemistry of a relatively simple diatomic molecule like ICl. In ICl photolysis in molecular beam of He and Xe seed gases, we observe broadening of the monomer peaks, which is more severe in the case of I and I* where even angular distributions are changing from perpendicular to parallel. The KER of Cl and Cl* increases in Xe compared to that in He. We explain these observations based on formation of two cluster types: a cage-like type where one or more ICl molecules are embedded in Xe and another type where small clusters of Xe or Xe-ICl cores feature an ICl molecule on the surface. Although many open questions remain about the actual mechanism of the observed effects, the experimental evidence is solid and well interpreted

by the rather qualitative models of cluster dissociation proposed. A more detailed insight into the photodissociation dynamics in the present clusters requires high level theoretical treatment, which goes beyond the present purely experimental paper. Yet one of the contributions of the present work is to stimulate such theory to treat these exciting problems of molecule photochemistry in confined cluster environments. Our present results continue the effort to understand clustering effects on molecular photochemistry. These effects have now been observed in a number of systems extending from diatomic to polyatomic molecules and need additional experimental and theoretical work to be understood in detail.

References

- ¹ L. Rubio-Lago, D. Zaouris, Y. Sakellariou, D. Sofikitis, T. N. Kitsopoulos, F. Wang, X. Yang, B. Cronin, A. L. Devine, G. A. King, M. G. D. Nix, M. N. R. Ashfold, and S. S. Xantheas, “Photofragment slice imaging studies of pyrrole and the Xe...pyrrole cluster”, *J. Chem. Phys.* **127**, 064306 (2007).
- ² M. L. Lipciuc, F. Wang, X. Yang, T. N. Kitsopoulos, G. S. Fanourgakis, and S. S. Xantheas, “Cluster-controlled photofragmentation: The case of the Xe-pyrrole cluster”, *ChemPhysChem* **9**, 1838 (2008).
- ³ J. Fedor, J. Kočišek, V. Poterya, O. Votava, A. Pysanenko, M. L. Lipciuc, T. N. Kitsopoulos, and M. Fárník, “Velocity map imaging of HBr photodissociation in large rare gas clusters”, *J. Chem. Phys.* **134**, 154303 (2011).
- ⁴ U. Buck, “Photodissociation of hydrogen halide molecules in different cluster environments”, *J. Phys. Chem. A* **106**, 10049 (2002).
- ⁵ M. S. Child and R. B. Bernstein, “Diatomic interhalogens: Systematics and implications of spectroscopic interatomic potentials and curve crossings”, *J. Chem. Phys.* **59**, 5916 (1973).
- ⁶ D. J. Seery and D. Britton, “The continuous absorption spectra of chlorine, bromine, bromine chloride, iodine chloride, and iodine bromide”, *J. Phys. Chem.* **68**, 2263 (1964).
- ⁷ S. Yabushita, “Potential energy curves of ICl and non-adiabatic interactions studied by the spin-orbit CI method”, *J. Mol. Struct.: THEOCHEM* **461–462**, 523 (1999).
- ⁸ N. Diamantopoulou, A. Kartakoulis, P. Glodic, T. N. Kitsopoulos, and P. C. Samartzis, “Ultraviolet photodissociation of iodine monochloride (ICl) at 235, 250, and 265 nm”, *J. Chem. Phys.* **134**, 194314 (2011).
- ⁹ K. Tonokura, Y. Matsumi, M. Kawasaki, H. L. Kim, S. Yabushita, S. Fujimura, and K. Saito, “Photodissociation of ICl at 235–248 nm”, *J. Chem. Phys.* **99**, 3461 (1993).
- ¹⁰ L. J. Rogers, M. N. R. Ashfold, Y. Matsumi, M. Kawasaki, and B. J. Whitaker, “The photodissociation of iodine monochloride at 235 nm”, *Chem. Phys. Lett.* **258**, 159 (1996).
- ¹¹ C.-K. Ni and G. W. Flynn, “State and velocity distributions of Cl atoms produced in the photodissociation of ICl at 237 nm”, *Chem. Phys. Lett.* **210**, 333 (1993).
- ¹² G. Herzberg, *Molecular Spectra and Molecular Structure, Vol. I, Spectra of Diatomic Molecules* (Van Nostrand Reinhold, New York, 1950).

¹³ M. Fárník, V. Poterya, O. Votava, M. Ončák, P. Slaviček, and U. Buck, “Solvent-induced photostability of acetylene molecules in clusters probed by multiphoton dissociation”, *J. Phys. Chem. A* **113**, 7322 (2009).

¹⁴ M. Fárník, V. Poterya, J. Kočíšek, and P. Slaviček, “Short review on the acetylene photochemistry in clusters: photofragment caging and reactivity”, *Mol. Phys.* **110**, 2817 (2012).

Chapter V

Collision-induced dissociation of Nb_xO_y^+ ($x = 1, 2, y = 2-12$) clusters: crossed molecular beams and collision cell studies

5.1 Introduction

Niobium oxides have been found to exhibit outstanding catalytic properties. They find application in the petrochemical industry, as a support material in metallic or oxide catalysts for selective hydrocarbon oxidation, and in NO_x conversion for pollution control.^{1,2,3} These applications triggered a series of studies on the preparation, molecular structure–reactivity relation, and their catalytic behavior.⁴⁻⁸ It was concluded that the catalytic activity of the niobium oxide surface is dependent on the preparation process with the active species being a photo-excited Nb=O bond dispersed on the catalyst surface.

A complete understanding of the formation mechanism of these surface oxides and the relationship between the structure and reactivity still has not been achieved, due to the complexity of coordination sites in terms of stoichiometries and phase structures present on niobium oxide surfaces. Various surface experimental techniques that provide information on the atomic structure and composition of surfaces often show limited abilities to directly probe structure-reactivity relationships. As an approach to overcoming the difficulty of surface inhomogeneity, studies on gas phase clusters can provide insights in the physical and chemical properties of catalytic surfaces. A few studies have been conducted on free gas phase niobium

oxide clusters, with the aim of modeling isolated active sites present on niobium oxide catalysts. These investigations started with studies on gas phase reactions of some small niobium oxide anions⁹ and cations¹⁰ and continued later with studies on chemistry of reactions of anionic and cationic niobium oxide clusters.¹¹⁻¹³

In order to understand the chemical reactivity, the knowledge of the structure and the stability of the clusters is crucial. Related to this, Castleman et al.¹³ have studied the properties of cationic niobium oxide clusters. Based on their experiments on CID, they found the building blocks and the corresponding cluster stoichiometry of the most stable species. Motivated by the results from these CID experiments, Sambrano et al.¹⁴ have presented a DFT study for neutral Nb_xO_y and cation Nb_xO_y^+ clusters, providing a complementary theoretical study of geometric, thermodynamic, and electronic properties. Furthermore, extensive studies on cluster structures have also been done using infrared multiple photon dissociation (IR-MPD)¹⁵ and UV-Vis photofragmentation.¹⁶

In our laboratory, we have used photofragmentation spectroscopy and CID of mass-selected ions to study the stability and the structure of metal-doped noble gas clusters¹⁷ and metal oxide clusters.¹⁸⁻²¹ In a similar manner, in this contribution we study the positively charged Nb oxide clusters by time-of-flight mass spectrometry and collisions with noble gas atoms. We measure the clusters' fragmentation cross section using our recent approach based on crossed molecular beams²¹ compared with the standard CID technique.^{13,20,22-24} The new experimental configuration, which uses a secondary molecular Ne beam crossing perpendicularly the primary cluster beam, and a retarding field energy analyzer (RFEA), is significantly faster and more efficient for obtaining fragmentation cross sections, without mass selection of the individual clusters. Furthermore, information on additional reaction channels (besides fragmentation) activated by cluster ion – atom energetic collisions (such as multi-ionization or Coulomb explosion) can be obtained.

5.2 Experimental apparatus and methods

5.2.1 Setup

The differentially pumped molecular beam apparatus used in these experiments has been described in detail previously.^{21,25-28} A molecular beam of niobium oxide clusters is generated in a source chamber by combining the laser ablation of a niobium target with a supersonic expansion of oxygen. The niobium oxide cluster cations are carried and cooled down in the supersonic expansion and subsequently pass through a 4-mm-diameter skimmer into a double-field TOF mass spectrometer that can be used either in linear configuration or as a reflectron assembly. The stability and the dynamics properties of the produced clusters have been investigated in detail using collision induced fragmentation

5.3 Results

5.3.1 Mass spectra

In Figure 5.1, we present mass spectra of the cationic niobium oxide clusters formed in our source, obtained in linear TOF configuration, with and without the secondary beam crossing (dashed and full line, respectively). Contrary to experiments using a pure He beam as carrier gas,³⁰ by adding O₂,^{13,31} or using pure O₂ as carrier gas in our case, no atomic ion (Nb⁺) or niobium monoxide (NbO⁺) are detected, due to their exothermic reactions with oxygen.^{32,33} The dominant production of cluster ions containing one metal atom is observed and discussed in several previous studies^{18,34} performed by our group. The configuration of our cluster source – without confining channels – limits the number of metal-metal collisions, necessary for the formation of clusters containing more than one metal atom. Nevertheless, small amounts of Nb₂O_y⁺ (y = 2–15) and Nb₃O_{7–9}⁺ were also detected.

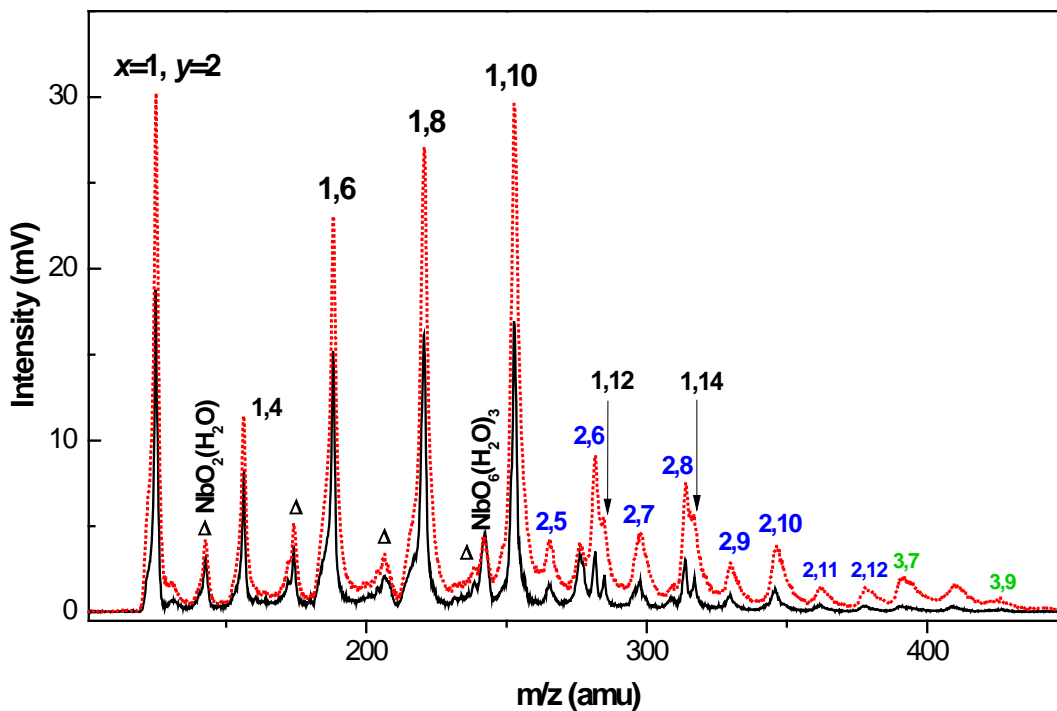


Figure 5.1. Mass spectra of niobium oxide clusters Nb_xO_y^+ obtained at $V_{\text{grid}} \approx 0$, with beam crossing (dashed line) and without beam crossing (solid line). The Δ indicates the hydrated clusters (see text for details).

The NbO_y^+ series consists mostly of clusters with an even number of oxygen atoms. The absence of clusters with an odd number of O atoms differs from earlier studies^{13,15,35} where both even- and odd-numbered clusters were formed. A similar odd-even alternation is noticed for Nb_2O_y^+ cluster series, but not as prominent as in the case of NbO_y^+ clusters. The use of pure O_2 reacting with the Nb ablation plume leads to the formation of clusters very rich in oxygen.³⁶⁻³⁸ Although not so strong, this effect is also seen in the distribution of Nb_2O_y^+ clusters, where, Nb_2O_6^+ cluster is the most intense of the series. Additionally, hydrated clusters (marked by triangles in Figure 5.1), with the general formula $\text{NbO}_y(\text{H}_2\text{O})_w^+$ ($y = 2, 4, 6, 8, w = 1, 3$) were generated from water impurities present in the gas inlet system.

5.3.2 Fragmentation channels

Another striking feature in Figure 5.1 is an important intensity increase in all peaks when the secondary beam is on. Considering all the possible outcomes of cluster ion-atom collisions (Equations 1.29–1.34), this increase can be attributed to energetic neutral fragments (Equations 1.31–1.33) and/or to the creation of additional charged species by Coulomb explosion (Equations 1.34). This second possibility will be discussed later.

The newly formed ionic species can be separated from the nonfragmented parent (one by one) by gradually increasing the RFEA voltages (V_{grid}) and measuring the decrease in the signal for each particular cluster as already mentioned in Section 2.2.2. The signal's evolution with increasing V_{grid} between 0 V and ~2000 V ($V_{\text{grid}} \gg V_{\text{acc}}$) is shown in Figure 5.2 for two cluster ions, NbO_8^+ and NbO_{10}^+ .

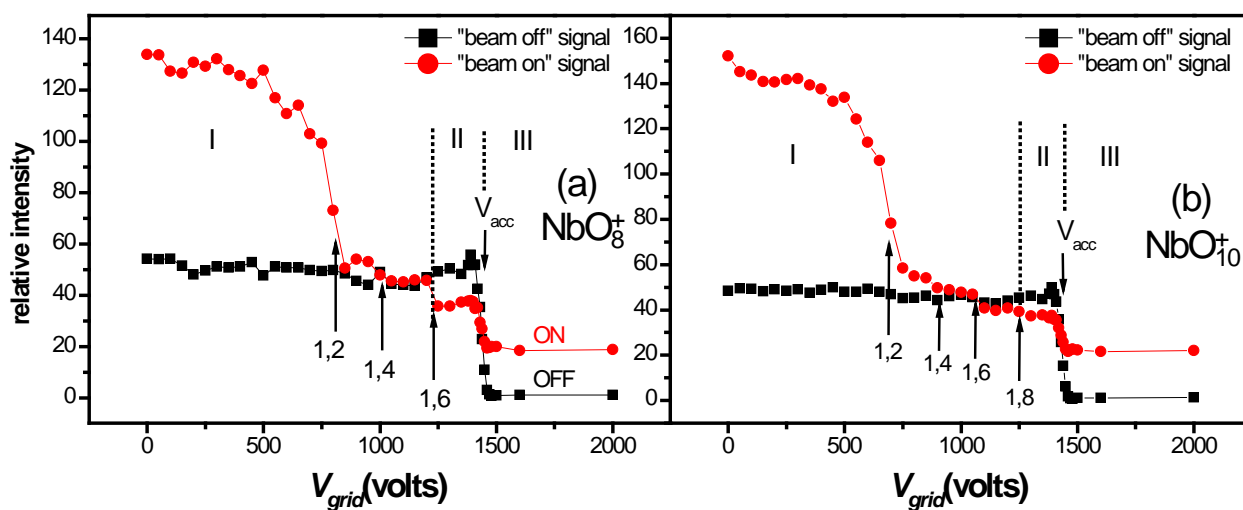


Figure 5.2. The fragmentation of the NbO_8^+ (a) and NbO_{10}^+ (b) clusters. The arrows with the labels indicate the kinetic energy and the size of the corresponding fragments.

The determination of fragments' masses, as described in the Section 1.2.6, indicate that NbO_y^+ clusters dissociate *via* loss of one or more O_2 molecules (or pairs of oxygen atoms).

The fragmentation pathways for the NbO_y^+ clusters are also investigated with the conventional gas cell experimental configuration, described in Section 2.2.1. In investigations using a reflectron, similar results were obtained for all NbO_y^+ clusters, and we present in Figure 5.3 only the cases of NbO_8^+ as a representative example (collision partner Kr, collision energy in the center-of-mass frame, $E_{\text{CM}} = 275$ eV).

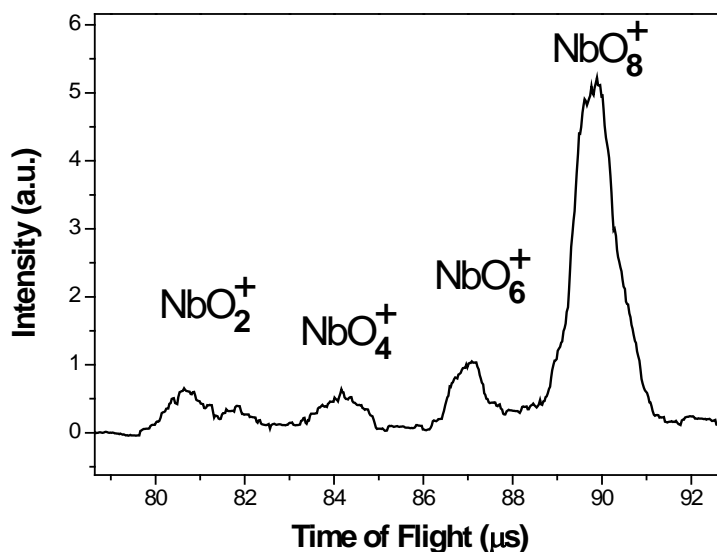


Figure 5.3. Reflectron TOF spectrum of the mass-selected NbO_8^+ cluster, showing the fragments formed after collisions with Kr atoms in beam-gas cell arrangement.

Both methods clearly indicate similar fragmentation patterns, showing the loss of one or more O_2 molecules. The mass of the neutrals cannot be directly measured, but is calculated as the difference between the masses of the parent and the observed ionic fragments; therefore the form of oxygen fragments (atomic or molecular) is undetermined. Loss of groups of two O-atoms or, more likely, molecular oxygen is one of the fragmentation channels of larger Nb_xO_y clusters for highly energetic collisions¹³ and the main photofragmentation channel for oxygen-rich Nb_2O_y^+ clusters.¹⁶ In our group, it has also been previously observed for $\text{Fe}(\text{O}_2)_n^+$ ($n = 1-6$) clusters.^{21,34}

The loss of oxygen is also observed for clusters containing two Nb atoms. In Figure 5.4, we present the intensity of Nb_2O_8^+ cluster, as a function of the V_{grid} before and after secondary beam crossing and we indicate in the figure by arrows and labels the kinetic energy and the size x,y of the expected fragments, respectively.

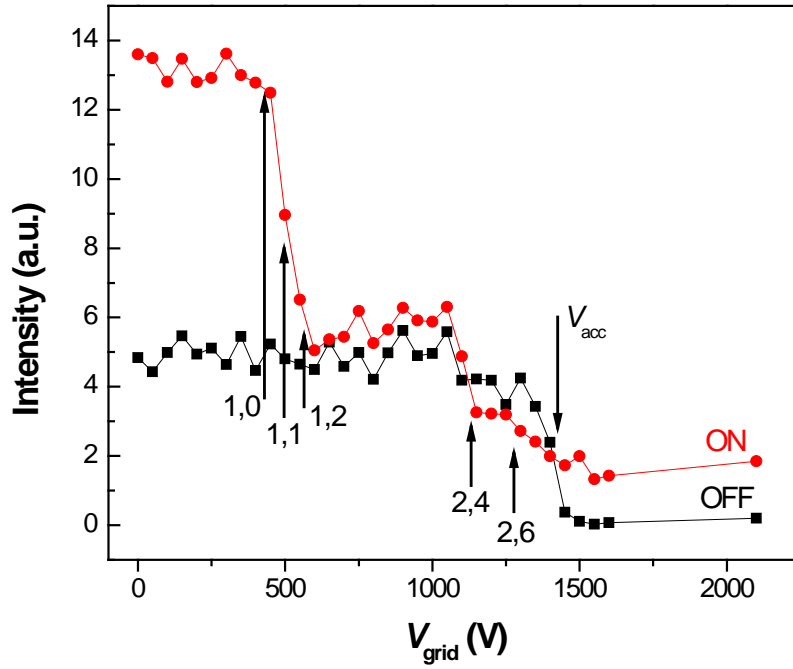


Figure 5.4. The fragmentation of the Nb_2O_8^+ cluster.

5.3.3 Collision cross section measurements

As analyzed before in Section 2.2.2, the fragmentation cross section Q for an individual cluster is determined using Equation 5.1. In particular, for the Nb_xO_y^+ clusters in collisions with Ne atoms with an acceleration potential of 1500 V we use:

$$Q = -\frac{1}{NL} \ln \left(\frac{I_{V_{\text{grid}}=1400}^{\text{ON}} - I_{V_{\text{grid}}=2000}^{\text{ON}}}{I_{V_{\text{grid}}=1400}^{\text{OFF}} - I_{V_{\text{grid}}=2000}^{\text{OFF}}} \right) \quad (5.1).$$

In Figure 5.5 we plot the QNL values obtained from the crossed beam (CB) fragmentation of NbO_y^+ clusters as a function of the number of oxygen atoms y , for three values of the

laboratory collision energy (500, 1500 and 1800 eV). For comparison, Figure 5.5 also shows the QNL results (circles) obtained using the conventional beam-gas cell (BG) configuration, at $E_{\text{Lab}}=1500$ eV. The data sets were normalized to each other using the least square method. Some representative error bars ($\sim 20\%$) (due mainly to the reproducibility of the data) are also shown in the figure. The CB and BG results are in good agreement showing a similar trend of increasing cross section with increasing y for NbO_y^+ ($y = 4, 6, 8$) clusters, as predicted by the quasi-spherical cluster model.³⁹ As notable exception, for NbO_{10}^+ the fragmentation cross section is equal or smaller than for NbO_8^+ . A similar situation was observed for iron oxide clusters^{21,34} and it was explained by an increased stability of FeO_{10}^+ , as proven by the corresponding mass spectra and the DFT calculations. In the same way, in the present case, the mass spectrum of niobium oxide clusters supports this assumption showing an intense peak for NbO_{10}^+ , followed by an important signal decrease for the next clusters of the series.

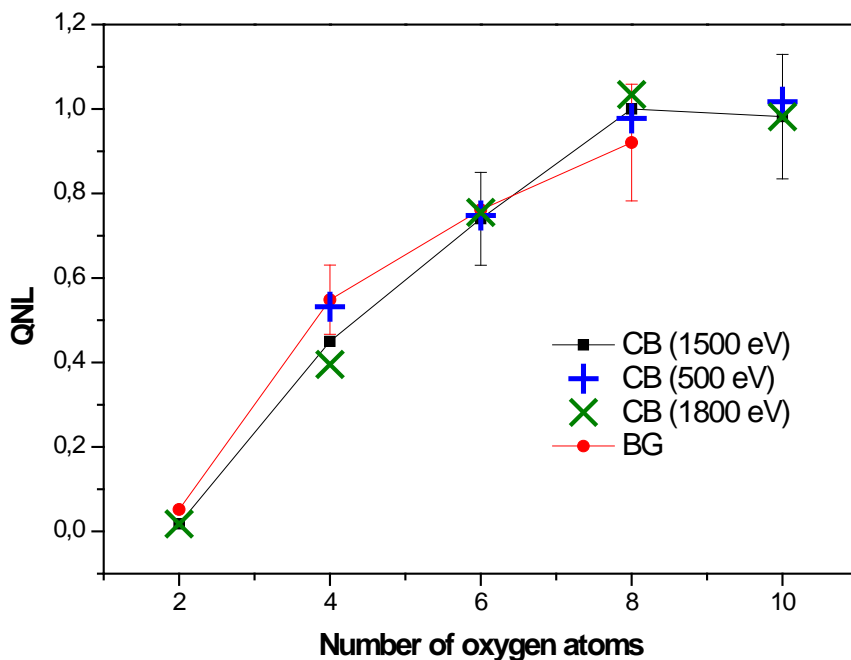


Figure 5.5. Fragmentation cross sections of NbO_y^+ clusters. The values were obtained from the crossed beam (CB) experiments with secondary Ne beam at different laboratory collision energies (■ 1500 eV, × 1800 eV, + 500 eV) and the beam-gas cell (BG) experiments using Kr as the collision gas (●) at 1500 eV collision energy.

The fragmentation cross section is the lower limit and in certain conditions represents a good approximation of the total collision cross section.²¹ Under these circumstances, the evolution of the fragmentation cross section as a function of cluster size should be independent of the collision energy. In order to prove this, cross section measurements of NbO_y^+ clusters were performed for three different values of kinetic energy in the laboratory frame of reference E_{Lab} at 500 eV, 1500 eV and 1800 eV. The results are very similar and can be explained by the fact that even at the lowest E_{Lab} investigated here (500 eV), the collision energy is high enough (E_{CM} ranges from 37 eV for NbO_{10}^+ to 70 eV in the case of NbO_2^+) and every collision leads to cluster fragmentation.

This is also the case for the beam-gas cell experiments, performed with Kr as a collision partner. The larger mass of Kr ($m = 84$), as compared to Ne ($m = 20$), makes that for similar laboratory energies, the center of mass collision energy is higher. Moreover, increasing the E_{CM} by increasing the accelerating potential to 1800 V (up to 248 eV for NbO_2^+ in collision with Ne) did not lead to the appearance of new (high energy activated) fragmentation channels.

In our previous work on iron oxide clusters,^{21,34} the equivalence between the fragmentation cross section and the total collision cross section at high collision energies has been proved by comparing the experimental results with the calculated geometrical cross sections for theoretical structures. To the best of our knowledge, such structures are not available for the (quite uncommon) oxygen-rich clusters containing one niobium atom (ion) reported here. We noticed, however, some similarities between the experimental results (compare mass spectra and *QNL* measurements from this paper with Refs. 21, 34) obtained for niobium and iron oxides clusters, like the prevalence of clusters containing an even number of oxygen atoms and the stability of clusters with 10 oxygen atoms followed by a sudden decrease in the intensity for larger clusters. Similar evolution is noticed also in the case of the fragmentation cross sections of the two series: a linear increase with the size, with the small decrease for MO_{10} clusters ($M = \text{Nb}$ or Fe). These similarities encouraged us to assume similar geometries for niobium oxide and iron oxide clusters. In addition, we approximated the length of different bonds between the constituent atoms from structures reported in the literature for larger niobium oxide clusters (containing more than 1 Nb atom)^{14,40,41}. We considered the distance between Nb and O to be 1.9

and 1.75 Å, for a single bond and double bond, respectively, and the length of O–O bond to be 1.3 Å. By rescaling the iron oxide clusters structures reported in Ref. 42 to the bond lengths mentioned earlier, we determined some probable geometries for the NbO_y^+ clusters studied here.

In Figure 5.6 we compare the fragmentation cross section measured in the crossed beam experimental configuration and the geometrical cross sections determined by applying the projection model to structures considered as most probable for O-rich NbO_y^+ clusters.

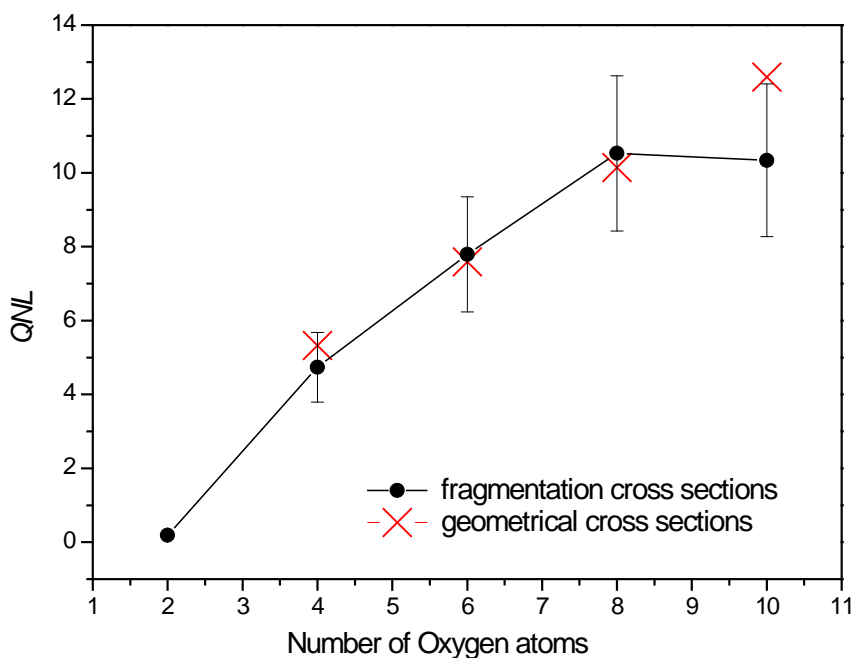


Figure 5.6. Comparison of experimentally determined fragmentation cross sections (CB experiments at collision energy 1500 eV), and calculated geometrical cross section for NbO_y^+ clusters.

As in the case of iron oxide clusters, a good correspondence is observed between most of the experimental and theoretical values. The only discrepancy, observed for NbO_{10}^+ can be explained (like for FeO_y^+) by the fact that in theory we calculate the geometrical cross section, which is only approximated with the fragmentation cross section determined experimentally ($Q_{\text{geom}} \geq Q_{\text{frag}}$). This effect is evident also for the thermodynamically stable NbO_2^+ : its fragmentation cross section as measured by our method is very small, close to zero in the error limits.

Cross section determination using the crossed beam configuration does not require prior mass separation of individual clusters. In this way, even clusters with a low abundance can be measured. As already mentioned, in our source, clusters with more than one metal atom are scarcely formed (see Figure 5.1), but their intensity is enough to allow cross beam measurements. In Figure 5.7 we plot the results (squares) for the fragmentation cross section of Nb_2O_y^+ clusters as a function of the number of the oxygen atoms y at $E_{\text{Lab}}=1500$ eV.

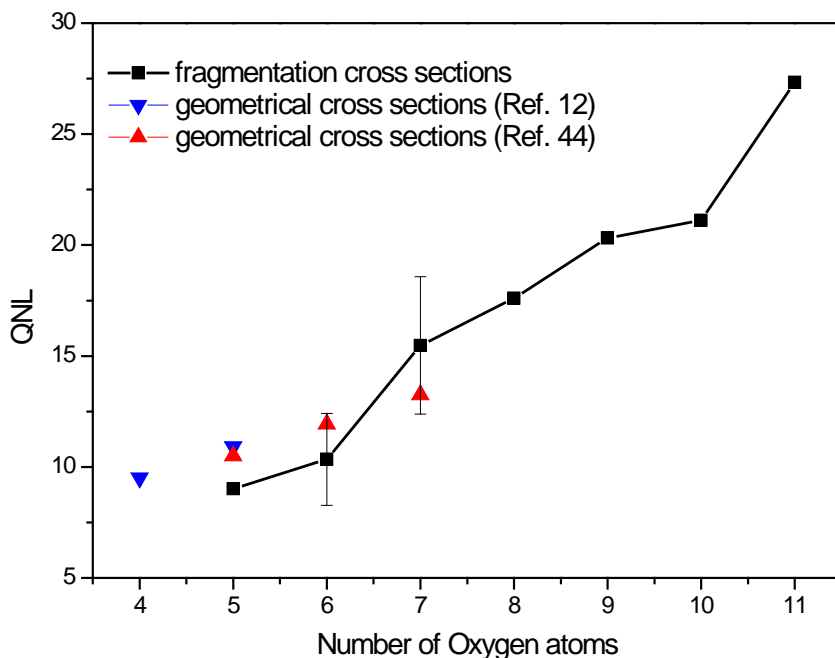


Figure 5.7. Nb_2O_y^+ clusters fragmentation cross sections obtained from the crossed beam experiments at $E_{\text{Lab}}=1500$ eV and the calculated geometrical cross section for structures from Refs. 14 and 41.

As expected, the general trend of the increasing cross section with the cluster size is observed. Furthermore, it is worth noticing that the fragmentation cross sections reflect also the stability of the clusters, so that the local minima in the cross section indicate higher stability of the respective clusters. This is in accordance to the mass spectra of figure where the stability of the same clusters appears as peaks with higher intensity. As previously observed for NbO_{10}^+ , in this case Nb_2O_6^+ , Nb_2O_8^+ and $\text{Nb}_2\text{O}_{10}^+$ seem to be more stable in comparison to their neighbors.

Several authors^{14,40,41} reported calculations of low energy structures for Nb₂O_y clusters (neutrals and/or ions). For the Nb₂O₄ and Nb₂O₅¹⁴, the differences between the neutral and cationic structures are insignificant; they have the same geometries, only the bond lengths are slightly different. This allows us to use the neutral geometries reported by Zhai *et al.*⁴¹ as an approximation for larger clusters' structures and we used the projection model to determine their geometrical cross section. The calculated values (triangles) agree with the experimentally determined fragmentation cross sections in the limit of the experimental errors. Theoretical calculations are necessary for larger clusters in order to have a more thorough comparison.

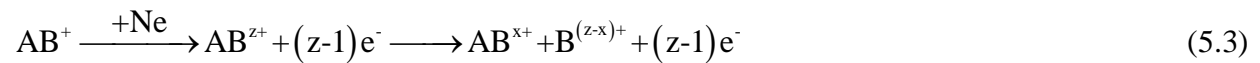
5.3.4 Collisional multiionization

If the outcome from a collision between a cluster ion (AB⁺) and an atom (X) is the fragmentation



then the intensity of parents (AB⁺) and the ionic fragments (A⁺) varies with V_{grid} as presented in Figure 2.5 In the case of NbO_y⁺ clusters, B would correspond to an undetermined number of neutral oxygen molecules or atoms produced by fragmentation. It is assumed that for V_{grid} ≈ 0, the intensity difference between “beam on” and “beam off” is exclusively due to the neutral fragments (B). The amount of these neutrals can be measured when V_{grid} ≫ V_{acc} with the secondary beam “on” (the charged species are rejected and only neutrals are detected).

However, this is not the case for the experimental data shown in Figure 5.2, where the high intensity of clusters at V_{grid} ≈ 0 after the interaction with the secondary beam exceeds the amount of the neutrals and thus, clearly indicates the appearance of new ions. Additional charges can be formed from one ion by Coulomb explosion of a multiply charged cluster, as indicated in the Equation 5.3.



The first ionization potentials of both molecular ($IP(\text{O}_2)=12.07$ eV) and atomic ($IP(\text{O I})=13.6$ eV)⁴³ are smaller than the second ionization potential of niobium ($IP(\text{Nb II}) = 14.32$ eV),⁴⁴ so no stable Nb^{2+}O_y clusters are expected to be formed. Instead, the second charge will appear on one of the O atoms and because the cluster is not big enough to compensate the Coulombic repulsion by charge separation, a positively charged fragment will be ejected. It is well known that multiply charged clusters are observed only above a critical size (appearance size); for example pure Nb_n^{2+} clusters have been detected only for $n \geq 9$.⁴⁴ For a discussion on charge delocalization dynamics on metal clusters and metal oxide clusters see Refs. 45,46.

The ratio of charged particles formed following collisional activation (CE) to the initial parents is noted $(I_0 + CE)/I_0$ and can be determined from the cluster's intensity measured at $V_{\text{grid}} \approx 0$, where all the fragments are detected (region I in Figure 5.2), using the formula:

$$\frac{I_0 + CE}{I_0} = \frac{I_{\text{I}}^{\text{ON}} - I_{\text{III}}^{\text{ON}}}{I_{\text{I}}^{\text{OFF}} - I_{\text{III}}^{\text{OFF}}}, \quad (5.4)$$

where I_0 is the intensity of the parent and CE represents additional ions formed by Coulomb explosion. I_{I}^{ON} , $I_{\text{III}}^{\text{ON}}$, $I_{\text{I}}^{\text{OFF}}$ and $I_{\text{III}}^{\text{OFF}}$ are the intensities measured in regions I and III for “beam on” and “beam off” respectively. In Table 5.1 we present the values obtained for NbO_y^+ clusters at three different acceleration energies.

Table 5.1 Ratio of ions detected after collisions to the initial parent ions at different acceleration energies.

Cluster ion	$V_{\text{acc}} = 500$ V	$V_{\text{acc}} = 1500$ V	$V_{\text{acc}} = 1800$ V
NbO_4^+	1.14	1.36	1.94
NbO_6^+	1.25	1.82	2.20
NbO_8^+	1.31	2.21	2.42
NbO_{10}^+	1.35	2.52	2.50

Values of the ratio superior to 1 prove the formation of new charges by Coulomb explosion in all studied cases, for example 14% of supplementary charges formed from NbO_4^+ . The ratio superior to 2 indicates at least one channel leading to the appearance of two or more new charges. For the clusters considered, the fraction of newly formed ions to the initial parents is increasing with the cluster size, indicating the loss of more ionic fragments from larger clusters.

For any particular cluster, the increase of acceleration energy promotes the formation of more charged fragments. This can be explained by the fact that at higher collision energy, more energy is transferred to the cluster electronic excitations, possibly removing many electrons and resulting in the formation of higher z multiple charged ions that will produce more fragment ions. A thorough study of the extent of Coulomb explosion for various (high) collision energies, feasible using our technique, would give information on the parent cluster's energetic states and multiionization phenomena.

5.4 Conclusions

In this paper, we present the formation and fragmentation of Nb_xO_y^+ clusters ($x = 1-2$, $y = 2-12$) after collision with noble gases. The open configuration of our cluster source, combined with the use of a high oxygen content beam for the clusters formation, leads to the apparition of small, oxygen-rich aggregates whose O/Nb ratio is very different from the stoichiometry of the common niobium oxides. We also measured the collision cross sections of those clusters. The results are based on the fragmentation cross sections, obtained following collision induced dissociation.

Without precisely measuring the N (the number density of the collision partner) and L (the length of the interaction region between clusters and noble gas), the absolute value cannot be determined, but the evolution of measured cross section with the cluster's size (number of atoms) is representative and could be used for validating structures obtained by *ab initio* calculations, as we have recently shown.²¹

While the conventional CID studies using a reflectron are limited (by ion optics) to the detection of fragments with molecular masses close to the parents', the linear configuration used

in our new approach allows the efficient detection of ions (and neutrals!) in a larger mass range. Therefore, the new experimental configuration allows detecting and quantifying the Coulomb explosion of small clusters, opening the way to new studies.

References

- ¹ I. E. Wachs, L. E. Briand, J.-M. Jehng, L. Burcham, and X. Gao, “Molecular structure and reactivity of the group V metal oxides”, *Catal. Today* **57**, 323 (2000).
- ² E. I. Ko, J. M. Hupp, F. H. Rogan, and N. J. Wagner, “Preparation, reduction, and chemisorption behavior of niobia-supported nickel catalysts”, *J. Catal.* **84**, 85 (1983).
- ³ T. Ushikubo, “Recent topics of research and development of catalysis by niobium and tantalum oxides”, *Catal. Today* **57**, 331 (2000).
- ⁴ J.-M. Jehng and I. E. Wachs, “The molecular structures and reactivity of supported niobium oxide catalysts”, *Catal. Today* **8**, 37 (1990).
- ⁵ S. Yoshida, Y. Nishimura, T. Tanaka, H. Kanai, and T. Funabiki, “The local structures and photo-catalytic activity of supported niobium oxide catalysts”, *Catal. Today* **8**, 67 (1990).
- ⁶ A. Morikawa and A. Togashi, “Stability of niobium oxide catalyst activity emerging in reductive medium”, *Catal. Today* **16**, 333 (1993).
- ⁷ Y. Zhao, X. Zhou, L. Ye, S.C.E. Tsang, *Nano Rev.* **3**, 17631 (2012).
- ⁸ A. Borgschulte, J.H. Rector, B. Dam, R. Griessen, A. Züttel, *J.Catal* **235**, 353 (2005).
- ⁹ S. W. Sigsworth and A. W. Castleman, Jr., “Reaction of Group V and VI transition metal oxide and oxyhydroxide anions with oxygen, water, and hydrogen chloride”, *J. Am. Chem. Soc.* **114**, 10471 (1992).
- ¹⁰ M. R. Sievers and P. B. Armentrout, “Gas phase activation of carbon dioxide by niobium and niobium monoxide cations”, *Int. J. Mass Spectrom.* **179-180**, 103 (1998).
- ¹¹ P. Jackson, K. J. Fisher, and G. D. Willett, “Some reactions and thermochemistry of NbO_3^- : oxidation and reduction, hydrogen bond strength, and catalytic activation of primary alcohols”, *Int. J. Mass Spectrom.* **197**, 95 (2000).
- ¹² P. Jackson, K. J. Fisher, and G. D. Willett, “The catalytic activation of primary alcohols on niobium oxide surfaces unraveled: the gas phase reactions of Nb_xO_y^- clusters with methanol and ethanol”, *Chem. Phys.* **262**, 179 (2000).
- ¹³ H. T. Deng, K. P. Kerns, and A. W. Castleman, Jr., “Formation, structures, and reactivities of niobium oxide cluster ions”, *J. Phys. Chem.* **100**, 13386 (1996).

- ¹⁴ J. R. Sambrano, J. Andrés, A. Beltrán, F. Sensato, and E. Longo, “Theoretical study of the structure and stability of Nb_xO_y and Nb_xO_y^+ ($x = 1-3$; $y = 2-5, 7, 8$) clusters”, *Chem. Phys. Lett.* **287**, 620 (1998).
- ¹⁵ A. Fielicke, G. Meijer, and G. von Helden, “Infrared spectroscopy of niobium oxide cluster cations in a molecular beam: identifying the clusters structures”, *J. Am. Chem. Soc.* **125**, 3659 (2003).
- ¹⁶ K. S. Molek, T. D. Jaeger, and M. A. Duncan, “Photodissociation of vanadium, niobium and tantalum oxide cluster cations”, *J. Chem. Phys.* **123**, 144313/1 (2005).
- ¹⁷ G. S. Fanourgakis, S. C. Farantos, C. Lüder, M. Velegarakis, and S. S. Xantheas, “Optical absorption of Sr^+Ar_n ($n = 2-8$) clusters: Experiment and theory”, *J. Chem. Phys.* **109**, 108 (1998).
- ¹⁸ M. Velegarakis and A. Sfounis, “Formation and photodecomposition of cationic titanium oxide clusters”, *Appl. Phys. A* **97**, 765 (2009).
- ¹⁹ M. Jadrque, B. Sierra, A. Sfounis, and M. Velegarakis, “Photofragmentation of mass-selected titanium oxide cluster cations”, *Appl. Phys. B* **100**, 587 (2010).
- ²⁰ M. Velegarakis, M. Massaouti, and M. Jadrque, “Collision-induced dissociation studies on gas-phase titanium oxide cluster cations”, *Appl. Phys. A-Mater.* **108**, 127 (2012).
- ²¹ M. Velegarakis, C. Mihasan, and M. Jadrque, “Collision-induced dissociation studies on $\text{Fe}(\text{O}_2)_n^+$ ($n = 1-6$) clusters: application of a new technique based on crossed molecular beams”, *J. Phys. Chem. A* **117**, 2891 (2013).
- ²² W. Begemann, S. Dreihöfer, K. H. Meiwes-Broer, and H. O. Lutz, “Sputtered metal cluster ions: Unimolecular decomposition and collision induced fragmentation”, *Z. Phys. D* **3**, 183 (1986).
- ²³ G. von Helden, M.T. Hsu, N. Gotts, and M.T. Bowers, “Carbon cluster cations with up to 84 atoms: structures, formation mechanism, and reactivity”, *J. Phys. Chem.* **97**, 8182 (1993).
- ²⁴ M. F. Jarrold, “Drift Tube Studies of Atomic Clusters”, *J. Phys. Chem.* **99**, 11 (1995).
- ²⁵ C. Lüder and M. Velegarakis, “Photofragmentation spectrum of the Sr^+Ar complex”, *J. Chem. Phys.* **105**, 2167 (1996).

- ²⁶ C. Lüder, E. Georgiou, and M. Velegarakis, “Studies on the production and stability of large C_N^+ and $M_xR_N^+$ ($M = C, Si, Ge$ and $R = Ar, Kr$) clusters”, *Int. J. Mass Spect. Ion Proc.* **153**, 129 (1996).
- ²⁷ G.E. Froudakis, M. Muhlhauser, S.C. Farantos, A. Sfounis, and M. Velegarakis, “Mass spectra and Structures of Cu^+Rg_n clusters ($Rg = Ne, Ar$)”, *Chem. Phys.* **280**, 43 (2002).
- ²⁸ E. Witkowicz, H. Linnartz, C.A. de Lange, W. Ubachs, A. Sfounis, M. Massaouti, and M. Velegarakis, “Mass spectrometric and laser spectroscopic characterization of a supersonic planar plasma expansion”, *Intern. J. of Mass Spectrom.* **232**, 25 (2004).
- ²⁹ K. Athanassenas, D. Kreisle, B.A. Collings, D.M. Rayner, and P.A. Hackett, “Ionization potentials of niobium oxide clusters”, *Chem. Phys. Lett.* **213**, 105 (1993).
- ³⁰ P. P. Radi, G. von Helden, M. T. Hsu, P. R. Kemper, M. T. Bowers, “Thermal bimolecular reactions of size selected transition metal cluster ions: $Nb_n^+ + O_2$, $n = 1-6$ ”, *Int. J. Mass Spectrom. Ion Processes* **109**, 49 (1991).
- ³¹ F. Dong, S. Heinbuch, S. G. He, Y. Xie, J. J. Rocca, and E. R. Bernstein, “Formation and distribution of neutral vanadium, niobium, and tantalum oxide clusters: Single photon ionization at 26.5 eV”, *J. Chem. Phys.* **125**, 164318 (2006).
- ³² S. K. Loh, Li Lian, and P. B. Armentrout, “Oxidation reactions at variably sized transition metal centers: Fe_n^+ and $Nb_n^+ + O_2$ ($n = 1-3$)”, *J. Chem. Phys.* **91**, 6148 (1989).
- ³³ M. Chen, X. Wang, and Q. Qin, “Characterization of the products generated from laser ablation of Nb_2O_5 using matrix isolation FTIR spectroscopy”, *Appl. Surf. Sci.* **156**, 16 (2000).
- ³⁴ G. Mpourmpakis, M. Velegarakis, C. Mihean, and A. N. Andriotis, “Symmetry-switching molecular $Fe(O_2)_n^+$ clusters”, *J. Phys. Chem. A* **115**, 7456 (2011).
- ³⁵ K. A. Zemski, D. R. Justes, and A. W. Castleman Jr., “Studies of metal oxide clusters: elucidating reactive sites responsible for the activity of transition metal oxide catalysts”, *J. Phys. Chem. B* **106**, 6136 (2002).
- ³⁶ D. Prekas, C. Lüder, and M. Velegarakis, “Structural transitions in metal-ion-doped noble gas clusters: Experiments and molecular dynamics simulation”, *J. Chem. Phys.* **108**, 4450 (1998).

- ³⁷ M. Velegrakis, "Stability, structure and optical properties of metal ion-doped noble gas clusters", In *Advances in Metal and Semiconductor Clusters, Vol. V*, ed. M. A. Duncan (Elsevier, Amsterdam, 2001) p. 227.
- ³⁸ C. Lüder, D. Prekas, and M. Velegrakis, "Ion-size effects in the growth sequences of metal-iondoped noble gas clusters", *Laser Chem.* **17**, 109 (1997).
- ³⁹ P. Weis, "Structure determination of gaseous metal and semi-metal cluster ions by ion mobility spectrometry", *Int. J. Mass Spectrom.* **245**, 1 (2005).
- ⁴⁰ Y.X. Zhao, X.L. Ding, Y.P. Ma, Z.C. Wang, and S.G. He, "Transition metal oxide clusters with character of oxygen-centered radical: a DFT study", *Theor. Chem. Acc.* **127**, 449 (2010).
- ⁴¹ H.J. Zhai, X.H. Zhang, W.J. Chen, X. Huang, and L.S. Wang, "Stoichiometric and oxygen-rich $M_2O_n^-$ and M_2O_n ($M = Nb, Ta; n = 5-7$) clusters: molecular models for oxygen radicals, diradicals, and superoxides", *J. Am. Chem. Soc.* **133**, 3085 (2011).
- ⁴² C. Wang, J. Jian, G. Wang, Z.H. Li, and M. Zhou, "Infrared photodissociation spectroscopy of oxygen-rich $Fe(O_2)_n^+$ ($n = 3-5$) cation complexes", *J. Phys. Chem. A* **118**, 4519 (2014).
- ⁴³ H.M. Rosenstock, K. Draxl, B.W. Steiner, and J.T. Herron, "Ion Energetics Data" in NIST Chemistry WebBook, NIST Standard Reference Database Number 69, Eds. P.J. Linstrom and W.G. Mallard, National Institute of Standards and Technology, Gaithersburg MD, 20899, <http://webbook.nist.gov>, (retrieved September 18, 2013).
- ⁴⁴ N. Saito, K. Koyama, and M. Tanimoto, "Cluster generation by laser ablation", *Appl. Surf. Sci.* **169-170**, 379 (2001).
- ⁴⁵ T. Döppner, S. Teuber, M. Schumacher, J. Tiggesbäumker, and K.H. Meiwes-Broer, "Charging dynamics of metal clusters in intense laser fields", *Appl. Phys. B* **71**, 357 (2000).
- ⁴⁶ D. E. Blumling, S. G. Sayres, A. W. Castleman, Jr., "Strong-field ionization and dissociation studies of small early transition metal oxide clusters", *Int. J. Mass Spectrom.* **300**, 74 (2011).

Chapter VI

Formation, fragmentation and structures of $Y_xO_y^+$ ($x = 1, 2, y = 1-13$) clusters: collision induced dissociation experiments and density functional theory calculations

6.1 Introduction

The research field of transition metal clusters, especially transition metal oxide clusters has exhibited a rapid development in both experiment and theory in the past decades. The clusters have attracted much attention because of wide applications in many areas, such as catalysis, material science, nanotechnology and microelectronics.^{1,2,3} Among them, yttrium oxide clusters have been a subject of many theoretical and experimental studies. For example, yttrium doped vanadium oxide cluster cations are investigated in order to demonstrate the local charge effects on methane activation for catalytic purposes.⁴ Another study has shown that nanoparticles composed of cerium oxide or yttrium oxide could have possible applications in medicine.⁵

For studies of free clusters (in gas phase), well established experimental procedures – by coupling of ablation laser with a mass spectrometer – have been used,⁶ providing information on molecular, fragment and cluster ion formation in the ejected plume. Laser ablation of simple

oxides (Y_2O_3) or Y-M-Cu-O metal-composite oxides (M = Ba, Sr, Ca, Mg)^{6,7,8,9} (for example $YBa_2Cu_3O_{7-x}$) in high vacuum led to formation of pure yttrium oxide cluster ions $YO(Y_2O_3)_n^+$ or mixed cluster ions of various sizes and compositions. The laser vaporization experiments of Becker and al.⁶ have shown Y_2O_3 and YO to be the building units of generated cluster ions and the authors suggest that these clusters are products of condensation in gas phase rather than direct emission from the solid.

Recently, there have been several studies on electronic properties of small yttrium-oxide clusters. Knickelbein probed the photoionization spectra and measured electron vertical ionization potentials (IP) of Y_xO clusters ($x = 2-31$).¹⁰ Wu and Wang¹¹ performed the photoelectron spectroscopy studies (PES) on YO_y ($y = 1-5$) clusters. Pramann et al. produced $Y_xO_y^-(x = 2-10, y = 1-3)$ clusters, presented their PES spectra and measured the electron affinities.¹²

Yttrium oxide clusters of the form $Y_xO_y^+$, produced by laser vaporization, have also been investigated by Reed and Duncan, with time-of-flight (TOF) mass spectrometry and mass-selected photodissociation, providing insight in their fragmentation mechanism (fragmentation channels) and identifying the most stable stoichiometries.¹³

Moreover, formation mechanisms, structures and relative stability of transition metal oxide clusters, have been studied in our laboratory employing the collision-induced dissociation (CID) method, for mass selected titanium,¹⁴ iron^{15,16} and niobium-oxide clusters cations.¹⁷ With regards to the yttrium oxide clusters, the CID method was employed earlier to investigate some smaller species at collision energies 30–110 eV and 170 eV by Kahwa et al.¹⁸ Their CID spectra have shown higher thermodynamic stability for the clusters with general formula $Y_aO_{(3a-1)/2}^+$, where a is an odd number (e.g. YO^+ , $Y_3O_4^+$, $Y_5O_7^+$, $Y_7O_{10}^+$).

The progress in the experimental studies has motivated some theoretical calculations of the yttrium-oxide clusters, most of which were focused on monoxides. Hybrid density functional theory (DFT) calculations were performed to study the structural (geometry) and electronic properties of neutral, anionic and cationic Y_3O clusters¹⁹ and Y_4O clusters.²⁰ Yang and Xiong

extended theoretical work on monoxides with their study on structural and electronic properties of Y_xO ($x = 2-14$) clusters.²¹ Theoretical reports on other types of yttrium-oxide clusters, containing more oxygen atoms, started with the investigation of the relative stabilities and structures of $Y_xO_y^+$ cations and their neutrals.¹³ In another study, DFT calculations were performed to investigate electronic and magnetic properties of Y_xO_2 and $Y_xO_2^-$ ($x = 1-8$) clusters.²² In a recent study, electronic and geometrical structures of neutral and charged YO_y ($y = 2-12$) clusters were investigated using various functionals.²³

However, up to now, the structure and stability of yttrium-oxide clusters, especially oxygen-rich clusters, have not been investigated sufficiently. In this contribution we study mass spectra, structure and stability of $Y_xO_y^+$ ($x = 1, 2, y = 1-13$). In our experimental studies we used an alternative CID method based on crossed molecular beams,^{15,16} which enables fast measurement of fragmentation processes without the need of mass selection of individual clusters.

We also systematically investigated the structures of the prominent series of clusters with an odd number of oxygen atoms, YO_y^+ ($y = 2k + 1, k = 0-6$), and their electronic properties and energetics, using density functional theory (DFT) calculations, as previously done for iron oxide clusters.¹⁵ Finally, comparison between theoretical and experimental results are performed and discussed.

6.2 Experimental apparatus and methods

6.2.1 Setup

The cluster source and the basic experimental setup have been described in detail elsewhere^{24,25,26} and only the general features will be presented here. Yttrium oxide clusters are produced in a first vacuum chamber (source chamber), where a rotating pure yttrium target is placed just in front of an oxygen (O_2) pulsed nozzle (diameter 0.5 mm, backing pressure 4 bar).

The fundamental (1064 nm) of a Nd:YAG (neodymium-doped yttrium aluminum garnet) laser (BMI, Series 5000) is employed to vaporize the yttrium target.

6.3 DFT calculations

To further investigate the structure and stability of the YO_{2k+1}^+ ($k = 0-6$) clusters identified in the mass spectra, we have performed theoretical density functional (DFT) calculations with the Gaussian 03W program package,²⁷ to obtain the lowest energy structures, Mulliken population analysis, and energetics of these clusters.

As previously seen, the B3LYP hybrid exchange-correlation functional^{28,29,30} in combination with LanL2DZ basis sets has been proven to be efficient for the prediction of structure and different electronic properties of various yttrium-oxide clusters Y_3O ,¹⁹ Y_4O ,²⁰ Y_xO_2 and Y_xO_2^- .²² In addition, the use of a larger polarized Quadruple- ζ basis set def2-QZVP³¹ instead of effective core potential LanL2DZ basis set provides more accurate DFT calculations of bond parameters and frequencies.²³

The geometry optimizations on YO_{2k+1}^+ ($k = 0-6$) clusters have been performed using B3LYP hybrid functional and pure functional BPW91.^{28,32} The yttrium atom was treated with def2-QZVP basis set,³¹ whereas the full electron basis set 6-311G(d,p) was used for oxygen.

Two growth patterns were considered for determining the ground-state structures and low-lying isomers of the clusters. (1) We first optimized YO^+ and then we continued with the sequential addition of O_2 . To locate the most stable geometrical configurations during calculations, several initial geometries were attempted for each YO_{2k+1}^+ cluster by adding one O_2 molecule in various positions, in the vicinity of the previously optimized structure of the YO_{2k-1}^+ ($k = 1-6$) cluster. Some of these initial structures were built according to a certain symmetry group; however no symmetry restrictions were considered in the calculations in order to ensure a more thorough exploration of the potential-energy surfaces of the clusters. (2) We also

considered the possible structures reported for the same yttrium oxide cluster ions by Venkataraman.²³

For each of the initial structures, we tested different spin multiplicities (S) to find the most stable electronic state. Finally, harmonic vibrational frequencies by numerical differentiation of analytical gradients were computed on the optimized geometries (structures) at the same level of theory to characterize the stationary points and obtain zero-point energy (ZPE) corrections. No correction factors were applied for the calculation of the frequencies or the ZPE correction. The stability of the obtained wave function for the ground state structures was checked performing single point energy calculations with the same method and criteria, including the keyword Stable in the input file.

The optimized geometric structures from the DFT calculations were used to calculate geometrical cross sections of the clusters, which were then compared with the experimentally determined collision cross sections to validate the obtained ground state structures of the YO_{2k+1}^+ ($k = 1-6$) clusters. The geometrical cross sections of the theoretical structures were calculated as the average of structures projections under different orientations using the projection model.^{16,33} The radii of the atoms were evaluated using the universal potential model at the center of mass collision energy (radius $Y^+ = 0.85 \text{ \AA}$ and radius $O = 0.60 \text{ \AA}$).^{16,34,35}

6.4 Results and discussion

6.4.1 Mass spectra

A typical TOF mass spectrum of the $Y_xO_y^+$ clusters obtained in our apparatus is shown in Figure 6.1. The intensity peaks of $Y_xO_y^+$ clusters are labeled as x, y ranging from 1, 1 to 3, 4. The spectrum reveals the formation of two main cluster series containing one (YO_y^+) and two yttrium atoms ($Y_2O_y^+$). The YO_y^+ series consists of members with an odd number of oxygen atoms whereas those with an even number of oxygen are absent. The maximum number of oxygen atoms observed for these two series was 13 for YO_y^+ and 6 for $Y_2O_y^+$ under our

experimental conditions. In addition, presence of water impurities in the gas inlet system led to the formation of hydrated clusters (marked by triangles in Figure 6.1), with the general formula $YO_y^+(H_2O)$ ($y = 1, 3, 5, 7$).

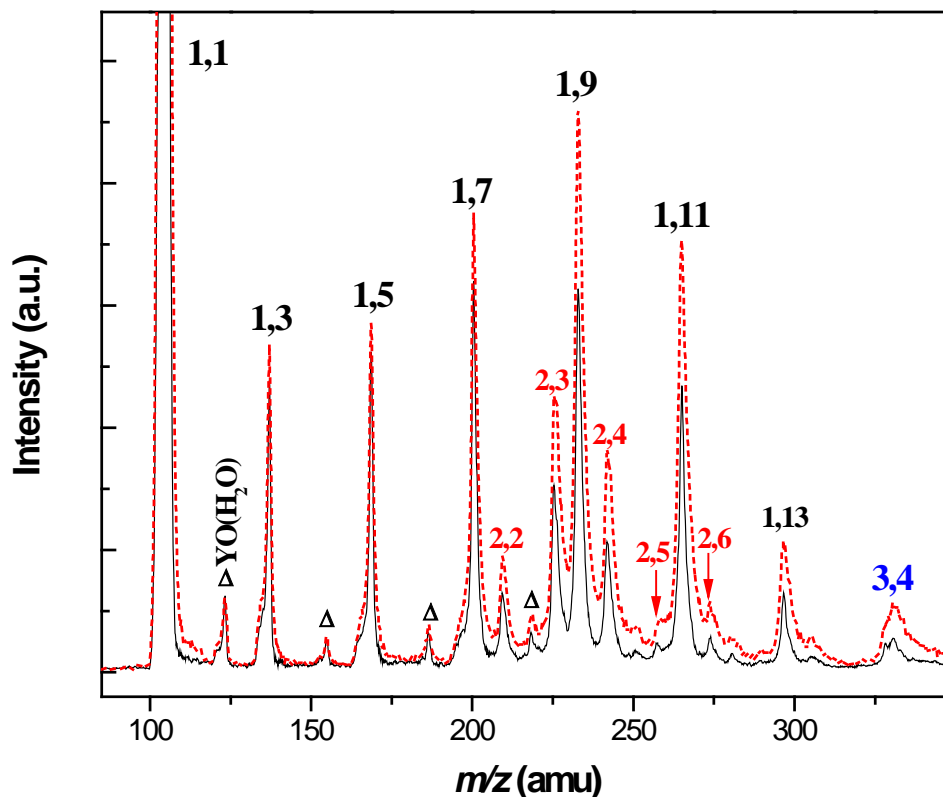


Figure 6.1. Mass spectra of $Y_xO_y^+$ clusters (labeled as x,y) obtained at $V_{\text{grid}}=0$, with beam crossing (dashed line, red) and without beam crossing (solid line, black). The Δ indicates the hydrated clusters (see text for details).

Accordingly to the spectrum in Figure 6.1, for the series of cluster ions containing an odd number of O atoms, YO_{2k+1}^+ ($k = 1-6$), we assume a formation mechanism by subsequent physisorptions of O_2 molecules to the initially formed YO^+ ion. Clusters containing more than one Y atom are also formed, but in small amounts, due to the particularity of our open cluster source,¹⁶ and the most abundant cluster containing two yttrium atoms is $Y_2O_3^+$, where the formal oxidation states of Y in the cluster ion can be represented in combination of +3 and +4. Although

in relatively small amounts, a peak at mass 331 amu in our mass spectrum is attributed to the $Y_3O_4^+$ cluster, as this cluster appears with high stability in the experiments of Reed and Duncan,¹³ and it is also the most abundant species produced by Kang and Bernstein.³⁶ Also, YO^+ and $Y_3O_4^+$ are identified as stable species and as preferred dissociation products of larger clusters by other groups.¹⁸

6.4.2 Fragmentation channels

We have measured ion intensities versus retarding potential for several YO_n^+ and $Y_2O_y^+$ clusters using the procedure described in Section 5.3.2. The potential on the retarding electrode V_{grid} was increased from 0 to a value significantly higher than the accelerating voltage, i.e., ~2100 V, and the results are shown in Figure 6.2(a–d) for YO_y^+ ($y = 5, 7, 9,$ and 11) clusters, respectively.

In the case of “beam on” signal, as the V_{grid} increases, fragments with $E_F \leq qV_{\text{grid}}$ are rejected and this appears as a sudden signal intensity decrease. This value of V_{grid} is used to derive the mass m_F from Equation 1.39. For each of the YO_y^+ cluster investigated, the only fragmentation channels we could identify were those corresponding to loss of one or more pairs of O atoms (possibly molecules) and are seen as well pronounced steps in Figure 6.2(a–d). As a typical example, there are four possible fragmentation channels in the case of YO_9^+ (Figure 6.2(c)), which lead to the YO_7^+ , YO_5^+ , YO_3^+ , and eventually YO^+ products.

Similar measurements were performed for clusters containing two yttrium atoms. The $Y_2O_2^+$ fragmentation (results not shown) produces only one fragment ion, YO^+ , in agreement with Ref. 18. The graphs in Figure 6.3(a,b) show plots of ion intensities vs retarding potential for two representative clusters containing two yttrium atoms: $Y_2O_3^+$ and $Y_2O_4^+$, respectively.

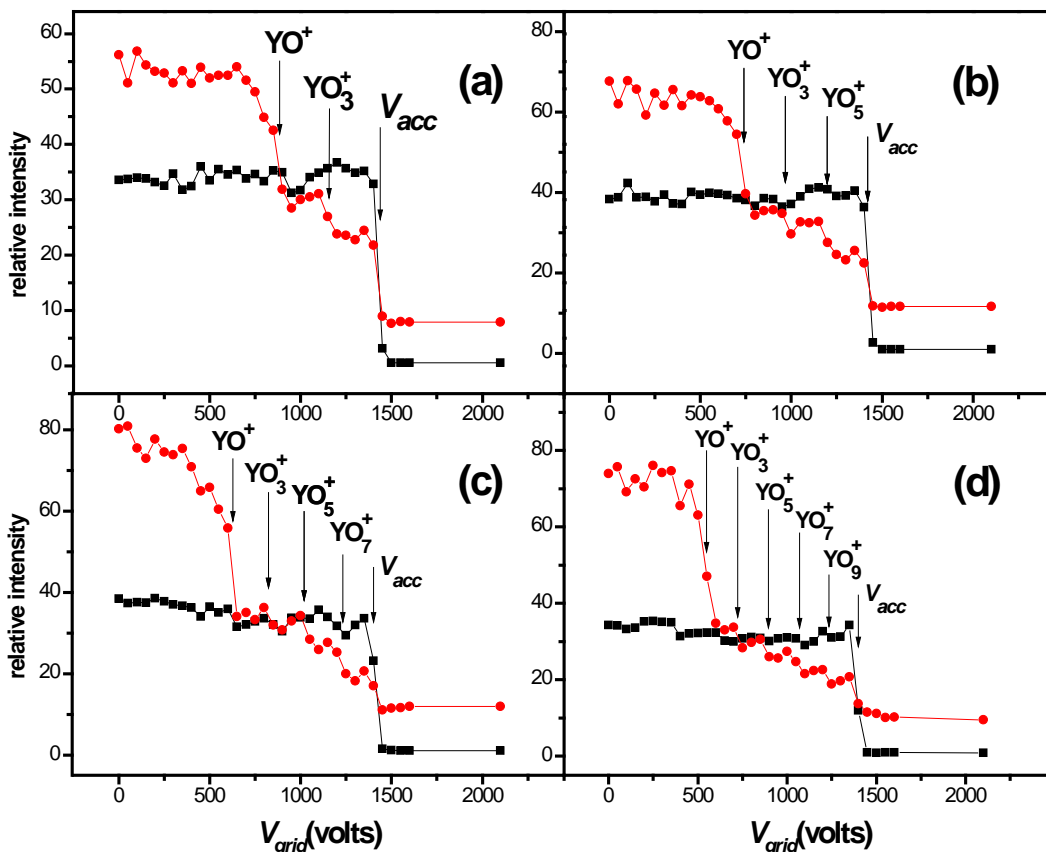


Figure 6.2. Relative ion intensity of (a) YO_5^+ , (b) YO_7^+ , (c) YO_9^+ and (d) YO_{11}^+ versus retarding potential, with beam crossing (circles) and without beam crossing (squares). The arrows indicate the laboratory kinetic energies E_{Lab} of the corresponding fragment ions. The kinetic energy distribution of the ions is obtained by taking the negative differential.

From Figure 6.3(a), we observe that $Y_2O_3^+$ releases O to produce $Y_2O_2^+$ or undergoes fragmentation by loss of YO_2 to produce YO^+ . The center of mass collision energy of $Y_2O_3^+$ is 124 eV, and the main CID product is YO^+ , also in agreement with Ref. 18, where formation of YO^+ was identified as the dominant product at collision energies higher than 50 eV.

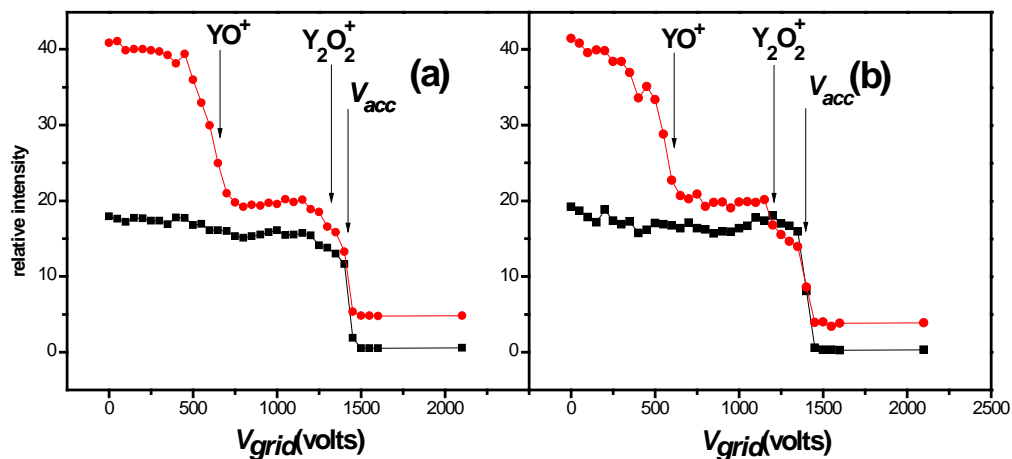
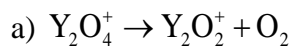


Figure 6.3. Fragmentation of (a) $Y_2O_3^+$ and (b) $Y_2O_4^+$, with beam crossing (circles) and without beam crossing (squares).

The fragmentation channels of the ion $Y_2O_4^+$, depicted in Figure 6.3(b), are most likely the following two:



Although we cannot directly identify the neutral fragments, the products accompanying the formation of YO^+ in Reaction b) are most likely YO and O_2 , as YO_3 is not expected to have a stable structure. All fragmentation channels of the $Y_2O_y^+$ clusters and their fragmentation products are summarized in Table 6.1.

Table 6.1. Fragmentation channels of $Y_2O_y^+$ clusters and their fragmentation products

Cluster ion	Fragment ion	Neutral(s)
$Y_2O_2^+$	YO^+	YO
$Y_2O_3^+$	$Y_2O_2^+$	O
	YO^+	YO_2
$Y_2O_4^+$	$Y_2O_2^+$	O_2
	YO^+	$YO + O_2$

6.4.3 DFT calculations

To gain further insight in the formation and stability of the clusters, we performed DFT calculations on the prominent species in our mass spectra, YO_{2k+1}^+ ($k = 0-6$). For each cluster investigated, we optimized numerous initial geometries and multiplicities in the search for the ground state structure (and multiplicity).

The calculation of the total binding E_b energy, which corresponds to the attaching of all O_2 units to the YO^+ ion, $\text{YO}^+ + k\text{O}_2 = \text{YO}_{2k+1}^+$, was done according to the following formula:

$$E_b(\text{YO}_{2k+1}^+) = E_{el}(\text{YO}^+) + k \cdot E_{el}(\text{O}_2) - E_{el}(\text{YO}_{2k+1}^+),$$

where all the electronic E_{el} energies were corrected by adding the zero point energy (ZPE) to the calculated values:

$$E_{el} = E_{calc} + E(\text{ZPE}).$$

The optimized geometries which correspond to the ground states and low-lying isomers of YO_{2k+1}^+ ($k = 1-6$) clusters, along with their multiplicities, are presented in Figure 6.4. The stable structures are designated by ya and yb, where y is the number of oxygen atoms, whereas labels a and b correspond to the ground and first low-lying states, respectively (according to the total binding energy E_b from high to low). Relative energies (RE), which represent the difference in total binding energy E_b between the energetically lowest structures, are also given in the Figure 6.4.

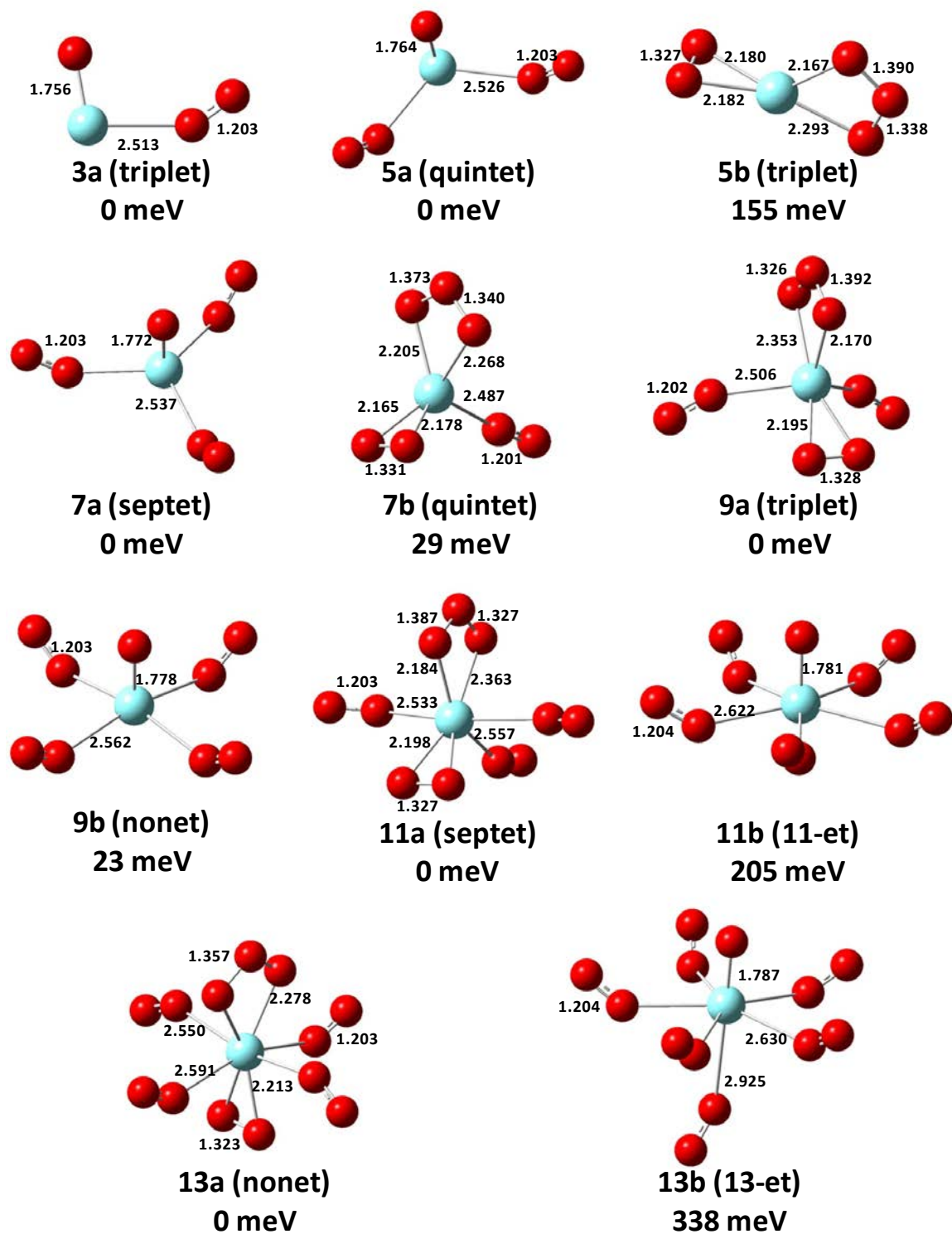


Figure 6.4. The optimized cation ground-state and low-energy structures for the YO_{2k+1}^+ ($k = 1-6$) clusters along with bond lengths, multiplicities and relative energies RE.

The relative stability of the clusters usually correlates with differences in the binding energies of the successive clusters, calculated with the relation

$$\Delta E_b = E_b(\text{YO}_{2k+1}^+) - E_b(\text{YO}_{2k-1}^+).$$

In Table 6.2, we summarize the multiplicities of the most stable and some low-lying cluster isomers, the calculated electronic E_{el} energies for these configurations, the total E_b binding energies for all O_2 ligands, and the binding energy differences ΔE_b of the YO_{2k+1}^+ clusters.

Table 6.2. Calculated structures (symmetries), multiplicities, total binding energies E_b , relative energies RE , and binding energy differences ΔE_b of YO_{2k+1}^+ clusters obtained at the DFT/B3LYP level of theory.

cluster	Symmetry group (isomer)	multiplicity	E_b (eV)	RE (meV)	ΔE_b (eV)
YO_3^+	C_s (3a)	triplet	2.217	0	2.217
	C_s	singlet	0.624	1593	-
YO_5^+	C_s (5a)	quintet	4.408	0	2.191
	C_s (5b)	triplet	4.253	155	-
YO_7^+	C_{3v} (7a)	septet	6.577	0	2.169
	C_1 (7b)	quintet	6.548	29	-
	C_1	triplet	6.546	31	-
YO_9^+	C_1 (9a)	triplet	8.699	0	2.122
	C_1	septet	8.693	6	-
	C_1	quintet	8.693	6	-
	C_{4v} (9b)	nonet	8.676	23	-
YO_{11}^+	C_s (11a)	septet	10.819	0	2.120
	C_1	triplet	10.807	12	-
	C_5 (11b)	11-et	10.614	205	-
	C_1	septet	10.590	229	-
YO_{13}^+	C_{2v} (13a)	nonet	12.795	0	1.976
	C_{2v}	11-et	12.787	8	-
	C_1 (13b)	13-et	12.457	338	-
	C_1	11-et	12.030	765	-

The global minimum of YO^+ is a singlet state, in agreement with Ref. 23. The calculated length of the yttrium-oxygen bond is 1.747 Å, which also agrees with the value of 1.745 Å computed at the same B3LYP level in the same study.

For YO_3^+ , a planar geometry with C_s symmetry is predicted, where the oxygen atoms are bound to the yttrium to form one oxo ligand (terminal oxygen atom) and an end-on bonded $\eta^1\text{-O}_2$ ligand (superoxo ligand), presented as the structure 3a in Figure 6.4. In this study, the terminal oxygen atom and terminal Y–O bond will be denoted as O_t and Y– O_t , respectively. The distance between Y and the superoxo ligand is quite long (2.513 Å) compared with the length of the Y– O_t bond (1.756 Å). For this cluster we predicted a triplet ground state. Another stable structure obtained for YO_3^+ is a singlet (not shown in the Figure 6.4), also with C_s symmetry. In this structure, the distance between Y and superoxo group is significantly longer (2.603 Å). However, this isomer structure is higher in energy than the triplet with 1593 meV and on the basis of the large energy difference we rule out this structure. The predicted minimum energy structure 3a is comparable with the observation of $\text{YO}^+(\text{CO})$ instead of $\text{Y}^+(\text{CO}_2)$.³⁷

In the case of the YO_5^+ cluster we obtained two stable structures, 5a and 5b, corresponding to a quintet and a triplet state, respectively, with quite different structures. The quintet state has a nonplanar structure corresponding to C_s symmetry, with one O_t atom and two end-on bonded superoxo ligands coordinated around central yttrium, where the bond lengths are slightly longer than in the case of YO_3^+ cluster. In the triplet state the oxygen atoms form side-on bonded peroxo ($\eta^2\text{-O}_2$) and ozonide ($\eta^2\text{-O}_3$) ligands similarly to the structure presented in Ref 23. The quintet state is energetically lower than the triplet for 155 meV, and represents the ground state of YO_5^+ .

The ground electronic state of YO_7^+ is a septet with C_{3v} symmetry (7a), with an O_t atom and three superoxo ligands coordinated around yttrium. All bond lengths are around 0.01 Å longer than in the case of the ground state YO_5^+ structure (5a), except O–O bond of the superoxo ligands, whose length remains unchanged (around 1.203 Å), and is very close to the calculated value of 1.207 Å for O_2 . The calculated bond length is in very good agreement with

the precise experimental value of 1.2074 Å.³⁸ Additionally, two stable structures were found, 29 and 31 meV higher in total binding energy than the ground state, corresponding to a quintet and a triplet state, respectively, thus representing two degenerate states. These two states are very similar superoxo–peroxo ozonide structures, with close geometrical parameters, thus only the quintet state is presented (7b).

In the case of the YO_9^+ , we obtained three degenerate states: a triplet, a quintet, and a septet, with the triplet state being the most stable, whereas the later two isomers are ~6 meV above the triplet. All three structures have C_1 geometry and very similar values of structural parameters; therefore only the ground triplet state is presented (9a). These cluster structures have two superoxo, one peroxo, and one ozonide groups connected to the central yttrium. Another stable structure (9b) was obtained, with one oxo and four superoxo ligands, placed approximately in the same equatorial plane normal to the axis of the YO^+ unit (the axis of the cluster); the angles between the YO^+ axis and the coordinated superoxo ligands are around 60°. Although the optimized structure has C_1 symmetry, by putting a higher cutoff level below which structural parameters are considered to be equal, the YO_9^+ cluster can be approximated with a higher C_{4v} symmetry group.

Of several different stable isomeric structures obtained in the case of YO_{11}^+ cluster, the ground state and the first low-lying isomer have similar geometrical structure and bond parameters and are found to have septet (11a) and triplet spin multiplicity, respectively. They are predicted to be (nearly) degenerate, with the ground septet state being only 12 meV more stable than the triplet (not presented in the Figure 6.4). These two isomers have a geometrical structure similar to the one of the most stable YO_9^+ isomer (9a), however, with one additional superoxo ligand. In addition, there also exists a low-lying isomer structure 11b (205 meV higher than the ground state) with the multiplicity of 11, possessing C_5 symmetry with five oxo ligands distributed around the YO^+ unit.

For the largest cluster theoretically studied, YO_{13}^+ , we found two degenerate structures corresponding to the ground state (13a) and the first low-lying state with a multiplicity of 9 and

11, respectively, where the latter one is 8 meV higher. The two structures have four superoxo, one peroxo, and one ozonide groups, and possess C_{2v} symmetry. Similarly to the previous clusters, for this cluster size we have also found low-lying structures with a YO^+ unit – with multiplicities of 13 (338 meV above the ground state) and 11 (765 meV above the ground state), respectively. These two isomers were found to have C_1 symmetry with one oxo and five superoxo ligands in pentagonal arrangement and one additional superoxo ligand placed approximately on the same axis with the YO^+ unit. These two isomers have very similar structures (13b), with the bond lengths differing by less than 0.01 Å. Of the six bonds between yttrium and superoxo ligands, the five in the “equatorial” plane are around 2.630 Å, whereas the on-axis bond is quite elongated (2.925 Å).

From Figure 6.4 we observe a series of cluster isomers with $n \geq 3$, possessing a shorter $Y-O_t$ bond, and significantly longer bonds between central yttrium and the weakly coordinated superoxo ligands. Here the optimized $Y-O_t$ bond distance increases with the cluster size, between 1.747 Å in the case of YO^+ and 1.787 Å for the largest YO_{13}^+ . For the same structures, the bonds between yttrium and the superoxo ligands range from 2.513 Å in the case of YO_3^+ to 2.630 Å for YO_{13}^+ . These structures strongly imply the existence of a chemically bound YO^+ cluster core whose formation can be explained by the fact that the initial phase in the growth of these clusters, $Y^+ + O_2 \rightarrow YO^+ + O$, is exothermic.³⁹ The preference for formation of clusters with an odd number of O atoms can also be explained by the stability of YO^+ core, where yttrium takes its stable +3 oxidation state¹³ corresponding to the bulk yttrium oxide, Y_2O_3 .^{40, 41}

We observe another series of cluster isomers without the YO^+ core, starting from the size $y \geq 5$, containing superoxo, peroxo, and ozonide oxygen. All the bonds connecting yttrium and these ligands show a slight increase in the bond lengths with the cluster size. The bond lengths between yttrium and superoxo ligands range between 2.487 and 2.591 Å, the bond lengths between yttrium and peroxo ligands are between 2.165 and 2.213 Å, whereas the bonds between yttrium and ozonide ligands vary from 2.167 and 2.363 Å.

In Figure 6.5 we plot the binding energy difference ΔE_b of the ground energy state (ground state structures of) YO_{2k+1}^+ ($k = 1-6$) cluster ions, corresponding to the reaction $YO_{2k-1}^+ + O_2 \rightarrow YO_{2k+1}^+$ leading to the formation of YO_{13}^+ .

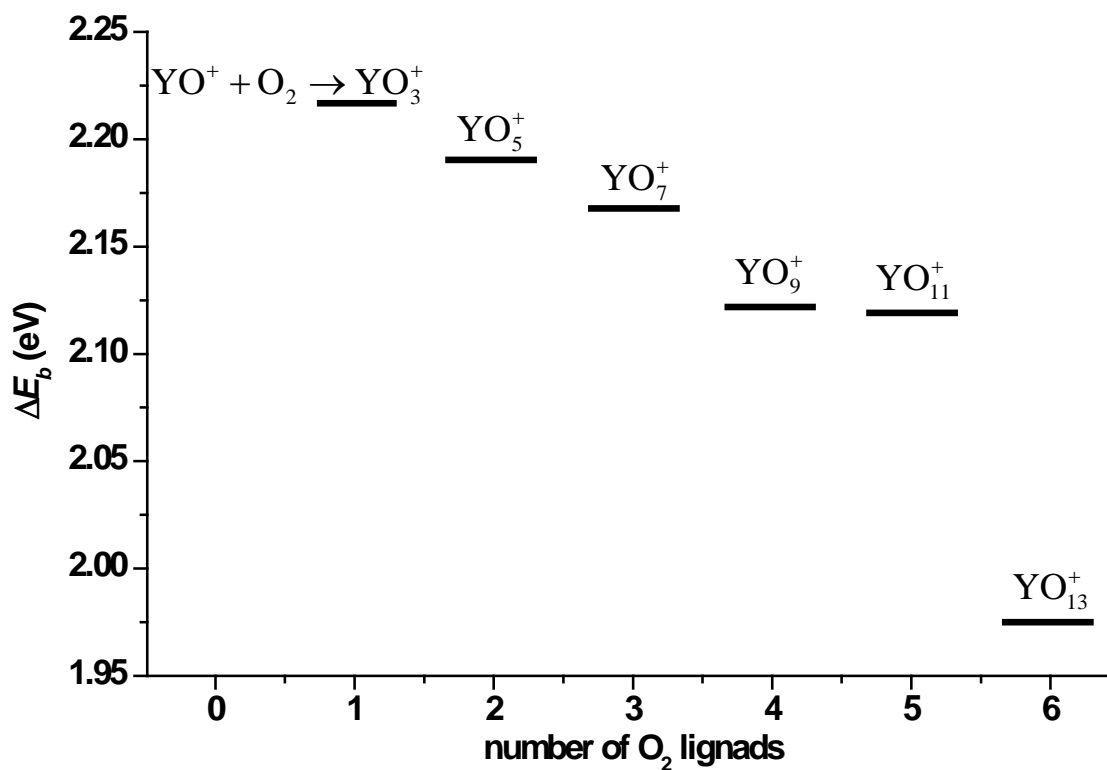


Figure 6.5. Variation of the binding energy difference ΔE_b of the YO_{2k+1}^+ , ($k = 1-6$) cluster ions with the number of O_2 ligands.

Figure 6.5 shows that as the number of O_2 attached to the YO^+ core increases, the sequential reactions gradually become less energetic favorable. The sequential bonding energy shows only a slight decrease until YO_{11}^+ , and then it shows a sudden decrease for YO_{13}^+ . As a consequence, the formation of clusters with more than five O_2 ligands becomes thermodynamically less favored. These results are in agreement with our experimental results for the cluster abundances shown in the mass spectrum (Figure 6.1), where the a series of relatively intense clusters containing up to five O_2 ligands is followed by a much lower YO_{13}^+ peak. This

observation is similar to the case of iron oxide clusters, where attaching up to five O₂ molecules to a Fe cation is a thermodynamically favored process, but adding one more O₂ is endothermic, which resulted in dominant production of Fe(O₂)_n⁺ (*n* = 1–5) and much weaker peaks for clusters with more than ten O atoms.¹⁵

In contrast to the theoretical results of Venkataraman,²³ which indicate that there are no thermodynamically stable structures for clusters with *n* > 8, our experimental results have shown formation of significant amounts of YO₉⁺, YO₁₁⁺, and YO₁₃⁺ clusters. Our calculations showed that for each YO_{2k+1}⁺, (*k* = 0–6) cluster there are two types of structures, close in energy. On the basis of the current state of the calculations, we are not able to rule out any of them; probably a mixture exists in the cluster beam because the cluster formation starts at relatively high temperature (≥300 K) in the gas-plasma mixing region. Therefore, more calculations are needed to gain information on these aspects.

6.4.4 Collision Cross Section Measurements

For the experimental determination of the fragmentation cross section we employ the procedure described in Section 2.2.2 as it is outlined in detail in Ref 17. Equation 2.4 can be rewritten in the following way:

$$QNL = -\ln \frac{I_{ON}(V_{grid} \lesssim V_{acc}) - I_{ON}(V_{grid} \gg V_{acc})}{I_{OFF}(V_{grid} \lesssim V_{acc}) - I_{OFF}(V_{grid} \gg V_{acc})} \quad (6.2)$$

where I_{ON} and I_{OFF} are signal intensities at appropriate voltages with (ON) and without (OFF) the secondary beam. With Equation 6.2, the quantity QNL , which we call relative fragmentation cross section is determined from the graphs in Figure 6.2(a–d) for the individual YO_y⁺ clusters. The results corresponding to experiments performed at the acceleration voltage 1500 V (laboratory kinetic energy = 1500 eV) as a function of the cluster size, i.e., the number of oxygen atoms *y*, are displayed in Figure 6.6. Measurements were also performed at an acceleration voltage of 1000 V, and these results are also plotted in Figure 6.6.

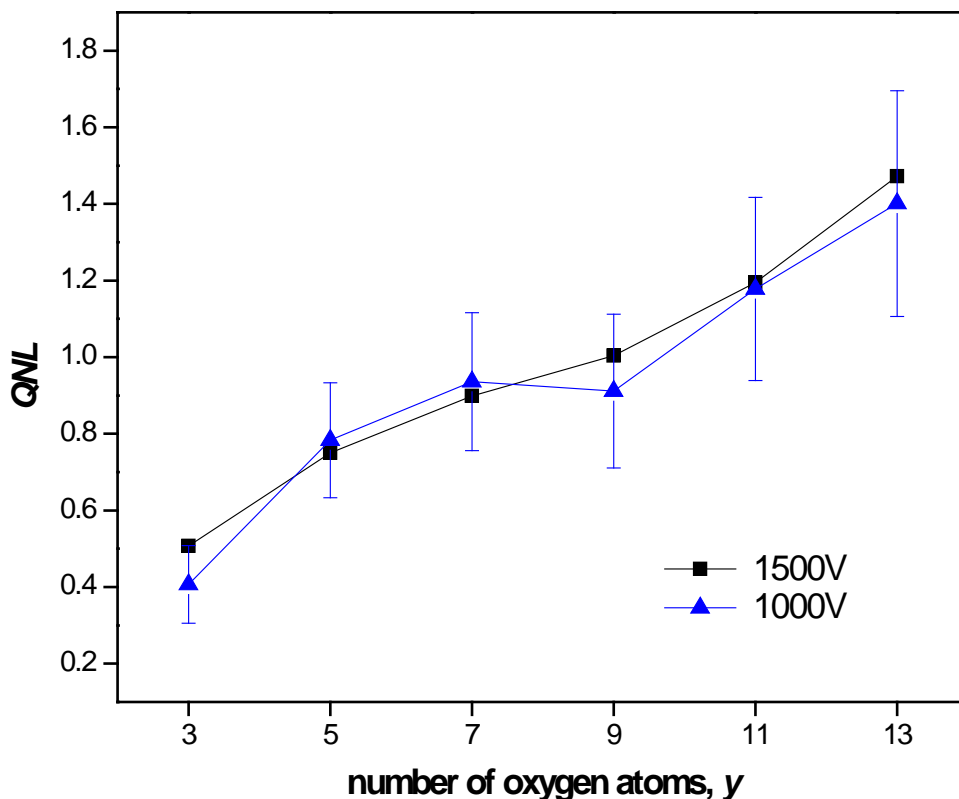


Figure 6.6. Comparison of relative fragmentation cross section of YO_y^+ clusters, obtained using different acceleration voltages V_{acc} , as a function of number of oxygen atoms, y .

The cross sections show similar trends, within experimental errors (estimated at around 20%). The cross sections for $\text{YO}_y^+ + \text{Ne}$ collisions increase with y , as seen in Figure 6.6. The relative minimum observed for $y = 9$ can be explained by the special stability of this cluster, as noticed also in the mass spectrum in Figure 6.1, where it is seen as the most prominent cluster. A similar observation was made for the iron oxide cluster containing 10 oxygen atoms.¹⁵

The center of mass frame collision energy for the smallest YO_y^+ cluster investigated, YO_3^+ , is 193 eV and decreases with the number of O down to 106.1 eV in the case of YO_{11}^+ , whereas for comparison, the dissociation energy of YO is ~ 7.4 eV.²³ Therefore, in collisions with the target gas, for every cluster of the series the energy available for conversion to internal energy is much higher than the dissociation threshold and therefore it is expected to cause efficient fragmentation. In the situation of high-energy collisions, where all collisions lead to

dissociation, the measured fragmentation cross sections can be considered as the lower limit of the total collision cross section. Because the present experiments are performed under a relative large center of mass collision energy, the collision cross section can be approximated with the orientationally averaged geometrical cross section, which reflects directly the geometrical structure of the involved species.

Based on these considerations, a validation for the theoretical geometrical structures from Section 6.4.2 is the comparison of their geometrical cross sections with the experimentally determined collision cross sections. In Figure 6.7 they are shown as a function of the number of oxygen atoms, y . The experimental values are normalized and displayed on the same figure for comparison.

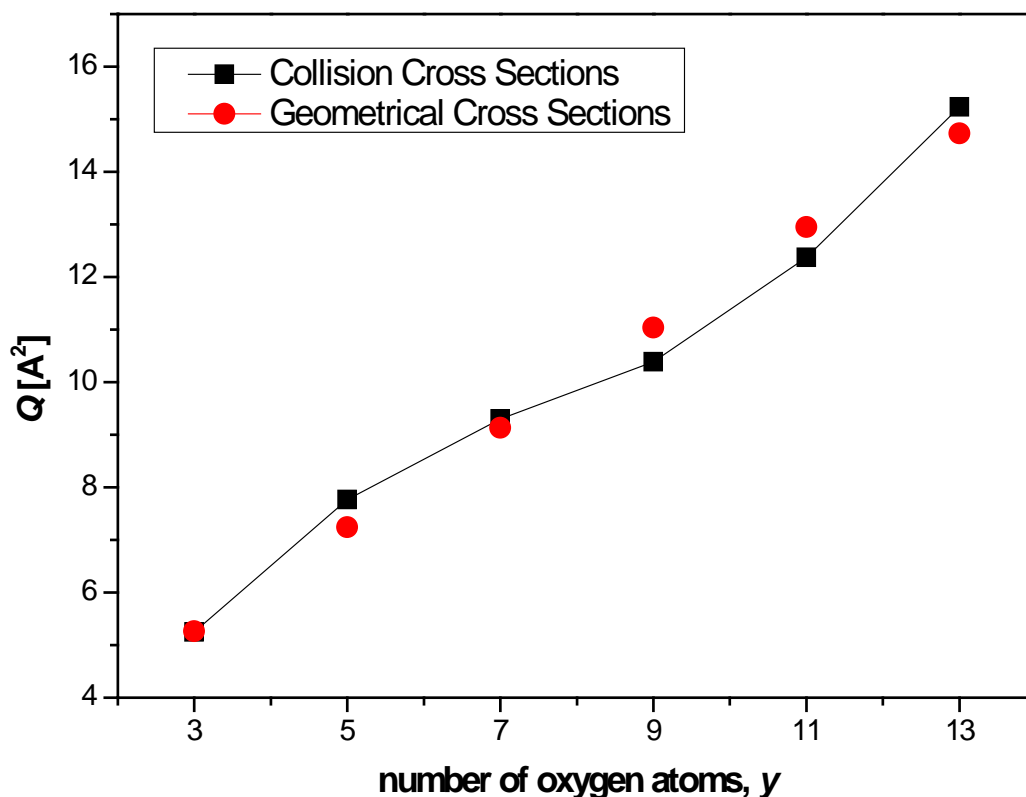


Figure 6.7 Comparison between the experimental (squares) and theoretical (circles) cross sections at 1500 eV laboratory energy. The experimental values have been normalized to the theoretical ones.

The general evolution trend is similar for the two sets of data and a good correspondence exists between the experimental and theoretical values. Although the theoretical values show an almost linear trend, a change of slope is observed at YO_9^+ for the experimentally determined cross sections. This discrepancy can be due to the fact that we compare the measured fragmentation cross section with the theoretically calculated geometrical one. Though generally the two values are very similar, in the case of clusters with special stability, the fragmentation cross section can be smaller. This was also observed in the cases of FeO_{10} and NbO_{10} .^{16,17}

6.5 Conclusions

We produced oxygen rich yttrium oxide clusters by mixing the laser-ablated yttrium plume with a pure oxygen molecular jet. Mostly clusters containing one metal atom are formed, with reduced quantities of clusters containing more Y atoms. Contrary to other transition metal oxide clusters produced in our laboratory (FeO_y^+ , NbO_y^+), the YO_y^+ clusters have odd values of y , due to the negative standard enthalpy of formation of YO, whereas for FeO and NbO (TiO, TaO, VO) is positive.⁴² Additionally to the TOF mass spectrometry, the YO_y^+ clusters have been studied by CID and their relative collision cross sections were measured. We used an experimental configuration developed in our laboratory, on the basis of the interaction of the ionic clusters beam with an atomic beam of noble gas and the subsequent separation of the reaction products (fragments) using an energy filter. In this way, we identified the fragmentation channels of the clusters after collision with noble gas atoms as the successively loss of oxygen molecules (or pairs of oxygen atoms) down to a YO^+ core. Therefore, on the basis of the fragmentation patterns of the clusters, we propose that the clusters are formed via sequentially attaching of O_2 molecules to the initially formed YO^+ cluster core.

Furthermore, DFT calculations were performed to identify the clusters' structures. Starting from YO_5^+ , two different series of structures are observed. In the case of the first series

of cluster isomers, O_2 molecules bind to the YO^+ core, to form end-on bonded superoxo ligands. In the second series of cluster isomers, the oxygen is in superoxo, peroxy and ozonide states.

Although the energy difference between the isomers of the same size is relatively small, there might exist a high-energy barrier for the isomerization reaction, which leaves most of the cluster in one of the isomer forms. Further theoretical work is needed to calculate different configurations and to explore the configuration space of these systems.

References

- ¹ V. E. Henrich and P. A. Cox, *The Surface Science of Metal Oxides* (Cambridge University Press, Cambridge, 1994).
- ² M. D. Morse, „Clusters of transition metal atoms,“ *Chem. Rev.* **86**, 1049 (1986).
- ³ A. W. Castleman and K. H. Bowen, „Clusters: structure, energetics, and dynamics of intermediate states of matter,“ *J. Phys. Chem.-Us.* **100**, 12911 (1996).
- ⁴ Z.-Y. Li, Y.-X. Zhao, X.-N. Wu, X.-L. Ding, and S.-G. He, „Methane activation by yttrium-doped vanadium oxide cluster cations: local charge effects,“ *Chem.-Eur. J.* **17**, 11728 (2011).
- ⁵ D. Schubert, R. Dargusch, J. Raitano, and S. W. Chan, „Cerium and yttrium oxide nanoparticles are neuroprotective,“ *Biochem. Bioph. Res. Co.* **342**, 86 (2006).
- ⁶ C. H. Becker and J. B. Pallix, „Laser ablation of bulk $\text{YBa}_2\text{Cu}_3\text{O}_{7-\delta}$ and cluster emission,“ *J. Appl. Phys.* **64**, 5152 (1988).
- ⁷ A. Mele, D. Consalvo, D. Stranges, A. Giardiniguidoni, and R. Teghil, „Cluster ion formation by laser evaporation of solid complex oxides,“ *Appl. Surf. Sci.* **43**, 398 (1989).
- ⁸ Z. Y. Liu, C. R. Wang, R. B. Huang, and L. S. Zheng, „Mass-distribution of cluster ions produced from laser-ablation of metal-composite-oxides Y-M-Cu-O (M = Ba, Sr, Ca, Mg),“ *Z. Phys. D Atom. Mol. Cl.* **34**, 257 (1995).
- ⁹ J. Giapintzakis, A. Sfounis, and M. Velegrakis, „A comparative mass spectroscopic study between infrared and ultraviolet laser ablation of a superconducting $\text{YBa}_2\text{Cu}_3\text{O}_{7-x}$ target,“ *Int. J. Mass Spectrom.* **189**, 1 (1999).
- ¹⁰ M. Knickelbein, „Photoionization spectroscopy of yttrium clusters: ionization potentials for Y_n and Y_nO ($n = 2-31$),“ *J. Chem. Phys.* **102**, 1 (1995).
- ¹¹ H. B. Wu and L. S. Wang, „Photoelectron spectroscopy and electronic structure of ScO_n^- ($n = 1-4$) and YO_n^- ($n = 1-5$): strong electron correlation effects in ScO^- and YO^- ,“ *J. Phys. Chem. A* **102**, 9129 (1998).

-
- ¹² A. Pramann, Y. Nakamura, A. Nakajima, and K. Kaya, „Photoelectron spectroscopy of yttrium oxide cluster anions: effects of oxygen and metal atom addition,” *J. Phys. Chem. A* **105**, 7534 (2001).
- ¹³ Z. A. Reed and M. A. Duncan, „Photodissociation of yttrium and lanthanum oxide cluster cations,” *J. Phys. Chem. A*, **112**, 5354 (2008).
- ¹⁴ M. Velegarakis, M. Massaouti, and M. Jadraque, „Collision-induced dissociation studies on gas-phase titanium oxide cluster cations,” *Appl. Phys. A-Mater.* **108**, 127 (2012).
- ¹⁵ G. Mpourmpakis, M. Velegarakis, C. Mihesan, and A. N. Andriotis, „Symmetry-switching molecular $\text{Fe}(\text{O}_2)_n^+$ clusters,” *J. Phys. Chem. A* **115**, 7456 (2011).
- ¹⁶ M. Velegarakis, C. Mihesan, and M. Jadraque, „Collision-induced dissociation studies on $\text{Fe}(\text{O}_2)_n^+$ ($n = 1-6$) clusters: application of a new technique based on crossed molecular beams,” *J. Phys. Chem. A* **117**, 2891 (2013).
- ¹⁷ C. Mihesan, P. Glodić, and M. Velegarakis, „Collision-induced dissociation of Nb_xO_y^+ ($x = 1, 2, y = 2-12$) clusters: crossed molecular beams and collision cell studies,” *Appl. Phys. A-Mater.* **118**, 1479 (2015).
- ¹⁸ I. A. Kahwa, J. Selbin, T. C. Y. Hsieh, D. W. Evans, K. M. Pamidimukkala, and R. Laine, „Stability trends and fragmentation patterns of gaseous yttrium-oxide clusters studied by fast atom bombardment tandem mass-spectrometry,” *Inorg. Chim. Acta.* **144**, 275 (1988).
- ¹⁹ G. Y. Gu, B. Dai, X. L. Ding, J. L. Yang, „A theoretical study of the Y_3O clusters,” *Eur. Phys. J D.* **29**, 27 (2004).
- ²⁰ B. Dai, K. M. Deng, and J. L. Yang, „A theoretical study of the Y_4O cluster,” *Chem. Phys. Lett.* **364**, 188 (2002).
- ²¹ Z. Yang and S. J. Xiong, „Structural, electronic, and magnetic properties of Y_nO ($n = 2-14$) clusters: density functional study,” *J. Chem. Phys.* **129**, 124308 (2008).
- ²² Z. Yang and S. J. Xiong, „Theoretical study of Y_nO_2 and Y_nO_2^- ($n = 1-8$) clusters,” *J Phys. Chem. A.* **114**, 54 (2010).
- ²³ N. S. Venkataramanan, „Effect of oxygen content and charge on the structure, stability and optoelectronic properties of yttrium oxide clusters,” *J. Phys. Chem. Solids.* **82**, 91 (2015).

-
- ²⁴ C. Lüder and M. Velegarakis, „Photofragmentation spectrum of the Sr⁺Ar complex,” *J. Chem. Phys.* **105**, 2167 (1996).
- ²⁵ C. Lüder, E. Georgiou, and M. Velegarakis, “Studies on the production and stability of large C_N⁺ and M_xR_N⁺ (M = C, Si, Ge and R = Ar, Kr) clusters,” *Int. J. Mass Spectrom. Ion Proc.* **153**, 129 (1996).
- ²⁶ E. Witkowicz, H. Linnartz, C. A. de Lange, W. Ubachs, A. Sfounis, M. Massaouti, and M. Velegarakis, „Mass spectrometric and laser spectroscopic characterization of a supersonic planar plasma expansion,” *Int. J. Mass Spectrom.* **232**, 25 (2004).
- ²⁷ M. J. Frisch, G. W. Trucks, H. B. Schlegel, G. E. Scuseria, M. A. Robb, J. R. Cheeseman, J. A. Montgomery, Jr. T. Vreven, K. N. Kudin, J. C. Burant, J. M. Millam, S. S. Iyengar, J. Tomasi, V. Barone, B. Mennucci, M. Cossi, G. Scalmani, N. Rega, G. A. Petersson, H. Nakatsuji, M. Hada, M. Ehara, K. Toyota, R. Fukuda, J. Hasegawa, M. Ishida, T. Nakajima, Y. Honda, O. Kitao, H. Nakai, M. Klene, X. Li, J. E. Knox, H. P. Hratchian, J. B. Cross, V. Bakken, C. Adamo, J. Jaramillo, R. Gomperts, R. E. Stratmann, O. Yazyev, A. J. Austin, R. Cammi, C. Pomelli, J. W. Ochterski, P. Y. Ayala, K. Morokuma, G. A. Voth, P. Salvador, J. J. Dannenberg, V. G. Zakrzewski, S. Dapprich, A. D. Daniels, M. C. Strain, O. Farkas, D. K. Malick, A. D. Rabuck, K. Raghavachari, J. B. Foresman, J. V. Ortiz, Q. Cui, A. G. Baboul, S. Clifford, J. Cioslowski, B. Stefanov, G. Liu, A. Liashenko, P. Piskorz, I. Komaromi, R. L. Martin, D. J. Fox, T. Keith, M. A. Al-Laham, C. Y. Peng, A. Nanayakkara, M. Challacombe, P. M. W. Gill, B. Johnson, W. Chen, M. W. Wong, C. Gonzalez, and J. A. Pople, Gaussian 03, revision D.01; Gaussian, Inc.: Wallingford, CT, 2004.
- ²⁸ A. D. Becke, „Density-functional exchange-energy approximation with correct asymptotic behavior,” *Phys. Rev. A: At., Mol., Opt. Phys.* **38**, 3098 (1988).
- ²⁹ A. D. Becke, „Density-functional thermochemistry 0.3. The role of exact exchange,” *J. Chem. Phys.* **98**, 5648 (1993).
- ³⁰ C. T. Lee, W. T. Yang, and R. G. Parr, „Development of the Colle-Salvetti correlation-energy formula into a functional of the electron density,” *Phys. Rev. B: Condens. Matter Mater. Phys.* **37**, 785 (1988).
- ³¹ F. Weigend, „Accurate Coulomb-fitting basis sets for H to Rn,” *Phys. Chem. Chem. Phys.* **8**, 1057 (2006).

-
- ³² J. P. Perdew and Y. Wang, „Accurate and simple analytic representation of the electron-gas correlation energy,” *Phys. Rev. B: Condens. Matter Mater. Phys.* **45**, 13244 (1992).
- ³³ G. Vonhelden, M. T. Hsu, N. Gotts, and M. T. Bowers, „Carbon cluster cations with up to 84 atoms – Structures, formation mechanism, and reactivity,” *J. Phys. Chem.* **97**, 8182 (1993).
- ³⁴ D. J. O’Connor and J. P. Biersack, „Comparison of theoretical and empirical interatomic potentials,” *Nucl. Instrum. Methods Phys. Res., Sect. B* **15**, 14 (1986).
- ³⁵ P. Biersack and J. F. Ziegler, „The Stopping and Range of Ions in Solids,” In *Springer Series in Electrophysics Vol. X*, eds. H. Ryssel, H. Glawischnig (Springer, Berlin, 1982) p. 122.
- ³⁶ W. Kang and E. R. Bernstein, „Formation of yttrium oxide clusters using pulsed laser vaporization,” *Bull. Korean Chem. Soc.* **26**, 345 (2005).
- ³⁷ M. R. Sievers and P. B. Armentrout, „Activation of carbon dioxide: gas-phase reactions of Y^+ , YO^+ , and YO_2^+ with CO and CO_2 ,” *Inorg. Chem.* **38**, 397 (1999).
- ³⁸ K. P. Huber and G. Herzberg, *Molecular Spectra and Molecular Structure, Vol. IV. Constants of Diatomic Molecules* (Van Nostrand Reinhold Company, New York, 1979).
- ³⁹ M. R. Sievers, C. Yu-Min, and P. B. Armentrout, „Metal oxide and carbide thermochemistry of Y^+ , Zr^+ , Nb^+ , and Mo^+ ,” *J. Chem. Phys.* **105**, 6322 (1996).
- ⁴⁰ P. A. Cox, *Transition Metal Oxides* (Clarendon Press, Oxford, 1992).
- ⁴¹ C. N. Rao and B. Raveau, *Transition Metal Oxides* (John Wiley, New York, 1998).
- ⁴² J. B. Pedley and E. M. Marshall, „Thermochemical data for gaseous monoxides,” *J. Phys. Chem. Ref. Data* **12**, 967 (1983).

